Design of an Integrated Electrostatic Atomic Force Microscope

by

Hamidreza Nafissi

A thesis
presented to the University of Waterloo
in fulfillment of the
thesis requirement for the degree of
Doctor of Philosophy
in
Electrical and Computer Engineering

Waterloo, Ontario, Canada, 2018

Examining Committee Membership

The following served on the Examining Committee for this thesis. The decision of the Examining Committee is by majority vote.

External Examiner:	Muhammad R. Hajj Professor, Dept. of Biomedical Engineering and Mechanics Virginia Polytechnic Institute and State University — VT
Supervisors:	Raafat Mansour Professor, Dept. of Electrical & Computer Engineering, University of Waterloo Eihab M. AbdelRahman Professor, Dept. of Systems Design Engineering, University of Waterloo
Internal Members:	Dayan Ban Professor, Dept. of Electrical & Computer Engineering, University of Waterloo Bo Cui Professor, Dept. of Electrical & Computer Engineering, University of Waterloo
Internal-External Member:	Mustafa Yavuz Professor, Dept. of Mechanical and Mechatronics Engineering University of Waterloo

I hereby declare that I am the sole author of this thesis. This is a true copy of the thesis, including any required final revisions, as accepted by my examiners.

I understand that my thesis may be made electronically available to the public.

Abstract

The need for investigation and characterization of physical, chemical and structural properties of material surfaces at the micro and nano scales led to the invention of Atomic Force Microscopy (AFM) in 1986 as a successor to the well-known Scanning Tunneling Microscopy (STM) to overcome the main shortcoming of STM, which worked only on conducting or semiconducting materials. In fact, the idea of AFM is predicated on the measurement of inter-atomic interaction forces between the molecules of a sharp stylus at the end of a silicon probe and the molecules of a specimen, when the tip comes to close proximity (less than 100nm) of the sample.

It detects the height of the probe hovering above the specimen surface by measuring the tip deflection, or the amplitude and frequency of its vibration. In each case (mode), the interaction forces between the sharp tip and the specimen govern the measured parameter which is detected optically by a laser beam reflected of the probe back side. A piezoelectric actuator drives the probe vibrations and Z-axis motions. Optical detection and piezoelectric actuation contribute significantly to the price and complexity of traditional AFM systems.

In this research effort, we use electrostatic actuation and capacitive motion detection of off-shelf AFM probes via electrodes printed on a Printed Circuit Board (PCB), thereby eliminating the optical and piezoelectric components of traditional AFMs, drastically reducing its cost, size and complexity as well as enabling new AFM operating modes. Two configurations for the probe-electrode system were modeled, simulated and demonstrated experimentally. The actuation voltage contains DC and AC components while the actuation frequency is set close to the probe natural frequency. Model and experimental results show that the DC component controls the operating point (static gap between the electrode and the probe) and the AC component controls the sensitivity of the AFM.

The detector output current is first amplified using a low-noise transimpedance amplifier. Next, a lock-in amplifier measures the magnitude and phase of the current at the second harmonic of the actuation frequency which is directly related to the tip-sample separation. This detection method overcomes the effect of large parasitic capacitance. It enables us to sketch two-dimensional maps of the current's magnitude or phase representing the specimen's topography.

To improve sensitivity, the static distance between the probe's tip and the specimen was set to operate the AFM in intermittent (tapping) mode. A nano-stage was developed for this purpose. It allows us to raster scan the specimen surface. In future work, automatic closed-loop feedback control should be deployed to manage the height of the AFM tip over

the specimen. A resonant drive and detection scheme should also be used to miniaturize the footprint of the AFM system to a few centimeters.

Acknowledgements

I would like to express my sincerest gratitude to my supervisor Dr. Eihab Abdel-Rahman for the immeasurable amount of support, encouragement, and guidance he has provided throughout this study. Dr. Abdel-Rahman's insights into and patient endurance throughout this project have been a true blessing. It is with great pleasure that I also thank my supervisor Professor Raafat Mansour. Many detailed and in-depth discussions with him have invaluably shaped the course of this research. Their extensive knowledge, vision, and creative thinking have been the source of inspiration for me throughout this work. I am honored to have supportive and professional supervisors like them.

I would like to express my profound gratitude to my advisory committee members Professor Dayan Ban, Professor Bo Cui and Professor Mustafa Yavuz, who were always ready to answer my questions and have provided me with constructive guidance and criticism for several years to improve this thesis to a great extent, and Professor Amir-Hamed Majedi, who has provided me with extensive advice and encouragement throughout the early stages of my time as a PhD student.

I would also like to especially thank Dr. Sangtak Park for his brilliant ideas in test and measurement methods, Dr. Neil Sarkar for technical discussions and support in scanning probe microscopy, and Dr. Mahmoud Khater for his knowledge transfer and support in theoretical problems.

I am very grateful to all my lab colleagues and friends, faculty and staff at the Electrical and Computer Engineering, and Systems Design Engineering Departments, members of the CIRFE Lab and members of the Nano and Micro Systems Lab. The enlightening discussions and the overall atmosphere and spirit have made my academic life pleasant and enjoyable. I never can forget about all the help and support by Andrew, Brian, Greg, Jorge and Phil in the Engineering Student Machine Shop and Dr. Yuquan Ding in Materials Lab.

Dr. Luis Gonzales, Dr. Tylan Das and Mr. Mahdi Beedel, I would like to express my heartfelt thanks to each and every one of you for supporting me in your own personal way; for making it possible for me to realize so many meaningful moments in my "PhD life" and to be able to enjoy graduate study in the moment. Your daily laughter and smiles have made my time as a PhD student extremely enjoyable and absolutely unforgettable.

I would especially like to thank my reliable and true friend Dr. Mohammad Eram, who always provided me with great advice and support, thanks for all the great conversations and shared moments during both good and bad times.

To my dearest teachers in life, my parents, Fatemeh and Reza. I am forever highly indebted to you. I would also like to thank my sisters, Zohreh, Nahid, and specifically Nafiseh for their love and support. Indeed, Nafiseh was the one who took the first step to bring me to the academic environment at the University of Waterloo.

Last, but most important, is my grateful appreciation to my beloved wife, Tahereh, and dearest, Narges and Amir-Hossein, for giving me the opportunity to follow my dreams and the love to make them a reality. How would I ever accomplish anything without your patience, sacrifice and your unconditional love, support, and encouragement? You always stood by me and believed in my ideas, providing a source of unending strength and support.

Finally, I achieve nothing without the grace of God, the devotion from my teachers, and the support of my family.

Dedication

Dedicated to my beloved wife, Tahereh,

my parents,

and

my children

for their love and encouragement during the past years.

Table of Contents

List of Tables

List of Figures

Abbreviations

AFM Atomic Force Microscope 1, 2, 10, 15, 33, 37

AM-AFM Amplitude modulated-AFM 2

CMOS Complementary Metal-Oxide Semiconductor 14, 24, 26

EAFM Eelctrostatic Atomic Force Microscope xvi–xviii, 46, 55, 66, 72, 74, 75, 83, 92, 95, 98, 100, 102, 103, 113, 118, 124, 127

FM-AFM Frequency modulated-AFM 2, 126

MEMS Microelectromechanical System 14, 15, 20, 22–25, 30, 31

MOSFET Metal-Oxide-Semiconductor Field Effect Transisitor 26

PCB Printed Circuit Board 7, 35, 37, 40

PID Proportional Integral Derivative 115–117

PLL Phase Locked Loop 2, 115

SEM Scanning Electron Microscope 17, 20

SMM Scanning Microwave Microscopy 26

SOI Silicon On Insulator 17, 30

SPM Scanning Probe Microscope 1, 2, 4, 6, 9, 10, 34

STM Scanning Tunneling Microscope 1, 3, 4, 20

VCO Voltage controlled oscillator 51

VGA Variable Gain Amplifier 28

Chapter 1

Introduction

Scanning Probe Microscope (SPM) is one of the crucial methods for characterization of surface physical properties at micro or nano scale. The invention of Scanning Tunneling Microscope (STM) in the early 80's and Atomic Force Microscopy Atomic Force Microscope (AFM) in the mid 80's opened new horizons for detection of physical properties and structure of specimen. AFM offered the additional ability to manipulate surfaces at the atomic scale, thereby allowing new technologies in diverse areas of research and industry, such as insertion of magnetic and electric charges at nano-scale.

AFM and, more generally, SPM rely on the detection of inter-atomic interactions between the probe and the surface of interest. A vast variety of physical properties underly this interaction and, hence, there is a wide range of SPM types. But the basic mechanism is the same: a sense probe, usually a microscale silicon cantilever, and a laser beam. The free end of the cantilever carries a sharp stylus with a tip radius in the range of several micrometers to several nanometers. The tip is brought in proximity of a target surface to take a 'measurement'. The coating of the microbeam and stylus, the frequency of its

oscillations, the separation distance between the tip and surface and the mode of operation are managed to detect different physical properties and spatial information.

1.1 Background

State-of-the-art SPM systems are multipurpose instruments supporting various microscopy modes. They utilize piezoelectric actuators to manage the separation distance between the tip and surface and to scan the tip over the surface. Broadly speaking, AFM modes can be classified into static and dynamic modes. In static modes, the actuator merely controls the height of the tip over the surface as the laser beam measures the probe deflection under the tip-surface interaction forces. The deflection can be mapped versus the spatial coordinates as a measure of the physical property underlying the interaction force to produce an 'image'of the physical property over the specimen's surface. In dynamic modes, the actuator drives the probe to oscillate at a fixed frequency as the laser beam measures the amplitude, phase or frequency of oscillations. The variation of these properties may be extremely small, however, thanks to advanced electrical measurement techniques, they can be detected and mapped in associate with surface coordinates to produce the image.

- In Amplitude modulated-AFM (AM-AFM), the amplitude of oscillation is measured as it changes as a function of the interaction forces between the tip and surface. These forces affect the probe's instantaneous stiffness and/or damping.
- In Frequency modulated-AFM (FM-AFM), the shift in vibration frequency from the excitation frequency due to the surface forces is measured. A Phase Locked Loop

(PLL) detects this shift and use it as measurand.

Depending on the distance between the tip and specimen surface, AFM modes can also be broken into four standard modes:

- **Contact Mode:** The tip comes into contact with the specimen surface with a constant force as the laser beam measures its deflection of peak frequency. It then retracts and moves to the next point in the scan to repeat the process.
- **Non-contact Mode:** The tip hovers over the surface at a controlled height as surface forces affect the overall force applied to the probe.
- **Intermittent Mode:** A combination of the previous modes benefiting from the advantages of both. The tip touches the surface temporarily while oscillating. This method, also called *tapping mode*, is specifically useful for soft specimens, such as living cells and soft polymers.
- **Lateral Force Microscopy:** The probe, in this mode, does not oscillate transversally, but in torsional motion.

1.2 Motivation

Atomic Force Microscopy was invented by Binnig, Quate and Gerber in 1985 [10] as a successor to STM to overcome its limitation to conducting and semi-conducting surfaces. AFM measures the interaction forces between the atoms (molecules) of a sharp stylus and

molecules of the specimen, when the tip is in close proximity (less than $100nm$) of the sample. STM measures the tunneling current between the molecules of the sharp tip and specimen.

The AFM cantilever scans the surface in a raster fashion. For each point of the surface (depending on the resolution of measurement), the system measures the interatomic forces and eventually generate a spatial map of those forces. For instance, in non-contact AFM, van der Waal force is dominant and because of the relationship between van der Waal forces with the separation distance [28, 30], the output of AFM is the topography of the specimen's surface. This is the reason for using the more prevalent term SPM.

The main advantage of AFM is that it can work almost on any type of material, in nearly any type of environment (liquid, air, vacuum), and in a wide range of temperatures. However, one of the most spectacular advantages of AFM is the ability to measure other interaction forces. For example, by selecting probe geometry, size, material and/or coating as well as tip-sample distance and scanning speed, we can measure electric, magnetic, and chemical properties. These features extend the abilities of AFM to microscopy, spectroscopy, metrology, surface manipulation, living cell observation and other applications [32].

As a result, state-of-the-art AFM systems are comprehensive, large, bulky and expensive systems. On the other hand, proliferation of these advanced equipments can popularize their application and accelerate related research. Miniaturization and integration represents an appealing alternative to shrink down the size and price of AFM systems. Specifically, advances in micreoelectromechanical systems (MEMS) and microfabrication

methods and materials facilitate the integration of new transduction technologies into scanning probes and an XY scanner in order to convert the probe deflection directly to electrical signal for further processing. The final goal for many research groups is a single-chip AFM [50, 49, 5, 46].

The traditional way of detecting probe deflection is based on converting the displacement of a laser beam reflected from the backside of the probe to an electrical signal using a four quadrant photodiode. This part of conventional AFM systems is not only one of the most expensive and massive components, but also needs a lot of workmanship. Modern systems, have seen incremental improvements to automate this process. But it remains a hurdle stimulating research to find other detection methods.

The most popular transduction methods include electrostatic, electro-thermal, piezoelectric, electromagnetic and piezoresistive. Electrostatic transduction was the primary concern in this research because it facilitates the integration of actuation and detection in one device compatible with microfabrication and exploits advances achievable on both fronts to greatly simplify the whole system. The idea is to create an AFM system which exploits commercially available AFM probes. Very few researchers have addressed the integration of electrostatic actuation and detection in one device and those who did were limited to the use of proprietary micromachined devices.

1.3 Objectives and Significance

Previous attempts at miniaturization of SPM systems relied on proprietary MEMS designed for special purposes, such as high-speed microscopy. These systems called for complicated microfabrication processes. In this research, the flexibility of electrostatic actuation and detection is exploited to integrate the sensor, the actuator and off-shelf AFM probes on a single inexpensive board. The ultimate goal is the development of inexpensive multipurpose SPM. As an initial step, the integrated system is implemented for non-contact AFM.

The challenge of the high drive voltages typically needed for electrostatic actuation, will be addressed via a technique dubbed resonant drive that employs a modulated signal where the carrier frequency is tuned to match the resonance frequency of an RLC circuit and the base frequency is tuned to match the natural frequency of the probe. The interaction between the electrical and mechanical resonances also provides a tool for observation of the amplitude, phase and frequency of the base signal driving the probe oscillations, via measurements of the current induced by its motions.

Finally, this research will exploit a closed loop control scheme to manage the excitation voltage applied to the capacitive actuator. This will control the steady-state height of the stylus over the scanned surface and limit the potential for onset of instabilities in the probe oscillations. In fact, the output of the control block constitutes the topography information obtained from the AFM.

1.4 Challenges

The first challenge is the design and construction of an AFM system that can attain microscale accuracy with the least use of microfabrication facilities. The least expensive technology available for this purpose is Printed Circuit Board (PCB) technology limited by high manufacturing tolerances.

The second challenge is accurate measurement of currents on the order of pico-to-nano Ampere which has direct bearing on the quality of oscillation measurement and image resolution. The mathematical model deployed to interpret current measurements as capacitance and probe oscillations is another substantial challenge addressed in this research.

Electrical noise in circuits and mechanical noise in the probe oscillations are significant sources of disturbance in the final product of the system: topography measurements. The impact of these disturbances were compensated via measurement circuits configuration, post-processing tools and use of vibration isolators. The goal of microscopy is to produce images or spatial maps of the surface physical property by converting the analog output of the AFM to well processed digital images. We used MATLAB tools to accomplish this step and obtain the scanned data in two-dimensional representation.

1.5 Outline of the Thesis

This thesis is composed of six chapters. The first chapter introduced the main ideas of this research, its context, motivations and objectives as well as the challenges addressed in this

project.

The second chapter reviews relevant literature including fundamentals of electrostatic actuation and previous attempts at miniaturization of AFM. This review also covers different integrated actuation and detection methods while stressing those employing electrostatic actuation and sensing.

The third chapter is dedicated to the electrostatic AFM devices and fixtures developed for experimental demonstration. This is the stepping stone to chapter four which describes the analytical models of the AFM subsystems. It covers static analysis of the first generation AFM and dynamic analysis of the second generation AFM in tapping mode. Towards that end, the model incorporates van der Waal force to examine its effect of the probe tip displacement and velocity.

For the numerical simulations, we used COMSOL to investigate the multiphysics governing the function of the second AFM device. In this chapter we will also propose the underlying theory of the project's main contribution, namely the relation between the cantilever's mechanical displacement and the measured current. The commercial partial differential equation solver, COMSOL, is deployed for the numerical simulations of the multiphysics governing the second generation AFM. This chapter also addresses the theory underlying the project's main contribution, namely the relation between the probe tip displacement and the measured motion induced current.

The fifth chapter presents the electrostatic AFM experimental results in three sections. First, the results of tapping mode AFM is introduced covering the probe's behavior as it touches the sample's surface and comparing the measured current output with the analyt-

ical and numerical results. A goal of this step is finding the optimal distance between the probe and the sample by deriving the AFM calibration curve. This curve is crucial for the start of scanning.

The second section reveals the results of line scans in tapping mode using unknown samples. This experiment aimed to check whether the output current resembled the surface pattern while scanning a single line. Repeated line scans were undertaken with varying lengths to investigate the repeatability of the measured current for the same line scans.

In third section, we performed raster scans of a calibration grating sample with a fixture exploiting an XY-stage. First, the results of a manual raster scan are presented before and after post-processing. Then results of a semi-automatic raster scan, utilizing a closed-loop motorized XY-stage, are presented.

The last chapter contains conclusions about the methods and equipment used in this research and how they can be improved to achieve a multipurpose SPM.

Chapter 2

Literature Review

This chapter reviews attempts to integrate actuation and sensing mechanisms with AFM probes. Since the early days of SPM, there has been a persistent endeavor to unify disparate parts of the system as mentioned in section 1.2 utilizing MEMS ability to incorporate piezoresistive, piezoelectric, electrothermal and electrostatic sense and actuation. Hence, researchers have been using these properties to design proprietary MEMS to integrate the AFM subsystems in a single-chip.

2.1 Integrated Actuation Schemes

Integrated actuators have been used in AFM for two purposes: to actuate the AFM probe in a normal direction to the sample surface and to provide planar (XY) motion of the probe tip or the sample. In the following, the most significant examples of these efforts will be investigated.

2.1.1 Electrostatic Actuation

Among all types of electrical actuators, electrostatic actuators have a vast diversity of applications because of their native compatibility with MEMS technology and configurations. These actuators are easily implemented in microstructures, such as beams and membranes, within three broad classes:

1. **Parallel-Plate Actuators:** Two parallel 'plates'make a capacitor. One or both plates are suspended by appropriately designed tethers to enable motion. Figure 2.1 shows an example of a parallel-plate actuator. where l, b, h are the plate's length,

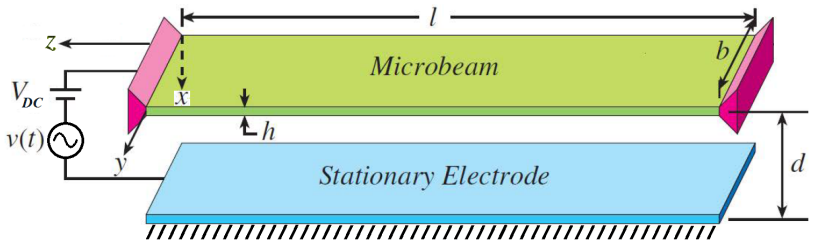

Figure 2.1: Schematic of a parallel-plate electrostatic actuator. [1] (reproduced by confirmation number 11716336 dated 07/May/2018 from Copyright Clearance Center).

width, and thickness, respectively, and d is the gap between the two plates at rest. By applying a voltage drop V between the plates, the resultant electrostatic field causes an attraction force between the plates

$$F_{es} = -\frac{\epsilon A_{eff} V^2}{2(d-x)^2} \tag{2.1}$$

where ϵ is the permittivity of the medium filling the gap, A_{eff} is the effective overlap-

ping area between the plates and x is the relative displacement caused by electrostatic attraction. This type of electrostatic actuator is used mainly in RF switches [39] and RF tunable capacitors [16].

2. **Comb-Finger Actuators:** This actuator is made of a set of parallel-plate actuators with interdigitated fingers in various comb-like configurations as shown in Figure 2.2. The fingers may or may not overlap.

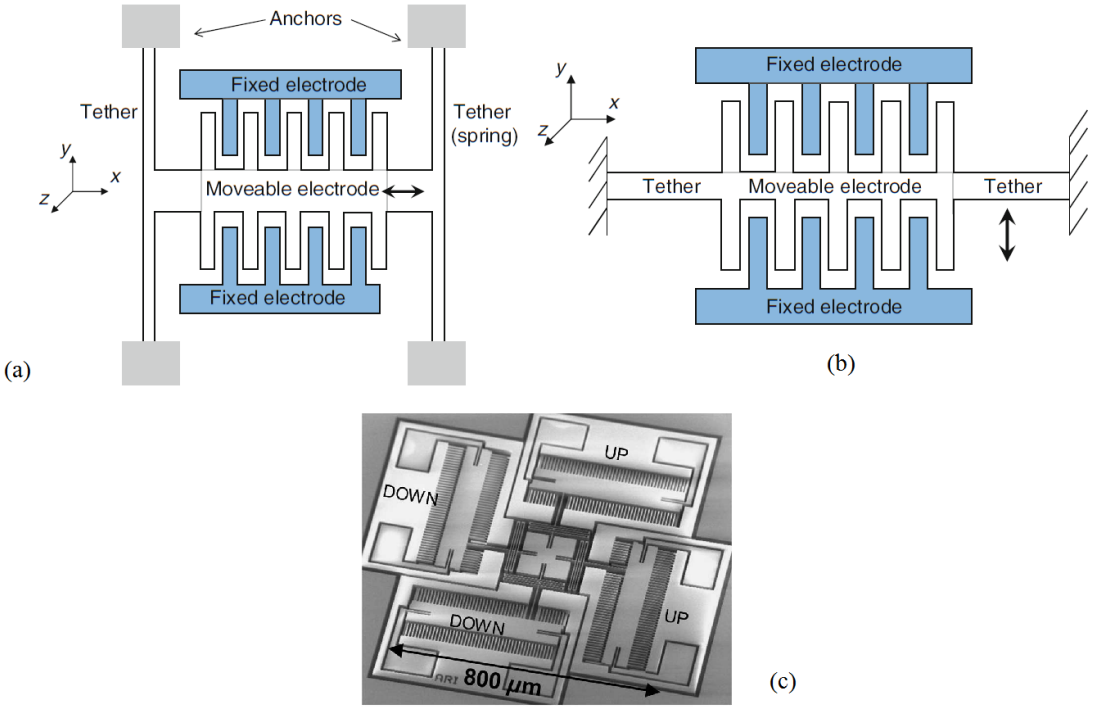

Figure 2.2: Three types of overlapping comb-finger actuators. Schematics of (a) laterally moving and (b) longitudinally moving comb-finger actuators [58], (reproduced by confirmation number 11716339 dated 07/May/2018 from Copyright Clearance Center). (c) SEM micrograph of a staggered comb-finger [33] (Copyright ©2004, IEEE).

Depending on the relative motion of the combs, they are classified into laterally

moving, longitudinally moving and staggered [33] comb-fingers. Staggered comb fingers, Figure 2.2c, facilitate rotary motion around one or two axes and are mainly used in micromirror applications.

The total force of the moving comb in longitudinal comb-finger actuators, Figure 2.2b, can be calculated by [51, 58]

$$F = \frac{\epsilon n t V^2}{d} \tag{2.2}$$

where n is the number of finger units (two facing plates), t is the thickness of the fingers and d is the gap between the 'faces'of two adjacent fingers. The interesting point in this actuator is that the force does not depend on the overlapping area of fingers. Movements in y direction do not affect it, unlike parallel-plate actuators, hence, the force is linearly proportional to the voltage squared V^2. Dependence of the number of fingers n shows that comb-finger actuators can provide high forces.

3. **Torsional Actuator:** This type of actuator usually is composed of a plate, able to turn around an axis, a 'hinge'. There can be one or more electrodes beneath the swinging plate as shown in Figure 2.3 to provide voltage drop relative to the plate. This type has a wide usage in micromirrors and reflective light projection applications. The electrostatic torque can be calculated from [58]:

$$M_e = \frac{\epsilon b V^2}{2\alpha^2}\left[\frac{d}{d - a_2\alpha} - \frac{d}{d - a_1\alpha} + \ln\left(\frac{d - a_2\alpha}{d - a_1\alpha}\right)\right] \tag{2.3}$$

where b is the plate length (into the page) and the other parameters appearing in the

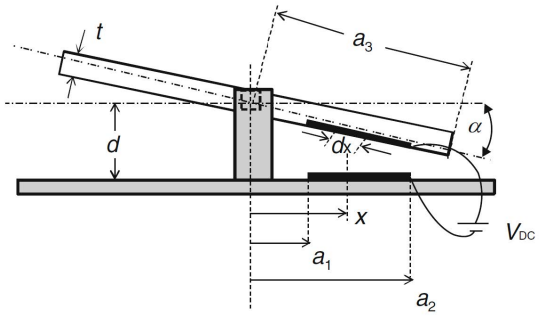

Figure 2.3: Schematic of a torsional electrostatic actuator [58], (reproduced under the confirmation number 11716339 dated 07/May/2018 from Copyright Clearance Center).

equation are illustrated in Figure 2.3.

The advantages of electrostatic actuation compared to other techniques are worth pointing out to understand the reasons this method is of high interest. Electrostatic actuation is consistent with the nature of Microelectromechanical System (MEMS) and Complementary Metal-Oxide Semiconductor (CMOS)-MEMS. Unlike piezorelectric actuators and piezoresistive sensors, it does not require the use of a specific material or deposition of extra layers. No external fields are required, as is the case for electromagnetic actuation. As a result, the complexity of the actuator structure, design and fabrication is far less than that for other actuation techniques. Power consumption is also very low because of low currents involved in capacitive devices. However, energy density is quite high. Electrostatic actuators are very flexible and therefore can be well controlled [54]. Further, because of their dependence on low capacitance values, their response time is shorter than any other actuation method.

The most significant drawbacks of electrostatic actuator are the high actuation voltage

requirements and nonlinear behavior. The latter can be quite problematic because it can lead to instabilities and failure through stiction of capacitor plates.

Next, the integration of electrostatic actuators into AFM will be reviewed in the literature.

Electrostatic Actuation of AFM Probes

All three types of electrostatic actuators have been used in conjunction with custom-made MEMS to miniaturize conventional AFM systems. Below, the most relevant efforts have been reported.

Long et al. [31] installed commercial AFM probes onto a specially designed MEMS fixture. A fixed electrode, as depicted in Figure 2.4, is placed on top of the probe where a laser beam is also directed. The electrode actuates the probe via common and differential mode voltages while the laser beam measures its oscillations. The gap between the electrode and the probe is adjustable.

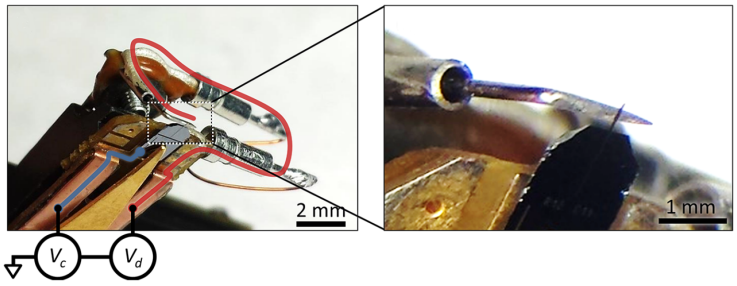

Figure 2.4: Electrostatically actuated off-shelf AFM probe [31] (license).

Brugger et al. [13, 12] undertook the first effort to introduce electrostatic actuation and

sensing to AFM. They developed a probe made of a microbeam and a counter electrode fabricated by silicon bulk micromachining as the actuation and sensing subsystems as shown in Figure 2.5. They produced devices with different lengths, for example a $800\mu m \times 40\mu m \times 5\mu m$ cantilever had a natural frequency of $f_n = 10\,\text{kHz}$ and a spring constant of $k = 0.5\,\text{N/m}$. The gap between the microbeam and the counter electrode was $3\mu\text{m}$ producing a capacitance of $100fF$. Three years later, Blanc [11] presented an array of AFM probes based on configuration of Brugger et al.'s integrated probes.

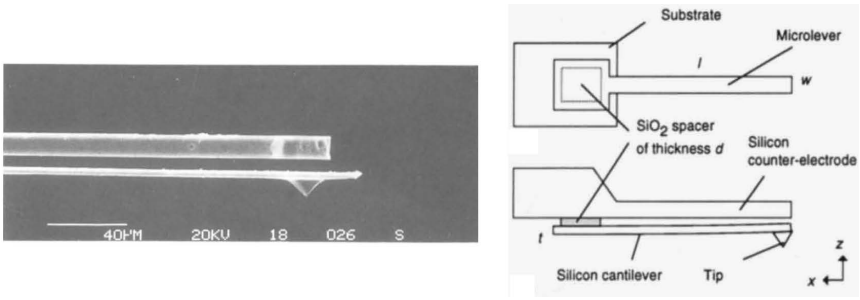

Figure 2.5: Brugger et al.'s electrostatically actuated AFM probe with integrated detection [12] (reproduced under the license number 4344290287168 dated 08/May/2018 from Elsevier and Copyright Clearance Center).

These two systems are the closest to achieving the main objective of this research, an integrated AFM system. However, the fall short in the former because of the use of optical detection and in the latter because of their use of proprietary probes and a pedestrian implementation of capacitive sensing.

Müller et al. [35] designed and fabricated a parallel plate actuated AFM device (Figure 2.6) with an array of two tips including separate parts for actuation and detection. The tips are actuated with a voltage applied to the electrostatic actuator and its current is mod-

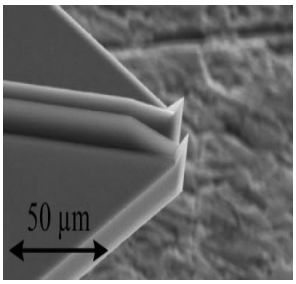

(a) SEM image of the tips

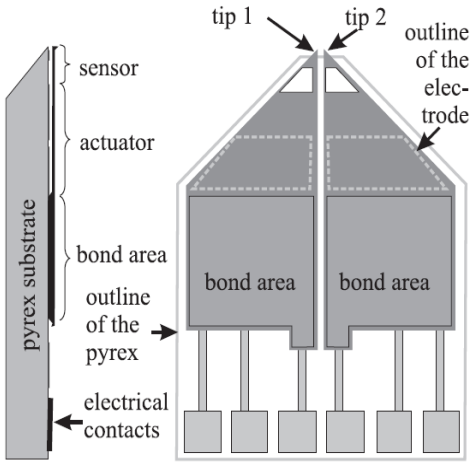

(b) Schematic drawing of AFM device with two sets of electrostatic actuation and detection membranes and two tips

Figure 2.6: Electrostatically actuated and detected AFM device and test setup presented by Müller et al [35] (reproduced under written permission of Japan Society of Applied Physics dated 09/May/2018).

ulated by the surface forces which change during scanning as the gap between the sample and the tip changes due to the sample's vertical movement. The actuator part consists up of a metallic bottom electrode and a moving membrane with an area of $0.5mm^2$ and the gap of $10\mu m$ while the triangular cantilever is at the endmost of the membrane. The third mode shape of this structure has a node exactly at the point the cantilever starts so Müller used the actuator's third eigenfrequency (around $140.6kHz$) for excitation. The detection scheme will be declared in section 2.2.1. Figure 2.6a shows an Scanning Electron Microscope (SEM) picture from the tips and Figure 2.6b shows the device schematic drawing. Geerlings et al. [21] in 2014 used the parallel plate principle to design a micromachined cantilever and integrated in-plane tip based on Silicon On Insulator (SOI) process as shown

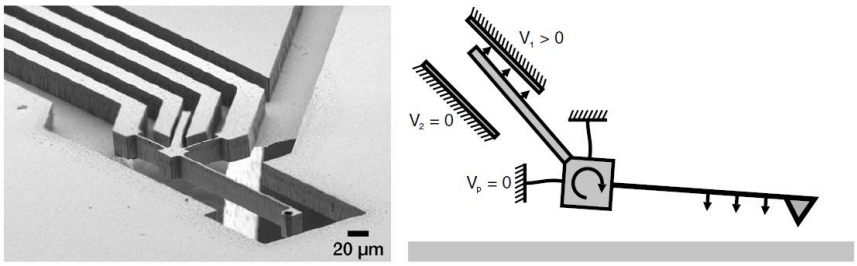

Figure 2.7: Electrostatically actuated AFM cantilever proposed by Geerlings et al. [21] (reproduced under the confirmation number 11716355 dated 08/May/2018 by Copyright Clearance Center).

in Figure 2.7.

This design had the potential of batch processing and the experiments based on optical detection showed the feasibility of the function. The actual resonant frequencies for different cantilevers with different lengths were from $35.6kHz$ to $56.3kHz$. The shortest cantilever with $100\mu m$ length showed $1.8\mu m$ displacement in its resonant frequency at $56.3kHz$ measured with stroboscopic video microscopy. The actuation voltage for this experiments was $20V_{pp}$.

Akiyama et al. [3] showed a cantilever equipped with two comb-drive actuators in either side of the cantilever to produce out-of-plane movement as shown in Figure 2.8. The dynamic range of this design was $1\mu m$ with a $11.4nm/V$ efficiency. The imaging bandwidth was reported as $80kHz$.

In 1997, Miller et al. [34] designed an array of a combined mechanism of comb-finger drive and torsional actuators proposing an out-of-plane movement of $\pm 0.7\mu m$ at the resonant frequency of $68.6kHz$ and $20V$ actuation voltage. They also utilized an integrated sensing technique based on capacitance measurement. The structure of Figure 2.9 has a

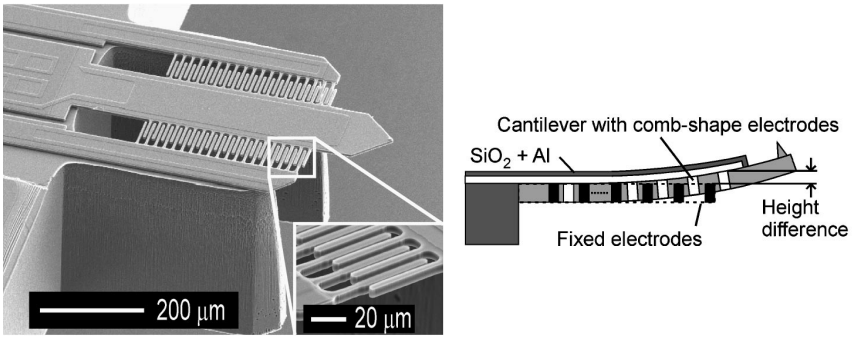

Figure 2.8: Electrostatically actuated AFM cantilever proposed by Akiyama et al. [3] (reproduced under the license number 4344240323803 dated 08/May/2018 by AIP Publishing and Copyright Clearance Center).

total area of $1.5\mu m \times 1.5\mu m$ and an array of 12×12 probes in an area of less than $1cm^2$ produces a device appropriate for surface manipulation with high throughput. For instance, Information storage, molecular manipulation, and nanolithography are a few examples worth to mention.

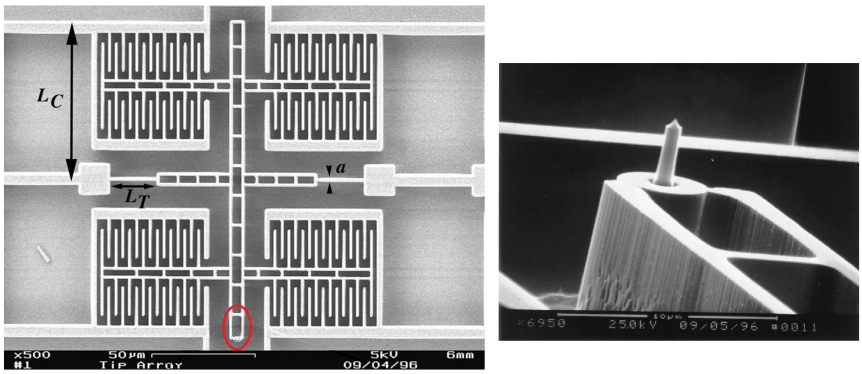

Figure 2.9: Electrostatically actuated AFM cantilever proposed by Miller et al. [34] (reproduced under the license number 4344240516659 dated 08/May/2018 by AIP Publishing and Copyright Clearance Center).

Tabak et al. [52, 18] used the PolyMUMPs process based on parallel plate technique to design a special MEMS-based z-scanner for out-of-plane movement of the stylus in high frequency for high speed AFM and STM applications. The MEMS membrane was suspended by four crab-leg springs. The resonance frequency of their structure was 186 kHz. Figure 2.10 shows the SEM micrograph of the device.

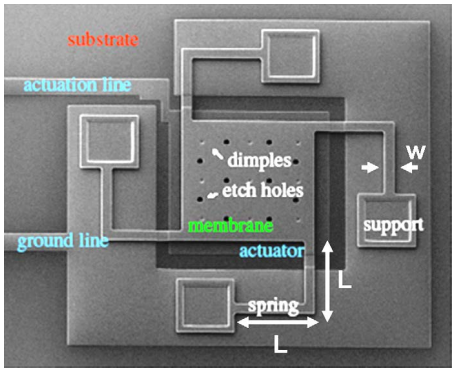

Figure 2.10: Electrostatically actuated AFM membrane proposed by Tabak et al. [52] (reproduced under the license number 4344240781734 dated 08/May/2018 by Elsevier and Copyright Clearance Center).

There have also been several attempts to design and produce XY scanners based on electrostatic actuators specially comb-finger drives [37, 24]. Here, two reports as samples for miniaturization will be introduced.

Olfatnia et al. [37] demonstrated a MEMS-based XY-microstage utilizing comb-finger actuators depicted in Figure 2.11. This two degree of freedom scanner proposes a wide scanning range which facilitates many applications including scanning probe microscopy.

This group reported a displacement range of $225\mu m$ per axis with the bandwidth of 400 Hz. This bandwidth is high enough to support many high speed scanning probe microscopy applications.

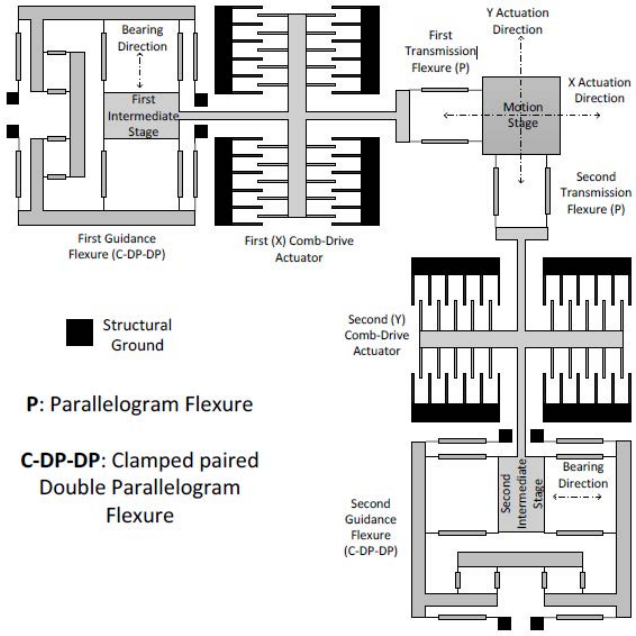

Figure 2.11: Electrostatically actuated XY- microstage presented by Olfatnia et al. [37] (reproduced under the license number 4346090676095 dated 10/May/2018 by American Society of Mechanical Engineers and Copyright Clearance Center).

In 2017, Ruppert et. al. [46] reported a single-chip AFM device depicted in Figure 2.12, including the electrostatic XY-scanner for horizontal movement of a cantilever which is actuated by a piezoelectric layer at its base. Ruppert achieved scanning frequencies of 2.85 kHz in the X direction and 2.77 kHz in the Y direction while they scanned the imaging sample in a $8\mu m$ by $8\mu m$ frame. They utilized the piezoelectric property for both actuation and sensing the AFM's cantilever.

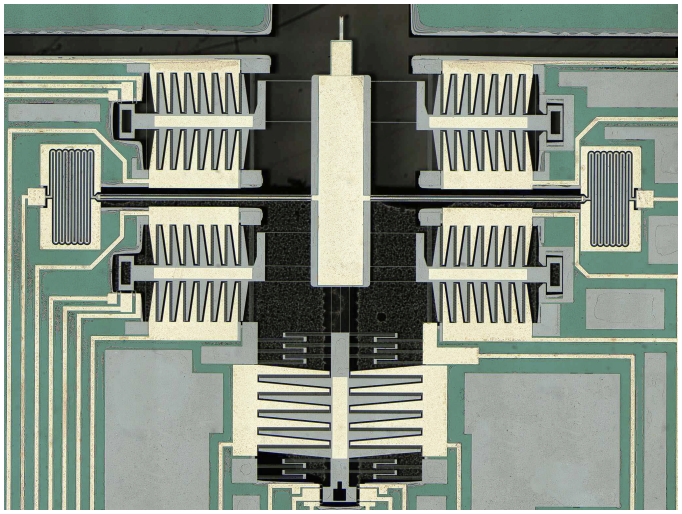

Figure 2.12: Electrostatically actuated XY-scanner for the AFM's cantilever by Ruppert et al. [46] (Copyright ©2017, IEEE).

Resonant Drive

Electrostatic actuators usually require high voltages for drive. Consequently, they need high voltage amplifiers and high voltage power supplies which leads to bulky and complicated systems and contradict the backbone idea of my research, miniaturization.

An appropriate approach to overcome this challenge is the use of resonance effect in the electrical drive circuits [42, 56]. To put it simple, by integrating the capacitance of a MEMS actuator into a resonant RLC circuit, a mixed signal made of a low-frequency (baseband) actuation signal and a high-frequency carrier signal in the configuration of Double Side Band Large-Carrier Amplitude Modulation can be magnified to drive the MEMS actuator with a high voltage.

Magnification is obtained by tuning the carrier signal frequency to match the RLC

circuit's resonant frequency. This is called the *Electrical Resonance* and the magnification ratio is equal to the resonant circuit's quality factor Q_L. The frequency of the baseband (modulating) signal is equal or near the resonant frequency of the MEMS device to achieve the highest displacement. This is called *Mechanical Resonance* and the quality factor of mechanical resonator is Q_M.

This actuation scheme is depicted in Figure 2.13. The overall quality factor of the resonant circuit Q_T, calculated from Equation (2.4), determines its dynamic amplification and therefore gain.

$$\frac{1}{Q_T} = \frac{1}{Q_L} + \frac{1}{Q_M} \tag{2.4}$$

MEMS electrostatic actuators usually have very high quality factors so the limiting pa-

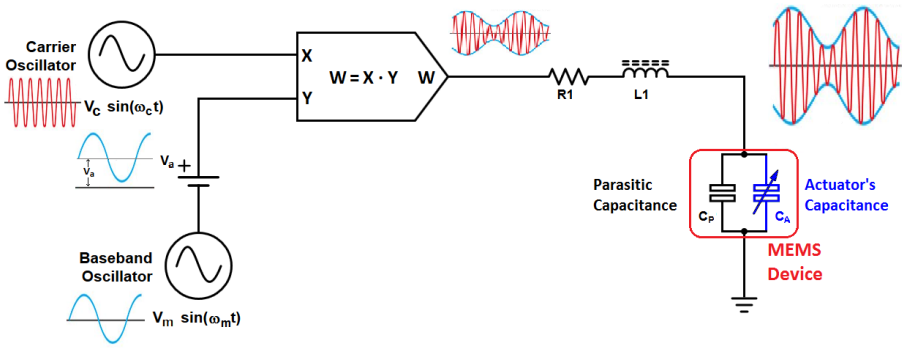

Figure 2.13: The basic concept of resonant drive actuation for electrostatic MEMS.

rameter for Q_T in Equation (2.4) will be Q_L. It means this technique needs very high quality factor inductors.

The capacitance of the MEMS electrostatic actuator demodulates the actuation signal. Consequently, only the magnified low frequency signal is left to drive the MEMS actuator.

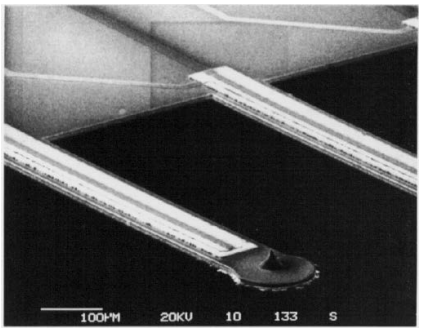

Figure 2.14: Piezoelectric integrated cantilevers by Indermuhle et al. [25] (reproduced under the confirmation number 11716448 dated 08/May/2018 by Institute of Physics Publishing and Copyright Clearance Center).

2.1.2 Piezoelectric Actuation

Piezoelectric actuation is the dominant method of actuating the AFM probe holder and/or sample stage in conventional AFM systems. These actuators have a large volume relative to the sample of interest. A great trend in MEMS research exists to integrate the AFM probe's actuation with the piezoelectric layers on the cantilever. Despite of some drawbacks of piezoelectric devices like nonlinearity with respect to actuation voltage, drift and incompatibility with standard CMOS fabrication process, this technique is still in the center of interest as a step toward miniaturization of AFMs.

As an example, Indermuhle et al. [25] fabricated cantilevers with $700\mu m$ length, piezoelectric layers for actuation and detection and integrated tips. They exploited the first resonance frequency for imaging a grid with a $1\mu m$ period and $15nm$ vertical steps. Figure 2.14 illustrates the cantilever array.

2.1.3 Electrothermal Actuation

This type of actuation is common in microelectromechanical devices because of geometric simplicity and compatibility with MEMS processes. Electrothermal actuation is established on the principle of the expansion of substructures due to increase in temperature. In fact, the main way of heating up the parts in a MEMS device is passing electric current through the part. Two methods are common for this purpose, depositing resistive materials on the desired substructure, and passing the current through the part itself. The former method which is called *Bimorph Method* is able to produce out-of-plane movements by selecting two similar movable devices connected together but with different resistances [58]. The second method, which is best for in-plane movements, is implemented by several well-known structures like U-shape structure which uses two legs with unequal cross sections but similar thermal expansion coefficients. The smaller cross-section shows higher resistance and produces more heat by passing the same current as the thicker leg. Consequently, the thinner leg will experience more expansion and causes a displacement.

While thermal actuation is advantageous in easiness, it suffers from several disadvantages which drop it from the list of possible actuators in high frequency AFMs. The most important drawback is high time constant of the actuation system to reach temperature equilibrium in each actuation cycle. The other difficulty with thermal actuation is its interference with surrounding environment which results in low actuation efficiency. For these reasons, miniature atomic microscopes which benefit the thermal actuation are mostly designed to work in contact mode. Two major examples of integrated actuating and reading schemes will be presented in the following.

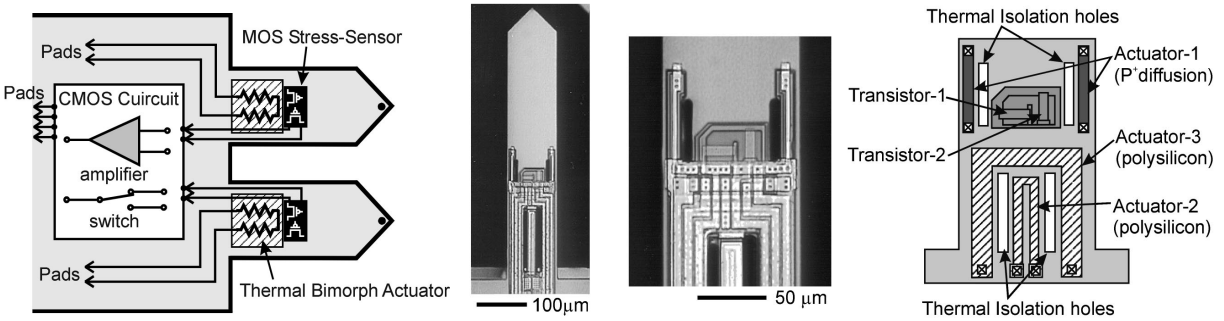

Figure 2.15: Electrothermal actuated AFM design proposed by Akiyama et al. [2] (reproduced under the license number 4344260259380 dated 08/May/2018 by AIP Publishing and Copyright Clearance Center).

Akiyama et al. [2] demonstrated a full custom-made cantilever array design (Figure 2.15) combined with thermal bimorph actuators as the primary out-of-plane actuator and feedback actuators. They used a metal oxide field effect transistor (Metal-Oxide-Semiconductor Field Effect Transisitor (MOSFET)) stress sensor integrated in the cantilever as the force detection mechanism along with on-chip CMOS circuitry.

Sarkar [50] designed the first-in-the-world single-chip contact mode atomic force microscope using the CMOS-MEMS technology employing electrothermal bimorph actuators for both XY scanning and Z-movement of the cantilever. Figure 2.16a shows the geometry of this design. In Figure 2.16b we can see the lateral actuator, and the transversal actuator is illustrated in Figure 2.16c. The XY scanner is able to cover a $10\mu m$ by $10\mu m$ area and the range of vertical scanning is $30\mu m$. This design facilitated one of the most compact complete designs of AFM systems which integrated all actuators and detectors needed for an AFM scan. It also opened a window toward other types of scanning probe microscopy techniques like Scanning Microwave Microscopy (SMM). [5].

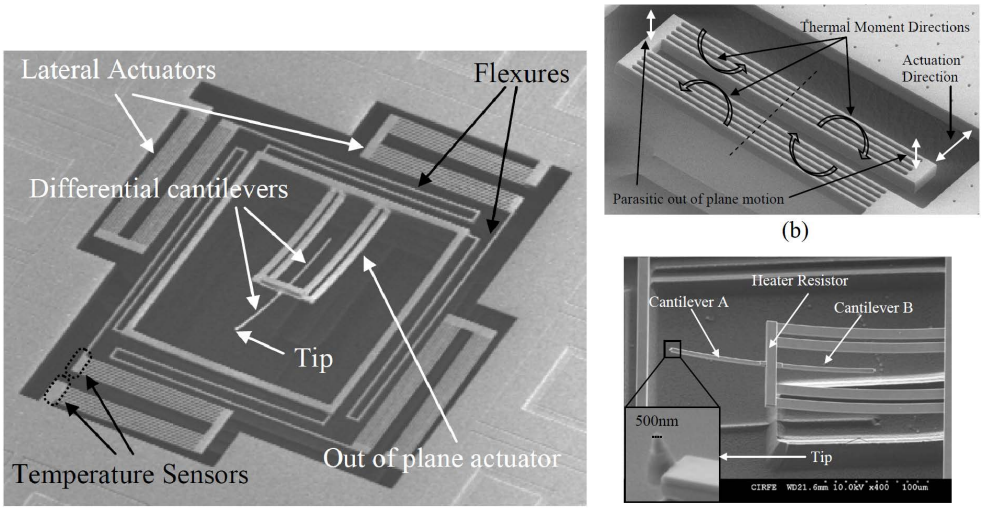

Figure 2.16: Electrothermal actuated AFM chip proposed by *Sarkar* [50] (Copyright ©2011, IEEE).

2.2 Integrated Detection Schemes

2.2.1 Electrostatic Detection

1. As mentioned in section 2.1.1, Blanc et al. used a cantilever with a counter electrode as shown in Figure 2.5. Figure 2.17b depicts an array of electrostatic probes fabricated based on this design. Blanc used cantilever's resonant frequency shift as the feedback loop signal which occurs because of the tip-sample forces. Then the output of the loop was applied to the piezoelectric stage holding the cantilever compartment to control the vertical movement as illustrated in Figure 2.17b.

The force gradients which cause the frequency shift were measured by the capacitive

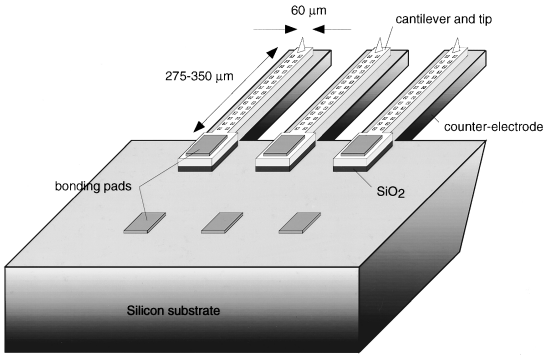

(a) Schematic drawing of the probe array

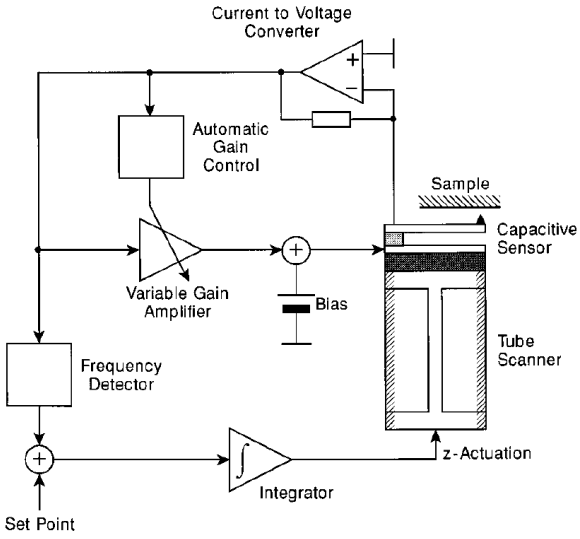

(b) Test setup

Figure 2.17: AFM system including the probe array and test setup for capacitive detection with a feedback loop controlling the height through a piezostage developed by Blanc et al. [11] (reproduced under the license number 4344251447743 dated 08/May/2018 by AIP Publishing and Copyright Clearance Center).

sensor's current after converting it to voltage. This voltage needs to be constant in order to have a one-to-one relation between the sensor's current and cantilever's displacement so the voltage was applied back to the cantilever through a gain-control circuit and a Variable Gain Amplifier (VGA). Blanc et al. successfully scanned a Cr grating with a pitch of 250nm on a quartz substrate.

2. In Müller's report, section 2.1.1, an AFM device including two tips with separate parallel plate electrostatic actuator and detector parts was employed. The measurement parameter in this effort was the current of the sensing part which was measured by a lock-in amplifier. To scan the sample, they used a closed-loop feedback mechanism controlling the gap between the tips and the sample by a vertical piezoscanner. The test setup is shown

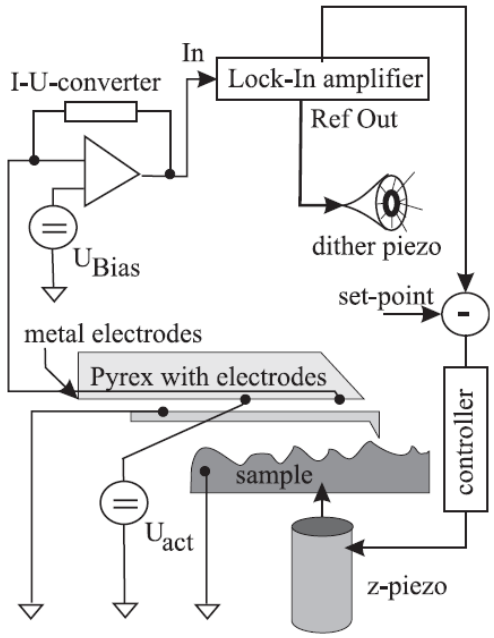

Figure 2.18: Test setup for capacitive detection with a feedback loop controlling the height through a piezostage presented by Müller et al. [35] (reproduced under written permission of the Japan Society of Applied Physics dated 09/May/2018).

in Figure 2.18. Despite of the feedback system, this setup is similar to the setup used in our research.

Bay et al. [7] proposed a balanced plate capacitor supported by two bottom electrodes acting in a differential manner. The balanced cantilever is equipped with a sharp tip fabricated by anisotropic etching at one end. Figure 2.19a shows the structure and Figure 2.19b describes the electrical circuit for providing the AC actuation voltage. A DC voltage is applied to a bottom electrode to compensate the atomic force produced by the tip-sample interaction and holding the balancing plate in its rest situation concluding in equal capacitances in balance capacitors ($\Delta C = 0$). This will eliminate the nonlinear behavior of the electrostatic actuator. The DC voltage will be used as the information outcome of

the system.

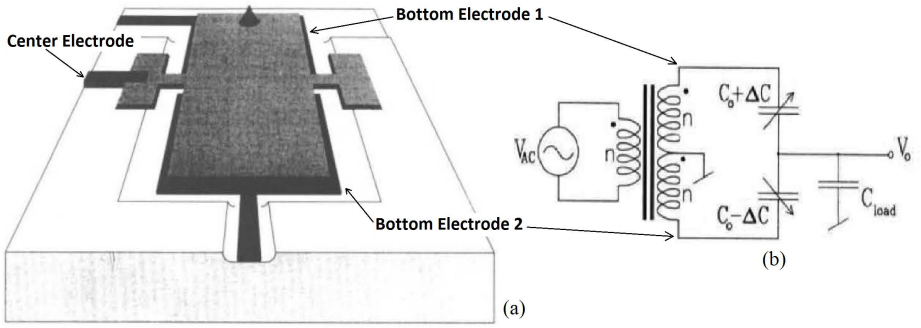

Figure 2.19: Capacitive actuation and differential detection by parallel plate capacitors; proposed by Bay et al. [7], (reproduced under the confirmation number 11716440 dated 08/May/2018 by Institute of Physics Publishing and Copyright Clearance Center).

2.2.2 Piezoresistive Detection

By definition, piezoresistivity means the change in the electrical resistance of solids due to the change in their strain in response to an applied stress [58]. Piezoresistive materials can be easily deposited on MEMS structures like AFM cantilevers and provide an integrated force sensing method. Here, two examples out of numerous cases reported in the literature will be presented.

1. Sarkar [50] has used piezoresistive strain gauges and temperature sensors in the actuators to detect the forces and perform the measurement using a circuit.

2. Thysen et al. [53] developed a SPM probe with two cantilevers. One is for imaging and the second is for reference. They used SOI wafers for fabricating this device. As Figure

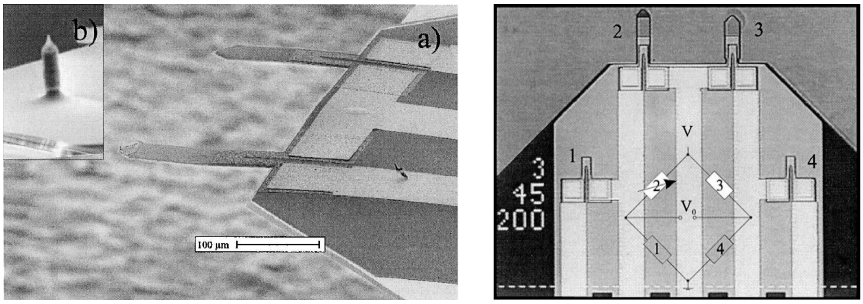

Figure 2.20: AFM probe with integrated piezoresistive read-out; Thaysen et al. [53] (reproduced under license number 4344290818159 dated 08/May/2018 from Elsevier and Copyright Clearance Center).

2.20 shows, thin film piezoresistive transducers have been encapsulated in a dielectric film to on the cantilevers to complete a symmetric Wheatstone bridge for signal read-out.

At the end, Table 2.1 summarizes the advantages and disadvantages of different actuation and detection properties including the conventional optical detection method.

2.3 Summary

In this chapter, the reported attempts of integrating the actuation mechanism to the scanning probe microscope's tip and cantilever were reviewed with an emphasize on the electrostatic actuation and capacitive detection after introducing the basic methods of actuation in microelectromechanical devices. Other methods of actuation and detection were covered which can be applied in MEMS technology including piezoelectric, piezoresistive and electrothermal properties.

In the investigated reports, there are cases which have similarities with the main streamline in this research in the fundamentals of the theory while the overall approaches are dif-

Table 2.1: Comparison of different MEMS actuation/detection methods [32]

Method	**Pros**	**Cons**
Optical	simple readout very high sensitivity mature technology No need to modify the cantilever	not array compatible, susceptible to refractive index changes, limited scanning range.
Electrostatic	Naturally compatible with MEMS No need to external fields very low power consumption applicable for actuation & detection very fast response time	Need to high voltage, Need to very close electrodes, Nonlinearity.
Piezoelectric	applicable for actuation & detection fast response time.	nonlinear vs actuation voltage, incompatible with CMOS fabrication process.
Piezoresistive	array applications	applicable for detection only.
Electrothermal	array applications, CMOS compatible. easy implementation	applicable for actuation only, relatively high time constant. interference with environment

ferent. Consequently, the approach in this research including the structure, the detection method of measuring the actuator's current at second harmonic of excitation frequency and the closed-loop feedback scheme controlling the probe's effective deflection are not analogous to others' works to the best of our knowledge.

Chapter 3

EAFM System

In this chapter, the hardware which have been designed, manufactured, and revised to realize the conceptual model of the research will be explained in three sections. First, we will describe the realization of electrostatic actuators based on commercial AFM probes in two scenarios, then we will focus on different apparatus designed and constructed for implementing the function of current measurement. At last, we will introduce the electronic circuits we have developed.

3.1 Integrated Probes

For the purpose of electrostatic actuation, a conductive microbeam and a counter electrode are needed. Usually in MEMS structures, the whole body of the structure including the device and the electrodes are in the same chip, however, in AFM probes, AFM microcantilever and tip should be free and able to oscillate and move above the specimen.

Consequently, the counter electrode can not cover the whole length of the cantilever in the same side of the specimen. Considering this condition, four different strategies depicted in Figure 3.1 were possible:

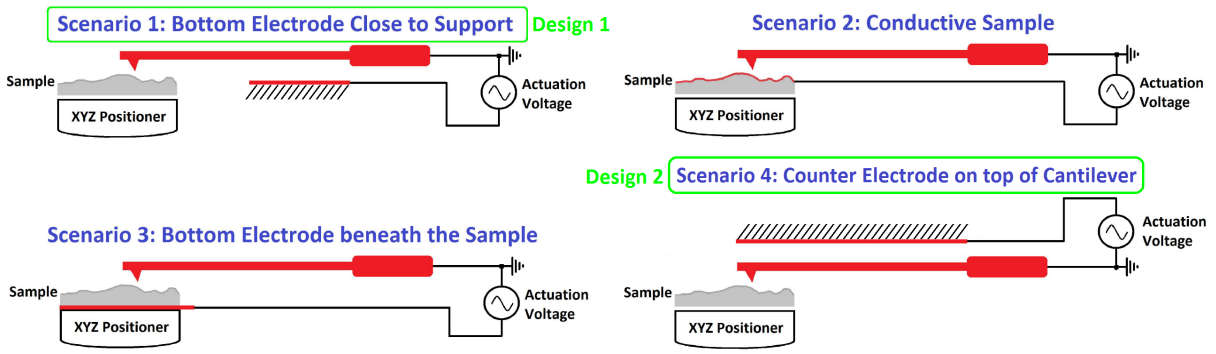

Figure 3.1: Four scenarios for applying the electrostatic force to AFM cantilever while scanning the specimen in general design.

1. The bottom electrode overlaps a portion (less than $\frac{1}{2}$) of the cantilever's length. This will let the cantilever to accomplish free oscillation over the specimen with the desired amplitude and there is no need to manipulate the sample and/or the XY&Z stage. This method supports diverse types of specimen and can work in vacuum, air or even liquid environments. The next advantage of this case is the independence of the electrostatic force from the interatomic forces of the tip and the surface which resembles the mechanical actuation of the SPM probe in commercial AFMs and facilitates a simpler analytical model.

   Moreover, by employing proper type of the cantilever and/or its coating materials and selecting suitable height, the physical interaction of the microbeam's tip and the specimen can be managed to perform more than one method of scanning probe

microscopy. For instance, the same AFM probe can accomplish the atomic force microscopy while its separation to the specimen is limited to a few nanometers; or, a single scan electrostatic force microscopy to detect surface charges by hovering above the surface with larger gap. This scenario also supports all three AFM working modes by a well-defined height control system.

The first issue in this design is the cantilever's length, namely we need cantilevers having enough length to cover the bottom electrode and at the same time, being able to have access to the sample's surface. This fact restricts our selections to probes with minimum length of $250\mu m$, provided that we can produce PCBs with very high precision cut and chamfer at the edge.

The second issue with this scenario is the high actuation voltage it needs because of the small overlapping area, and difficulty in the relatively high gap between the cantilever and bottom electrode.

2. The specimen is able to carry the actuation voltage. The advantages of this method are working with relatively low voltages and simplicity in mechanical fixture. One of the important disadvantages is the need to conductive specimen, or, a way to manipulate the sample to carry electric charges. This will affect the properties of the sample and also producing complex fringe fields. Evidently, this method is contradicting the philosophy of atomic force microscopy compared to scanning tunneling microscopy and will not meet the generality of the design. The probability of emerging tunneling current, pull-in and damaging the specimen is high in this approach.

3. A conductive plane drove by the actuation voltage covers the XY&Z stage under-

neath of the specimen. This method basically has the advantage of ability to work with relatively low voltages and scanning all types of specimen. However, its main drawback is the nonuniform electric field between the bottom electrode and the conductive cantilever which will affect all the analytical models of the vibration because the permittivity of the sensing capacitor will be a function of the sample's substance and more or less like a random variable. So the process of controlling the average height of the cantilever will be extremely complicated although not impossible.

In this case, the electrostatic force can not be independent from the interatomic forces of the tip and the surface, causing extra complexity in deriving a comprehensive analytical model. For the same reason, we will have intricate fringe fields between the tip and the sample which in many cases cause a more effective impact compared to uniform electrical field. With this scenario, the AFM cantilever is more likely to pull-in and damage the specimen.

4. A counter electrode at the top side of the cantilever will carry the excitation signal and the specimen is underneath the cantilever's tip. This scenario has the main advantage of higher current induced by the vibrating cantilever thus the detection system provides higher performance.

   The second advantage of this strategy is the low price. This design needs only a commercial AFM probe, a PCB probe carrier (will be called daughterboard) and very small amounts of conductive paste. The third technical advantage of this method is its simplicity in assembling, explained in more detail in section 3.1.2.

   An issue for this scenario is the requirement to increase the counter electrode's thick-

ness drastically; however, this issue could be addressed by the same conductive paste used to install the AFM probe on the probe carrier PCB. The thickness could be augmented gradually by some control on the amount of paste.

In this way, we would be able to manage the gap between the counter electrode and the cantilever because it has a substantial impact on the displacement and velocity of the cantilever, affecting the required levels of DC and AC components of the excitation voltage. The other disadvantage of this design is that once it is installed, there is no optical access to the probe for other measurements like displacement and/or velocity using a laser Doppler vibrometer.

Despite of the shortcomings, this design was selected and exploited for all the experiments of line scanning and raster scanning.

Relying on this discussion, eventually the first scenario was selected to design the probe holder assembly for the first part of the research and the fourth scenario for experiments regarding tapping mode and scanning.

3.1.1 EAFM Probe Prototype 1

For the first probe scenario, two different structures were designed. These structures will be declared in this section including the design details, challenges and some measurements. The analytical model and numerical simulations will be explained in chapter 4.

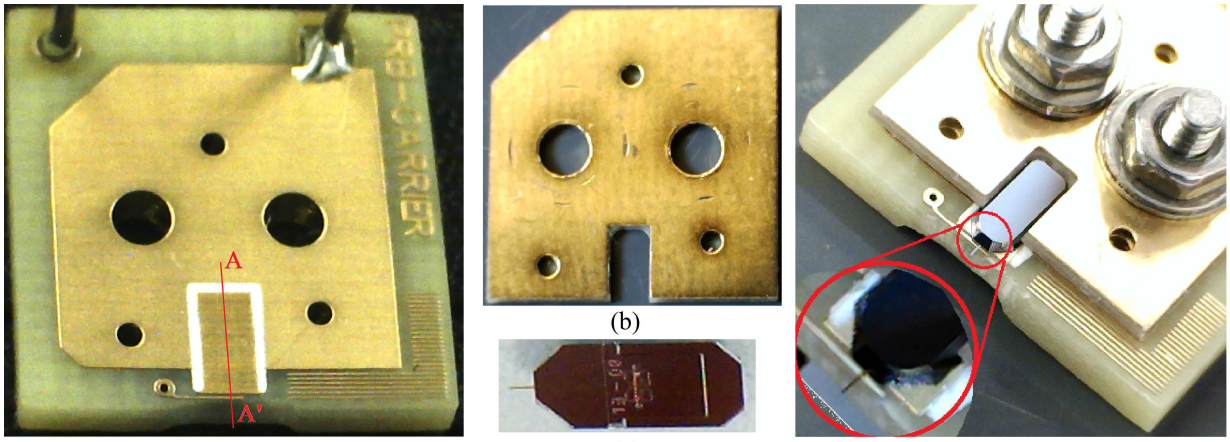

Figure 3.2: EAFM probe assembly for the first design. (a) probe carrier PCB (first version), (b) probe clamp PCB, (c) AFM silicon probe (courtesy of Bruker® Corporation) (d) the assembled AFM probe with the inset showing the configuration of the bottom electrode and the cantilever (dimensions not to scale).

.

Assembly 1

The simplest and fastest commercial technology for the structure of the probe holder was the printed circuit board (PCB) because the state-of-art manufacturing methods support capabilities as low as 3 mils ($76.4\mu m$) in track widths and separations. This facilitated PCBs containing structures in the order of the AFM probes'cantilevers. Figure 3.2 shows the components of this design.

1. **The probe carrier PCB**. As Figure 3.2a shows, this part includes the bottom electrode and an electrode to connect to the body of the AFM probe's silicon chip. Two versions for this piece of PCB were designed. In the first version, this part included an extra selective gold coating on the place of the silicon probe to guarantee

the gap between the surface of the silicon probe and the bottom electrode. But after assembling all parts and measuring the surface profile of the probe structure, we figured out that the practical gap was far above the desired value. This challenge is discussed in detail in section 3.1.1.

2. **The probe clamp PCB** which is responsible for securing the silicon probe on the probe carrier PCB (Figure 3.2b).

3. **AFM silicon probe**: Commercial silicon AFM probes in two versions: $450\mu m$ from Bruker® Corporation and $225\mu m$ from NANOSENSORS™ (Figure 3.2c).

These components are tightened together using screws and bolts. The *Prototype 1* of final assembled device is shown in Figure 3.2d.

Design Challenges

Two challenges were encountered in the design and realization of the probe carrier PCB.

1. **Silicon AFM Probes with Rectangular Cantilevers**

   The common microfabrication process for standard rectangular AFM cantilevers is wet-etching. This means the cantilever is not protruded from the body of probe chip, instead, it is like an extra layer on the surface of the silicon probe chip. This fact was not evident from the pictures in the datasheet prior to ordering the AFM probes. Figure 3.3 shows the profile of the silicon probe measured by Veeco NT1100 Optical Profilometer and the schematic of the silicon probe provided by Bruker®s catalog [15]. This profile shows the cantilever's stem is $8\mu m$ high which will not allow the

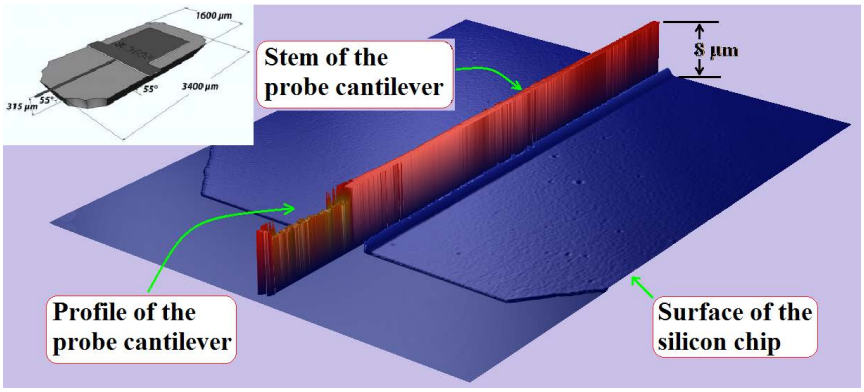

Figure 3.3: The surface profile of NANOSENSORS^{TM} 225μm AFM silicon probes. The profile shows the thickness of the cantilever's stem on the probe chip is around 8μm. The inset shows a schematic of the silicon probe adopted from Bruker's catalog [15].

surface of the silicon probe's chip to sit on the probe carrier PCB's surface. The effect is shown in Figure 3.4b. This will add a significant gap between the bottom electrode (on the probe carrier PCB) and the AFM cantilever.

2. **Probe Carrier PCB**

The first version of the probe carrier PCB was designed based on the fact that the thickness of the copper layer on the PCB's substrate (known as FR4) is uniform and we could add extra selective gold coating with a known thickness on any desired position. Hence, this board was ordered based on the assumption shown in Figure 3.4a. The diagrams in this figure represent the A-A'section shown in red color in Figure 3.2a.

Indeed, the thickness of the extra gold coating should be around 50 microinches (or 1.27μm) as per PCB manufacturer specifications. Moreover, the thickness of the bottom electrode was expected to be equal to the thickness of the copper areas on

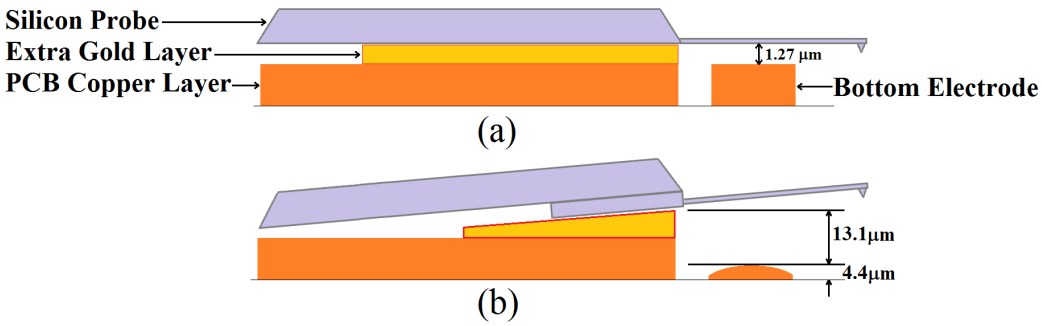

Figure 3.4: Declaration of the problem in probe carrier board PCB: (a) primary design assumption, (b) the first version

the board. With these assumptions and considering a flat AFM silicon probe sitting evenly on the surface of the extra gold coating, a gap around 1.5 to 3μm between the bottom electrode and the cantilever was awaited, promising an effective electrostatic field with reasonable actuation voltages. However, as the AFM probe was completely assembled using this board and a 225μm AFM probe, the practical gap was measured more than 60μm based on the information of the optical profilometer shown in Figure 3.5b.

Figure 3.5a shows the inclination in the thickness of the extra gold coating. This means the gold area is thicker in the edge. This phenomenon is reasonable because the extra gold coating has been implemented by electroplating which makes slightly higher thickness in the edges compared to the middle of the coating area.

Furthermore, the thickness of the bottom electrode is less than other copper parts because in the production of PCB, the copper in unwanted area is etched with acid which causes the edges of copper tracks and areas etched more. Consequently, narrow

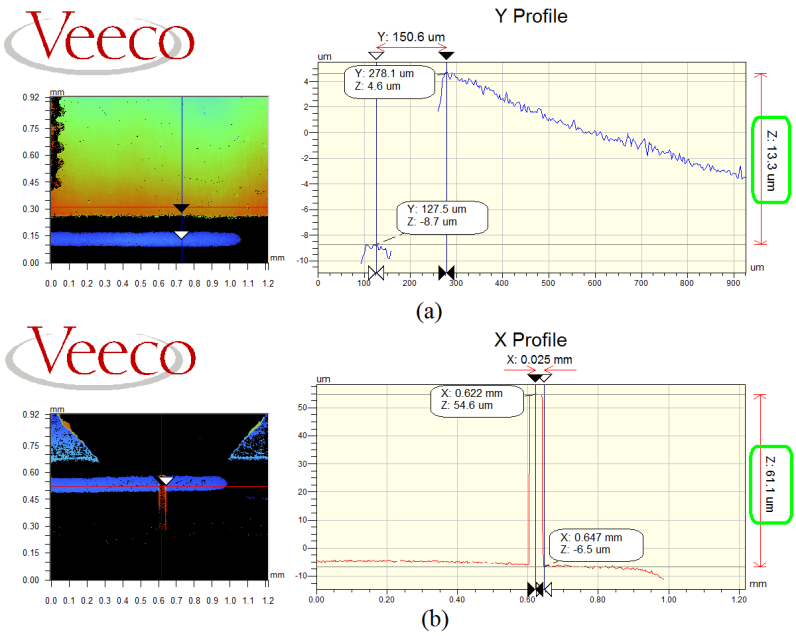

Figure 3.5: The profile of (a) the first version of probe carrier PCB near the bottom electrode, the practical gap is 13.3 instead of 1.27 μm, (b) the gap between the 225μm AFM probe and bottom electrode is 61.1μm.

tracks will get thinner than wider areas. This causes a huge gap, namely 13μm between the surface of the extra gold layer and the bottom electrode as evident in Figure 3.5a while they were supposed to be 1.27μm different.

The integration of these problems is shown schematically in Figure 3.4b and the profile of real device along with the measurement in Figure 3.5b.

To address this problem, different mechanical and chemical ways were tested to mitigate the thickness of the gold layer or the whole copper layer on the PCB. Finally, a probe with 14.1μm separation was achieved. This method was not systematic and there was no control on the process while it was too time consuming. For this reason,

the second version of the probe carrier PCB was initiated.

Assembly 2

To comply with other researches, and to be able to use other equipment in the CIRFE-Lab, Assembly 1 needed to be upgraded to new design including a trans-impedance amplifier very close to the AFM device. The outcome of this requirement is illustrated in Figure 3.6. This board named as daughterboard, is the probe carrier board and other parts are similar to Assembly 1.

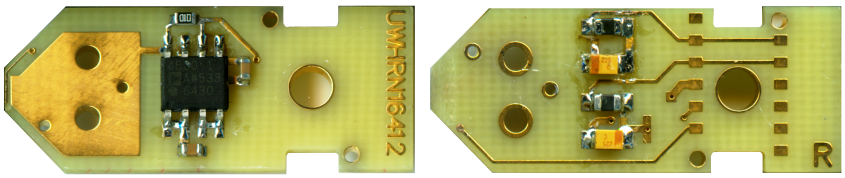

Figure 3.6: Second design for the first scenario, showing EAFM probe carrier PCB's top layer (left) and bottom layer (right), including the trans-impedance amplifier

3.1.2 EAFM Probe Prototype 2

The second design illustrated in Fig. 3.7 used scenario 4 in Figure 3.1. In this design, the bolts and nuts were eliminated while a conductive paste was used to stick the AFM probe to the PCB. Compared to the previous design, this process is easier, faster and less likely to break the cantilever. As depicted in Fig 3.7a, thickness of the fixed electrode can be managed to be in the order of the probe's chip thickness plus the copper layer resulting in a gap as wide as $15\mu m$ (Fig. 3.7c). The overlapping area is also increased by 2 orders of

magnitude resulting in $C_\circ \approx 10000aF$. This structure produced promising results and was used for line and raster scanning.

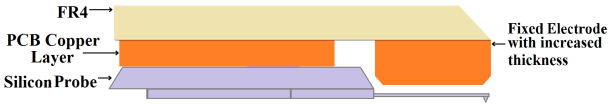

(a) Outline of second design

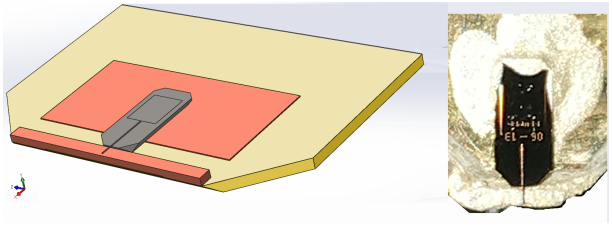

(b) Schematic and a picture of assembled device (flipped over)

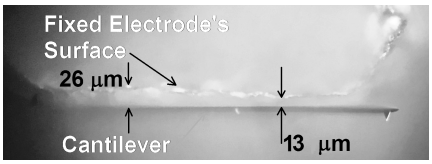

(c) Microscopic picture showing the cross section of the cantilever and fixed electrode

Figure 3.7: Details of second design

3.2 Fixtures

A scanning probe microscope needs a stable fixture to minimize external disturbances (mechanical noise). This fact forced us to design and manufacture the fixture with steel and aluminum. The fixture had to satisfy these fundamental functionalities:

- providing a platform to hold the sample,

Figure 3.8: The basic part of all fixtures including the coarse and fine Z-stage.

- ability to manage the relative separation of the sample and AFM probe's tip,
- accommodating the mechanism of raster scanning,
- reducing the ambient mechanical noise.

To meet these requirements, we considered to hold the sample on a platform with very accurate manually controlled vertical movement, and a 0-D, 1-D or 2-D positioner close to the vertical stage holding the AFM probe assembly. This assembly included the motherboard and daughterboard.

For this purpose, a very accurate manual linear stage with the accuracy of $22\frac{nm}{seg}$ was designed and constructed which does not have a commercial equivalent to the best of our knowledge. This linear positioner, called the *fine knob*, was attached to a commercial linear stage with the accuracy of $10\frac{\mu m}{seg}$, called *coarse knob*. These two manual micrometers

together configured the vertical stage facility in the fixture, common in all four apparatus as shown in Figure 3.8.

To address the issue of ambient mechanical noise and minimizing it, standard vibration isolators were exploited. Based on the type of scanning and the horizontal stages possessed temporarily, the constructed fixture needed to be reconfigured. These different designs will be discussed below:

3.2.1 First Apparatus

In this part, the main goal was to investigate the behavior of the EAFM current in tapping mode without scrolling over the sample. In fact, this step was crucial for the surface scanning because there was a strict need to an estimation of the optimum tip-sample distance. This option was performed by one-point scanning of the sample and recording the current frequency response for different tip-sample distances. Thus providing with comprehensive information about the current's magnitude and phase in frequency bands close to the second harmonic of cantilever's first resonant frequency, which was indispensable for deriving the calibration curve. The calibration curve was used to find the optimum distance for the highest differentiability in the most linear fashion. Figure 3.9 illustrates the picture of the apparatus used for this step.

This fixture was used to investigate other properties of the actuator's current versus change in DC and AC components of excitation voltage, nonlinear behaviors. Results of these tests will be discussed in chapter 5.

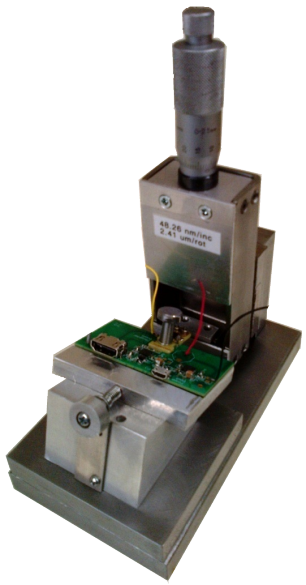

Figure 3.9: The fixture used for tapping mode tests. including the coarse and fine Z-stage.

3.2.2 Second Apparatus

The first experiment to investigate the feasibility of the constructed system was repeated scanning of one line of a specimen. Using the 1-D positioner, several line scanning measurements were implemented after the hight of the probe was set to an appropriate value, enabling tapping. The fixture for these experiments is shown in Figure 3.10. In each scan, the same line was scanned in different lengths and the measured current was recorded.

1-D Piezoscanner

After deriving the optimum distance, line scanning was started to investigate the feasibility of the approach and the performance of the manufactured hardware. A 1-D piezoscannar from nPoint Inc. was employed which supported very good resolution and linearity while

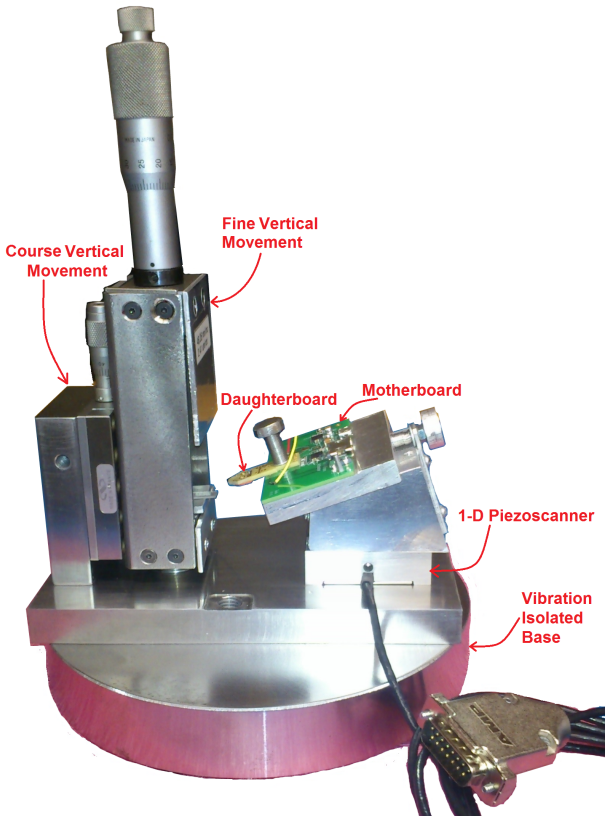

Figure 3.10: EAFM fixture with nPoint's 1-D scanner, implemented for line scanning.

scanning. The moving range of this stage was $150\mu m$ and the resolution was 1 nm. a friendly graphical user interface facilitated the settings and control of the stage. Figure 3.11b shows the scanner installed in the fixture, the controller and the graphical user interface.

3.2.3 Third Apparatus

The high precision piezoscanner described in section 3.2.2 provided only the X-direction scanning while for Y-direction we had to confine ourselves to a manual XY-stage with the accuracy of $10\mu m/segment$. Fig. 3.11a shows this fixture. For raster scanning, we scanned

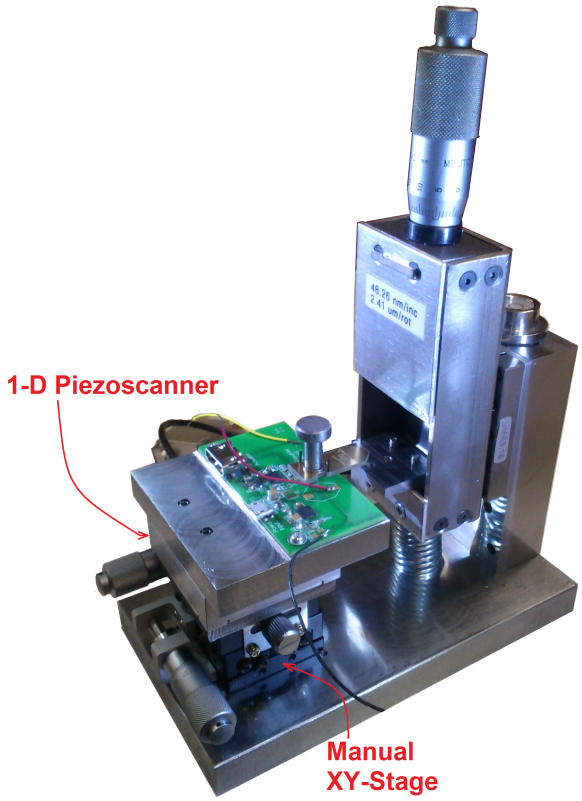

(a) EAFM fixture with the nPoint's 1-D scanner installed on a manual XY-scanner, implemented for raster scanning.

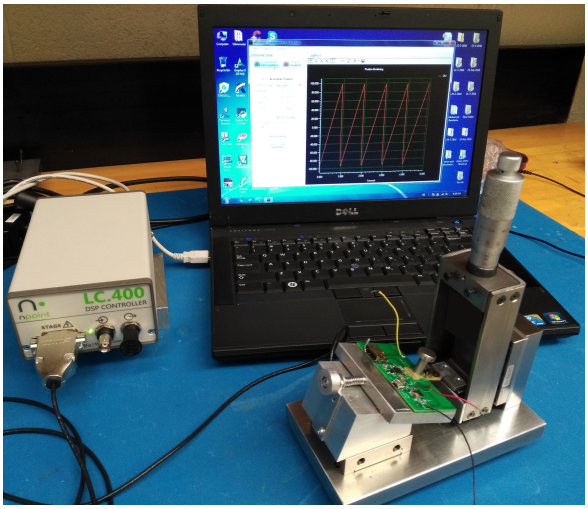

(b) nPoint's 1-D scanner intalled in the fixture, the control device and the GUI.

Figure 3.11: Third apparatus

one line of the sample, thereafter, we progressed the tip toward the next line manually with an accuracy worse than $5\mu m$ and started scanning the next line. Evidently, this distance

was far below the requirements of AFM images, but at this step, the proof of concept of integrated electrostatic actuation/detection in the implemented structure was the main goal only.

3.2.4 Fourth Apparatus

The fourth fixture illustrated in Figure 3.12, was configured for open-loop and closed-loop raster scanning based on a motorized XY-stage from National Apertures Inc.®.

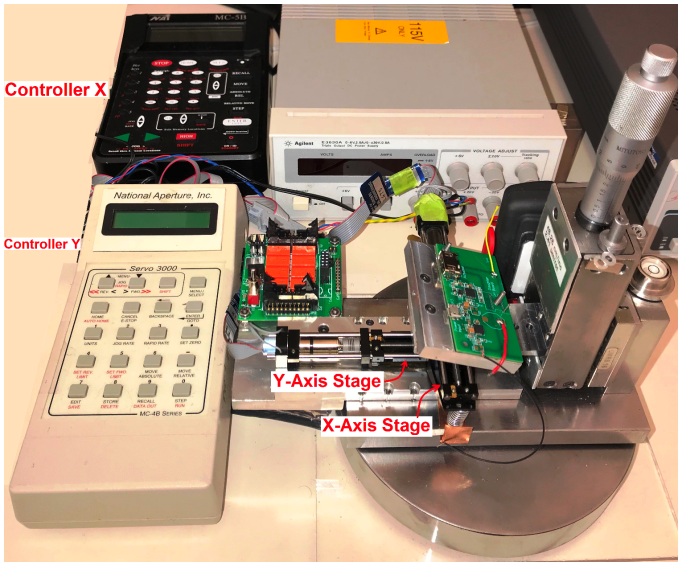

Figure 3.12: Fourth apparatus

Each direction on this stage had a DC motor with a 64:1 gearbox to reduce the speed and an encoder and controller. The claimed accuracy of movement for the linear stages was $125nm$ which was enough for scanning requirements.

3.3 Circuits

During this project different circuits were designed and used. The most important ones will be described in this section.

3.3.1 Resonant Drive Circuit

The function of this circuit is explained in section 2.1.1. Here the block diagram, schematic diagram, and PCB layouts and some pictures of the populated board will be presented.

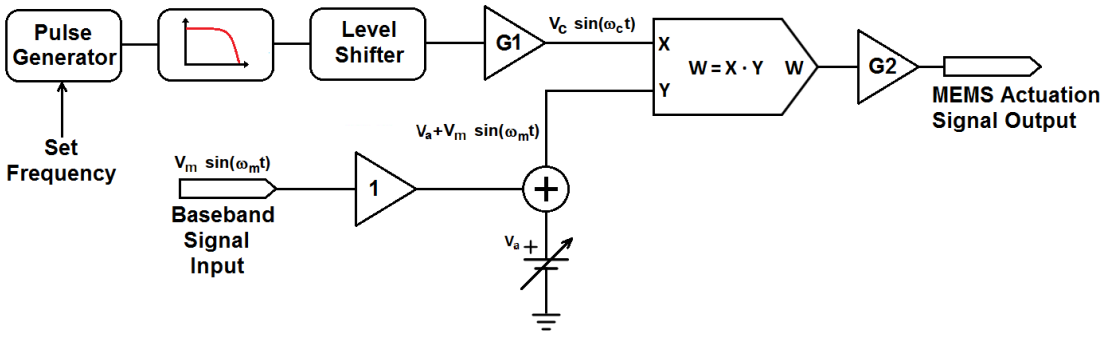

Figure 3.13: Resonant drive circuit's block diagram.

The resonant drive circuit includes several building blocks as depicted in Figure 3.13, with the most important ones explained in the following:

- **Internal Oscillator**. This part produced the carrier frequency (ω_c) employing a Voltage controlled oscillator (VCO) with a square wave output. The oscillator frequency was designed around $1MHz$ while it can be tuned by a variable DC voltage.

- **Low-pass Filter**. The carrier frequency deployed to the multiplier needs to be a pure sinusoid without higher harmonics of ω_c. Therefore, a low-pass filter with the specifications listed in Table 3.1 was designed.

  Table 3.1: Design specifications for the low pass filter in resonant drive circuit.

Specifications	**Description**
Filter Type	Low-Pass, Chebyshev
Filter Order	6
Specification	Optimize for Noise
Passband	-3dB at 1MHz
Stopband	-40dB at 2MHz
Passband Ripple	2%

  The output of this filter was a sinusoidal signal, consequently, it was not sensitive to the pass-band ripple. This fact enabled the benefit of lower order configuration of Chebyshev filters while keeping high stop-band attenuation ratio and minimum error between the actual and the idealized filter characteristics. Figure 3.14 depicts the most important characteristics for the filter of Table 3.1

- **Analog Multiplier** This multiplier was designed using the AD835 chip from Analog Devices™ with the features listed in Table 3.2.

AD835 is an optimized device to guarantee low noise operation of the circuit and a precise function regardless of the inputs polarities.

The schematic diagram, top and bottom layer PCB layouts and pictures are shown in Figures 3.15 and 3.16 respectively.

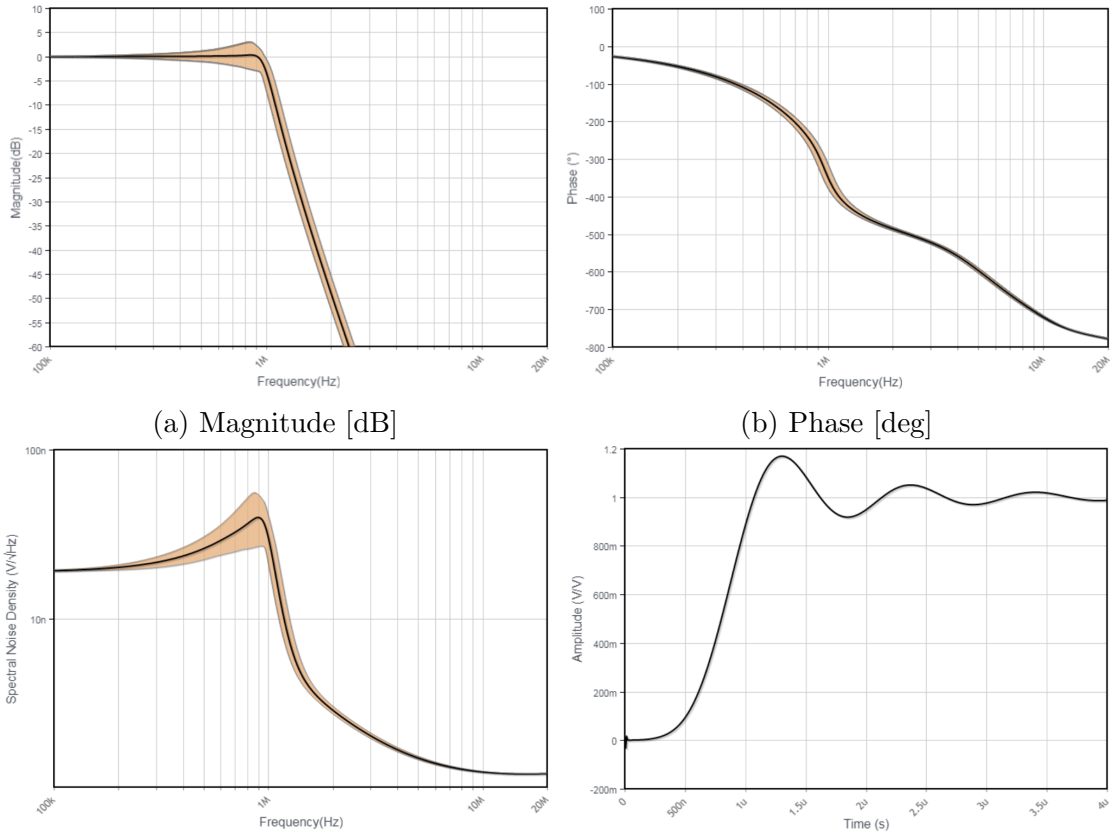

(a) Magnitude [dB]

(b) Phase [deg]

(c) Noise Density $[V/\sqrt{Hz}]$

(d) Step Response

Figure 3.14: Characteristics of the low-pass filter of resonant drive circuit. The brown margins show the drift in characteristics because of components' tolerances.

3.3.2 Motherboard Circuit

This circuit provides the power supply for daughter board. Low noise and low drop out linear regulators were used to convert the $\pm 9V$ input to clean $\pm 5V$ to drive the electrometer on the daughterboard. Figure 3.17 shows the schematic diagram. The PCB was designed to be compatible to the AFM system existent in CIRFE Lab. Figure 3.18 illustrates the PCB layout and pictures of the populated board.

Table 3.2: Technical features of AD835 analog multiplier chip.

Feature	**Description**
Multiplier Type	Four quadrant
Output Signal	Voltage
-3 dB Bandwidth	up to 250 MHz
Settling Time	20 ns (to settle to 0.1% of full scale (FS))
Input Impedance	$100k\Omega \| 2pF$
Multiplier Noise	$50nV/\sqrt{Hz}$

3.3.3 Daughterboard Circuit

Daughter board circuit accommodates the AFM probe and the low noise trans-impedance amplifier. The active element in this circuit is an electrometer with very high input impedance and very low input bias current, qualified for measuring very low currents like capacitive or chemical sensors. This circuit has some considerations regarding the PCB design which were applied to some extent.

Table 3.3: Main technical features of ADA4530-1 electrometer.

Feature	**Description**
Low input bias current	$\pm 20fA$ @ 25°C
Low offset voltage	$50\mu V$/°C maximum
Low voltage noise density	$14nV/\sqrt{Hz}$
Wide bandwidth	$2MHz$ unity-gain crossover

Figure 3.19 shows the schematic diagram and Figure 3.20 depicts the PCB design. The pictures of populated board have been shown in Figure 3.6.

3.4 Summary

The hardware designed and constructed for this research were described in this chapter. First, the devices which contributed the main objective of this research, namely integration of electrostatic actuation/capacitive detection were explained. Different scenarios for these devices were thought and finally two prototypes were implemented. To complete a test fixture for scanning the surface of a sample, we needed to design and produce different fixtures based on the scanning stages available to us. In fact, the AFM system needs a sturdy structure to accommodate an XY-scanner, an appropriate assembly to hold the circuits and the EAFM probe, a vertical stage to hold the sample. This fixture was isolated from the unwanted ambient vibrations by standard Sorbothane® vibration isolators.

The vertical stage with fine and coarse adjustments had the ability the control the tip-sample distance in sub-micrometer accuracy.

Finally several circuits were designed and developed to facilitate the resonant drive phenomenon and biasing requirements for the transimpedance amplifier on the EAFM Prototype 2.

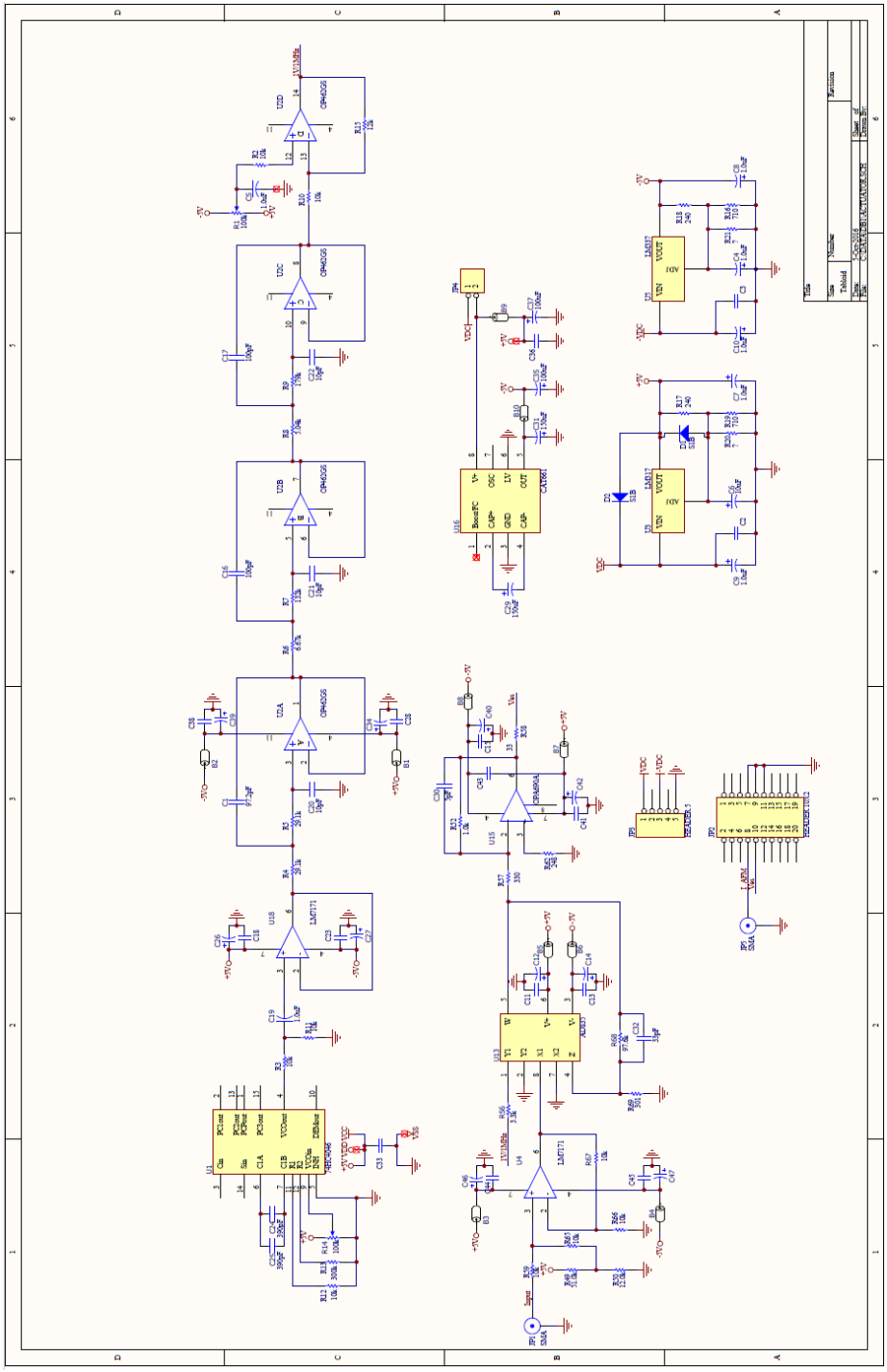

Figure 3.15: Resonant drive circuit's schematic diagram.

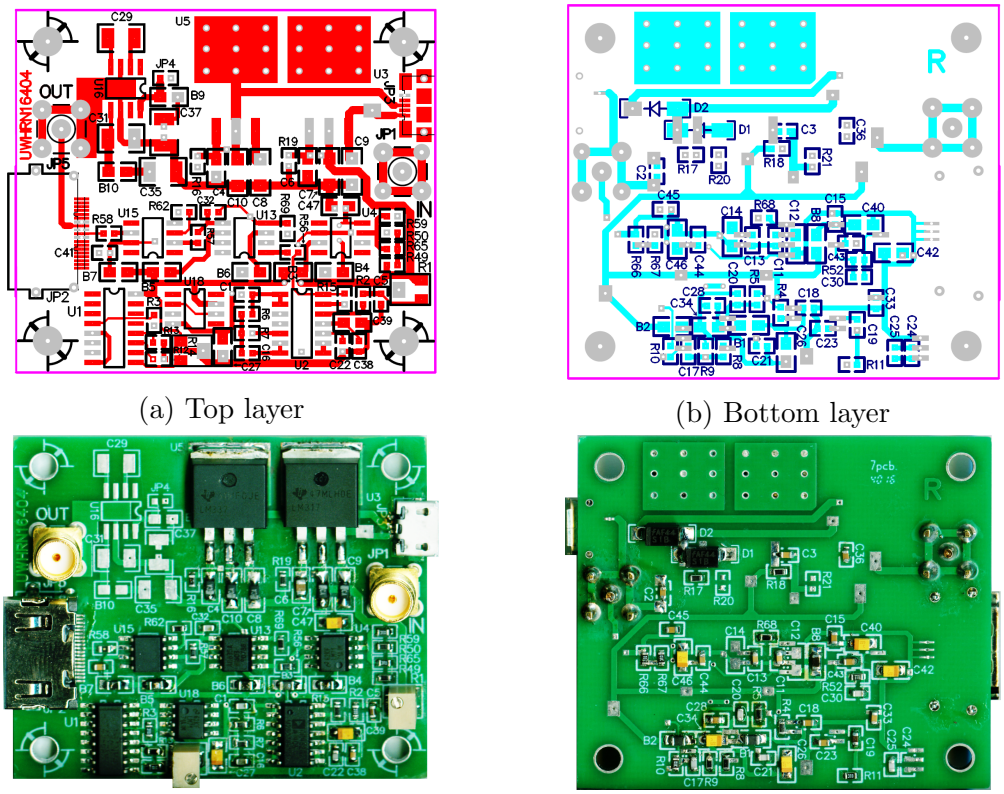

(a) Top layer

(b) Bottom layer

(c) Top layer

(d) Bottom layer

Figure 3.16: Resonant drive board's PCB layout and pictures.

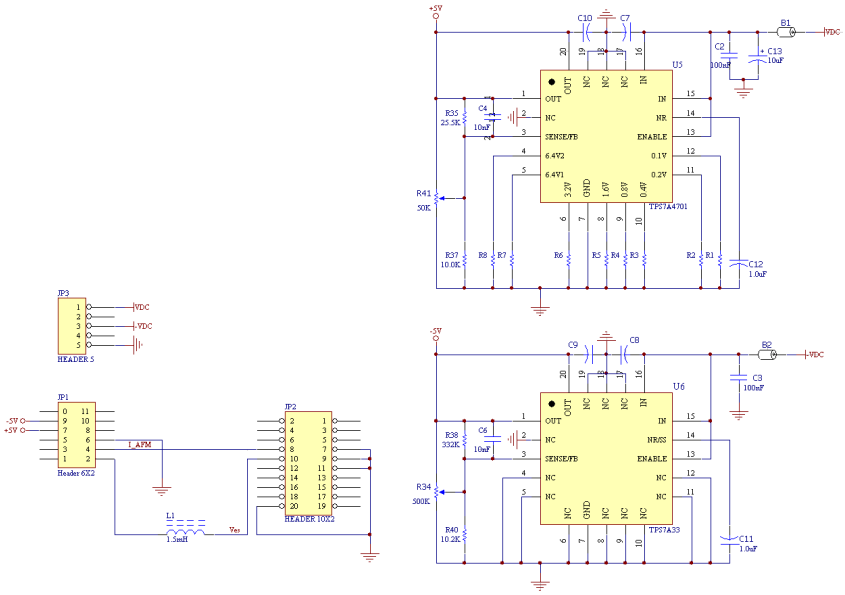

Figure 3.17: Schematic diagram of the motherboard.

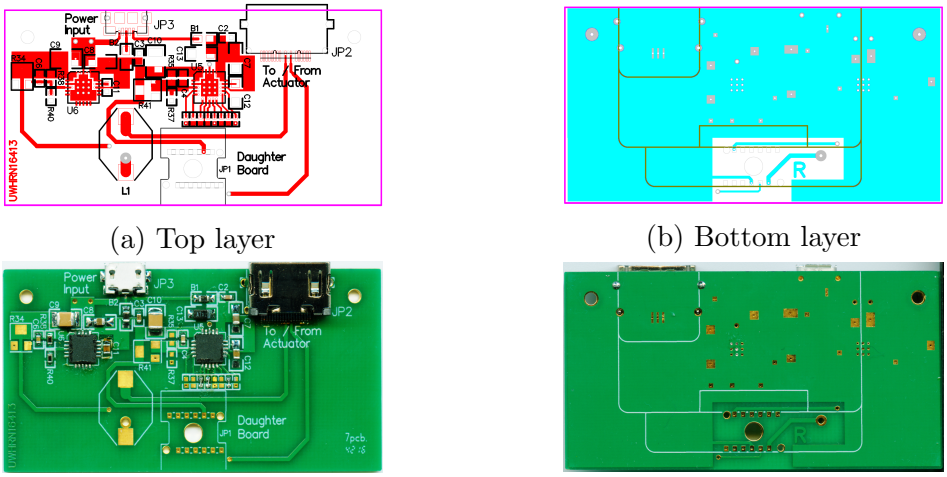

(a) Top layer

(b) Bottom layer

(c) Top layer

(d) Bottom layer

Figure 3.18: Motherboard's PCB layouts and pictures

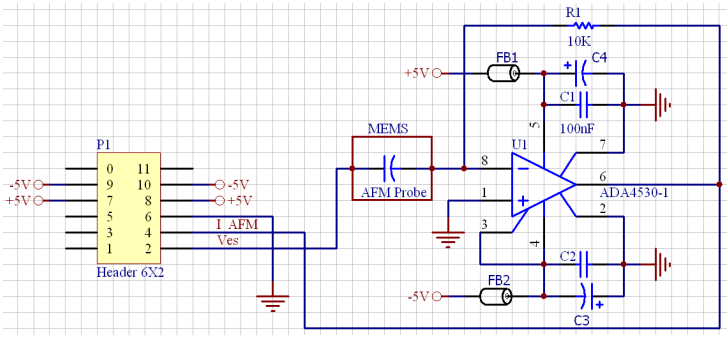

Figure 3.19: Schematic diagram for daughterboard including the AFM probe and transimpedance amplifier.

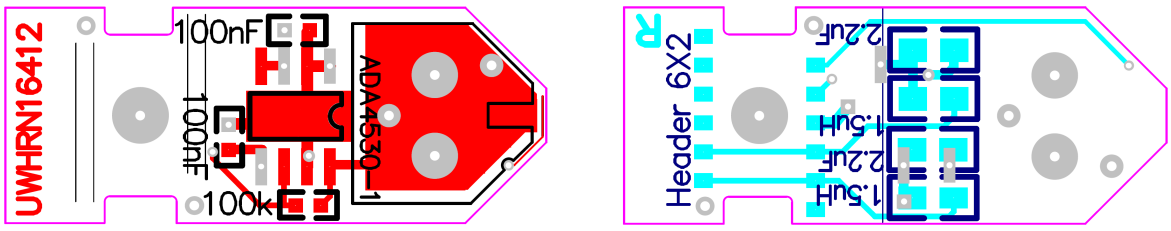

(a) Top layer

(b) Bottom layer

Figure 3.20: Daughterboard's PCB layouts.

Chapter 4

Analytical and Numerical Results

4.1 Theory of Operation

Understanding the components of current in an electrostatic MEMS actuator is of trivial importance for motion detection in cases we want to prevent using an optical motion detection scheme. Many applications need this knowledge of current because it is not possible to utilize a Doppler laser motion detection system in all cases. For example, many devices are already packaged and there is no access to the moving parts, some devices have an in-plane motion which is hardly detectable by the optical system. In most cases the optical vibration analysis system is usually too bulky and expensive.

On the other hand, the fundamental necessary equipment for current measurement are a trans-impedance amplifier for bringing up the level of actuator's current and a lock-in amplifier for detecting the current at higher harmonics of the actuation frequency. These

systems can be implemented for the proprietary application by standard digital signal processing modules.

In this study, the electrostatic actuator is formed by a fixed-free cantilever and a fixed electrode with the same length as the cantilever. The fringing electric field is not considered for simplicity.

4.1.1 Electrostatic Actuation

The electrostatic force in a parallel plate electrostatic actuator will be reviewed to investigate the effect of actuation voltage components.

Electrostatic Force

The electrostatic force produced by the applied voltage $V_a(t) = V_{DC} + V_{AC}\sin(\Omega t)$ is:

$$\begin{aligned} E_{\text{es}}(t) &= \frac{1}{2} C V_a(t)^2, \\ F_{\text{es}}(t) = -\frac{\partial E_{\text{es}}}{\partial x} &= -\frac{1}{2}\frac{\partial C}{\partial x} V_a(t)^2, \\ &= -\frac{1}{2}\frac{\partial C}{\partial x}\left(V_{DC}^2 + 2V_{DC}V_{AC}\sin(\Omega t) + V_{AC}^2\sin^2(\Omega t)\right), \\ &= -\frac{1}{2}\frac{\partial C}{\partial x}\left(V_{DC}^2 + \frac{V_{AC}^2}{2} + 2V_{DC}V_{AC}\sin(\Omega t) - \frac{V_{AC}^2}{2}\cos(2\Omega t)\right) \end{aligned} \tag{4.1}$$

The terms including V_{DC} have a dominant effect in the final value of F_{es} compared to the second harmonic component as illustrated in Figure 4.1. Concluding, if we want to apply only the AC component ($V_{\text{DC}} = 0$), we have to set the actuation frequency to half of the

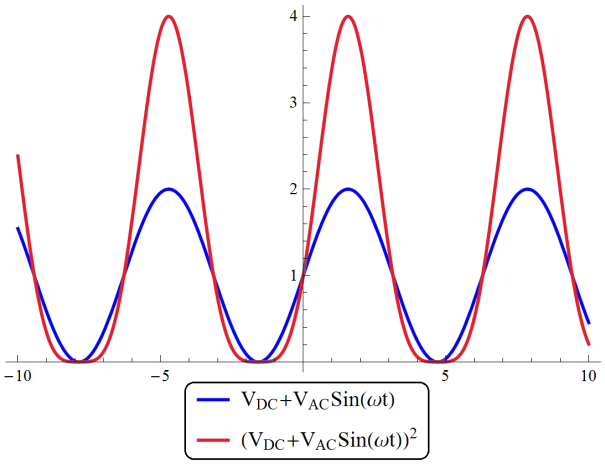

Figure 4.1: Comparison of two functions for $\Omega = 1, V_{\mathrm{DC}} = 1, V_{\mathrm{AC}} = 1$

device mechanical resonant frequency. As thus:

$$V_{\mathrm{DC}} = 0 \quad \Rightarrow \quad \Omega_a = \frac{1}{2}\Omega_\circ \tag{4.2}$$

$$E_{\mathrm{es}}(t) = -\frac{1}{2}\frac{\partial C}{\partial x}\frac{V_{AC}^2}{2}(1 - \cos(\Omega_\circ t)) \tag{4.3}$$

As an experimental example, Fig. 4.2 shows the displacement response of an AFM cantilever to the pure AC excitation with half the resonant frequency captured by the laser Doppler vibrometer. The displacement response at resonance frequency is 80 times bigger than the excitation frequency because of the mechanical resonant effect.

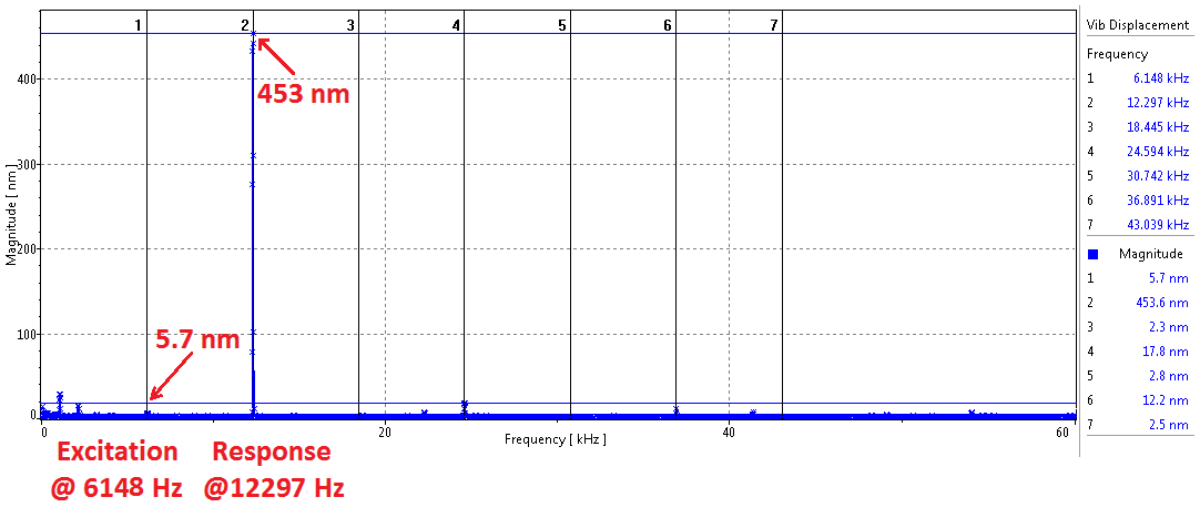

Figure 4.2: $V_{\mathrm{DC}} = 0, V_{\mathrm{AC}} = 10V_{peak}$ and $f_0 = 12296Hz$, the actuation frequency is $6148Hz$ and the displacement at resonant frequency is 80 times bigger than actuation frequency

4.1.2 Analysis of Motion Induced Current

The current in a capacitor is the time derivative of its charge. For an electrostatic actuator with a voltage-dependent capacitance, current can be written as:

$$\begin{aligned} i(t) &= \dot{q} = \frac{dq}{dt}, \\ i(t) &= \frac{d(C \cdot V)}{dt}, \\ i(t) &= V(t)\frac{dC(t)}{dt} + C(t)\frac{dV(t)}{dt}. \end{aligned} \tag{4.4}$$

where $C(t)$ is the whole capacitance of the electrostatic actuator and $V(t)$ is the actuation voltage.

Capacitance of the Electrostatic Actuator

The capacitance of electrostatic actuator can be considered as two parallel components:

$$C(t) = C_p + C_a(t), \tag{4.5}$$

where C_p is the parasitic capacitance due to all PCB traces, wire bondings and unavoidable proximities of conductive parts in the MEMS device and has a constant value.
$C_a(t)$ is the pure capacitance of the electrostatic actuator and is calculated by (4.6).

$$C_a(t) = \frac{\epsilon A}{g_\circ - \hat{x}(t)}, \tag{4.6}$$

where ϵ is the permittivity of the isolator in actuator (mainly air or vacuum), A is the coinciding area of electrodes, $g_\circ$ is the gap between the electrodes at rest and $\hat{x}(t)$ is the instantaneous displacement of the cantilever toward the fixed electrode. For simplicity in the future equations, we will use the non-dimensional instantaneous displacement

$$x(t) = \frac{\hat{x}(t)}{g_\circ}$$

in the form of:

$$\begin{aligned} C_a(t) &= \frac{\epsilon A}{g_\circ} \frac{1}{1 - x(t)} \\ &= C_\circ \frac{1}{1 - x(t)}, \end{aligned} \tag{4.7}$$

where $C_\circ$ is the actuator's capacitance at rest. Hence, we have:

$$\begin{aligned}\frac{dC(t)}{dt} &= \frac{d}{dt}(C_p + C_a(t)) \\ &= C_\circ \frac{\dot{x}(t)}{(1-x(t))^2}.\end{aligned} \tag{4.8}$$

Motion Induced Current

The actuation voltage consists of a DC component (V_{DC}) and an AC component (V_{AC}) at a frequency equal or close to the cantilever's mechanical resonant frequency $\Omega_\circ$. For a pure AC actuating signal (V_{DC}=0), one has to use $\Omega = \Omega_\circ/2$ because of the quadratic relation of electrostatic force and actuation voltage as described in section 4.1.1. The intention now is to find a closed form relation between the actuator's displacement and it's current; to retain the generality, the general sign Ω for the actuation frequency will be used.

$$\begin{aligned}V(t) &= V_{DC} + V_{AC}\sin(\Omega t), \\ \frac{dV(t)}{dt} &= \Omega V_{AC}\cos(\Omega t).\end{aligned}$$

Substituting all relevant equations in (4.4), we have:

$$\begin{aligned}i(t) &= (V_{DC} + V_{AC}\sin(\Omega t))C_\circ \frac{\dot{x}(t)}{(1-x(t))^2} + \left(C_p + C_\circ \frac{1}{1-x(t)}\right)(\Omega V_{AC}\cos(\Omega t)) \\ i(t) &= V_{AC}C_p\Omega\cos(\Omega t) + i_a(t)\end{aligned} \tag{4.9}$$

The first term in Equation (4.9) is the feed-through current passing through the parasitic capacitance C_p and is not relevant to the probe displacement so it will not be considered. It can be used for measurement of C_p. The remaining terms rewritten in Equation (4.10) are called *motion induced current* [43] and are of our primary interest:

$$i_a(t) = V_{DC}C_\circ\frac{\dot{x}(t)}{(1-x(t))^2} + V_{AC}C_\circ\frac{\dot{x}(t)}{(1-x(t))^2}\sin(\Omega t) + V_{AC}C_\circ\Omega\frac{1}{1-x(t)}\cos(\Omega t) \quad (4.10)$$

A closed form expression for $i_a(t)$ based on the cantilever's displacement and the electrostatic force $F_{es}(t)$ as per Equation 4.1 will be derived.

EAFM prototype 2 includes a fixed-free cantilever and a counter electrode overlapping the whole length of the cantilever. This structure allows us to use the lumped-mass approach to derive the displacement of the cantilever's free end. The equation of motion for the actuator can be written as

$$m_{eff}\ddot{x} + c\dot{x} + kx = F_{es}(t), \quad (4.11)$$

where m_{eff} is the effective mass (e.g. $m_{eff} = 0.24m$ for a fixed-free cantilever of mass m [45]), c is the damping coefficient, k is the actuator's stiffness at rest and $\Omega_\circ = \sqrt{\frac{k}{m_{eff}}}$ is the actuator's first mechanical resonant frequency.

There are two points to consider about $x(t)$ helping to simplify Equation (4.10):

1. Solving the equation of motion 4.11 for the electrostatic actuator excited by actuation voltage $V_a(t)$ with reasonable values for V_{DC} and V_{AC} and a frequency equal or close

to $\Omega_\circ$ will end up in a stable harmonic displacement with the general equation of [17]

$$x(t) = X_0 + X_1 \sin(\Omega t + \phi_1) + X_2 \sin(2\Omega t + \phi_2) + \cdots \tag{4.12}$$

All the harmonics higher than 2 can be ignored because of their trivial amplitudes compared to X_1 and just the static deflection X_0 and the amplitude of main actuation frequency Ω or X_1 will be maintained. Thus, $x(t) = X_0 + X_1 \sin(\Omega t + \phi_1)$. Hence, $\dot{x}(t) = X_1 \Omega \cos(\Omega t + \phi_1)$, where X_0, X_1 and ϕ_1 can be represented by [12, 43, 17]:

$$X_0 = \frac{\epsilon_\circ k A_{eff}}{2g_\circ^2} V_{DC}^2, \quad X_1 = \frac{\epsilon_\circ A_{eff}}{k g_\circ^2} V_{DC} V_{AC} \beta \tag{4.13}$$

while A_{eff} is actuator's effective area (e.g. $A_{eff} = \frac{3}{8}A$ for a fixed-free cantilever with area A [48]), β is a magnification factor related to the damping for excitation frequencies other than natural frequency, $\Omega_\circ$

$$\begin{aligned} \beta &= \frac{1}{\sqrt{\left(1 - \frac{\Omega^2}{\Omega_\circ^2}\right)^2 + \left(\frac{\Omega}{Q\Omega_\circ}\right)^2}} \\ \phi_1 &= \arctan\left(\frac{\frac{\Omega}{Q\Omega_\circ}}{1 - \frac{\Omega^2}{\Omega_\circ^2}}\right) \\ Q &= \frac{m_{eff}\Omega_\circ}{c} \end{aligned} \tag{4.14}$$

2. Using the Taylor series, $\frac{1}{1-x(t)}$ and $\frac{1}{(1-x(t))^2}$ can be expanded around the static deflection distance, X_0. According to the small values of higher order components, all

orders higher than 2 can safely be neglected. Consequently:

$$\begin{aligned}\frac{1}{1-x}_{|_{x=X_0}} &\cong a_0 + a_0^2(x-X_0) + a_0^3(x-X_0)^2,\\ \frac{1}{(1-x)^2}_{|_{x=X_0}} &\cong a_0^2 + 2a_0^3(x-X_0) + 3a_0^4(x-X_0)^2\end{aligned} \tag{4.15}$$

where $a_0 = 1/(1-X_0)$.

Applying point 1 in 2, Eq. (4.15) can be rewritten with the higher harmonics as:

$$\begin{aligned}\frac{1}{1-x}_{|_{x=X_0}} &\approx (a_0 + \frac{a_1^2}{2}) + a_1\sin(\Omega t+\phi_1) - \frac{a_1^2}{2}\cos(2\Omega t+2\phi_1),\\ \frac{1}{(1-x)^2}_{|_{x=X_0}} &\approx (a_0 + \frac{3a_1^2}{2}) + 2a_0a_1\sin(\Omega t+\phi_1) - \frac{3a_1^2}{2}\cos(2\Omega t+2\phi_1),\\ \frac{\dot{x}}{(1-x)^2}_{|_{x=X_0}} &\approx X_1\Omega\Big((a_0^2+\frac{3}{4}a_1^2)\cos(\Omega t+\phi_1) + a_0a_1\sin(2\Omega t+2\phi_1) - \frac{3}{4}a_1^2\cos(3\Omega t+3\phi_1)\Big)\end{aligned} \tag{4.16}$$

where $a_1 = a_0X_1$. Equation (4.17) can be derived by substituting approximations of (4.16) in Equation (4.10):

$$\begin{aligned}i_a(t) =& V_{DC}C_\circ\Omega X_1\Big(a_2\cos(\Omega t+\phi_1) + a_0a_1\sin(2\Omega t+2\phi_1) - \frac{3}{4}a_1^2\cos(3\Omega t+3\phi_1)\Big)+\\ & V_{AC}C_\circ\Omega X_1\Big(a_2\cos(\Omega t+\phi_1) + a_0a_1\sin(2\Omega t+2\phi_1) - \frac{3}{4}a_1^2\cos(3\Omega t+3\phi_1)\Big)\sin(\Omega t)+\\ & V_{AC}C_\circ\Omega\Big((a_0+\frac{a_1^2}{2}) + a_1\sin(\Omega t+\phi_1) - \frac{a_1^2}{2}\cos(2\Omega t+2\phi_1)\Big)\cos(\Omega t),\end{aligned} \tag{4.17}$$

where $a_2 = a_0^2 + \frac{3}{4}a_1^2$. The general relation between the motion induced current and

displacement x and velocity $\dot{x}$ can be concluded by simplifying Equation (4.17) using trigonometric identities and collecting for frequency harmonics:

$$
\begin{aligned}
i_a(t) =& \frac{1}{2} V_{AC} C_\circ \Omega \sin(\phi_1)(a_1 - X_1 a_2) \\
&+ \Big(V_{DC} C_\circ \Omega X_1 a_2 \cos(\phi_1) + V_{AC} C_\circ \Omega \frac{3a_1^2}{4} \cos(2\phi_1) + V_{AC} C_\circ \Omega \big(a_0 + \frac{a_1^2}{2}\big) \Big) \cos(\Omega t) \\
&- \Big(V_{DC} C_\circ \Omega X_1 a_2 \sin(\phi_1) - V_{AC} C_\circ \Omega \frac{a_1^2}{4} \sin(2\phi_1) \Big) \sin(\Omega t) \\
&+ \Big(V_{DC} C_\circ \Omega a_1^2 \sin(2\phi_1) + V_{AC} C_\circ \Omega \frac{X_1 a_2 + a_1}{2} \sin(\phi_1) + V_{AC} C_\circ \Omega X_1 \frac{3a_1^2}{8} \sin(3\phi_1) \Big) \cos(2\Omega t) \\
&+ \Big(V_{DC} C_\circ \Omega a_1^2 \cos(2\phi_1) + V_{AC} C_\circ \Omega \frac{X_1 a_2 + a_1}{2} \cos(\phi_1) - V_{AC} C_\circ \Omega X_1 \frac{3a_1^2}{8} \cos(3\phi_1) \Big) \sin(2\Omega t) \\
&- \Big(V_{DC} C_\circ \Omega X_1 \frac{3a_1^2}{4} \cos(3\phi_1) - V_{AC} C_\circ \Omega \frac{3a_1^2}{4} \cos(2\phi_1) \Big) \cos(3\Omega t) \\
&+ \Big(V_{DC} C_\circ \Omega X_1 \frac{3a_1^2}{4} \sin(3\phi_1) + V_{AC} C_\circ \Omega \frac{3a_1^2}{4} \sin(2\phi_1) \Big) \sin(3\Omega t) \\
&- \Big(V_{AC} C_\circ \Omega X_1 \frac{3a_1^2}{8} \sin(3\phi_1) \Big) \cos(4\Omega t) \\
&- \Big(V_{AC} C_\circ \Omega X_1 \frac{3a_1^2}{8} \cos(3\phi_1) \Big) \sin(4\Omega t)
\end{aligned}
\tag{4.18}
$$

Henceforth, The biased actuation voltage at resonant frequency will be considered because the preliminary experiments showed promising results with this type of excitation. Consequently, $\Omega = \Omega_\circ$ and $\phi_1 = 90°$, hence Equation (4.18) will simplified as:

$$
\begin{aligned}
i_a(t) =& \frac{1}{2} V_{AC} C_\circ \Omega (a_1 - X_1 a_2) \\
&+ V_{AC} C_\circ \Omega \left(a_0 - \frac{a_1^2}{4} \right) \cos(\Omega t) - V_{DC} C_\circ \Omega X_1 a_2 \sin(\Omega t) \\
&+ V_{AC} C_\circ \Omega \left(\frac{a_0 a_1}{2} - \frac{a_1}{2} \right) \cos(2\Omega t) - V_{DC} C_\circ \Omega a_1^2 \sin(2\Omega t) \\
&- V_{AC} C_\circ \Omega \frac{3a_1^2}{4} \cos(3\Omega t) + V_{DC} C_\circ \Omega X_1 \frac{3a_1^2}{4} \sin(3\Omega t) \\
&+ V_{AC} C_\circ \Omega X_1 \frac{3a_1^2}{8} \cos(4\Omega t)
\end{aligned}
\tag{4.19}
$$

By substituting Equation (4.19) in (4.9) and shifting the coordinate system to the static deflection X_0 as the center, X_0 will be zero, and

$$
a_0 = 1 \ , \quad a_1 = X_1 \ , \quad a_2 = 1 + \frac{3}{4} X_1^2 .
$$

Consequently, the equation of current versus displacement can be derived as:

$$
\begin{aligned}
i(t) =& - V_{AC} C_\circ \Omega_\circ \frac{3}{8} X_1^3 \\
&+ V_{AC} C_p \Omega_\circ \cos(\Omega_\circ t) + V_{AC} C_\circ \Omega_\circ \left(1 - \frac{X_1^2}{4} \right) \cos(\Omega_\circ t) - V_{DC} C_\circ \Omega_\circ \left(X_1 + \frac{3}{4} X_1^3 \right) \sin(\Omega_\circ t) \\
&+ V_{AC} C_\circ \Omega_\circ X_1 \cos(2\Omega_\circ t) - V_{DC} C_\circ \Omega_\circ X_1^2 \sin(2\Omega_\circ t) \\
&- \frac{3}{4} V_{AC} C_\circ \Omega_\circ X_1^2 \cos(3\Omega_\circ t) - \frac{3}{4} V_{DC} C_\circ \Omega_\circ X_1^3 \sin(3\Omega_\circ t) \\
&+ \frac{3}{8} V_{AC} C_\circ \Omega_\circ X_1^3 \cos(4\Omega_\circ t).
\end{aligned}
\tag{4.20}
$$

The terms including the main harmonic $\Omega_\circ$ can not provide information about displacement

(X_1) because of the dominant value of $C_p >> C_\circ$ in the first term and its independence from X_1. The terms of third and fourth harmonics ($3\Omega_\circ$) and ($4\Omega_\circ$) have amplitudes proportional to X_1^2 an X_1^3 which are in the orders of $10^{-12}m^2$ and $10^{-18}m^3$ and can be ignored in comparison to X_1 which is in the order of $10^{-6}m$. As a consequence, they are not able to provide promising information regarding displacement.

All in all, the current at the second harmonic ($2\Omega_\circ$) is the only term which produces information about the displacement, as Equation (4.21) shows:

$$i(t) = V_{AC}C_\circ\Omega_\circ X_1 \cos(2\Omega_\circ t) \tag{4.21}$$

This current is proportional to the cantilever's velocity and can be measured by a lock-in amplifier tuned at $2\Omega_\circ$. Other parameters affecting this current are the AC component of actuation voltage, the initial gap between the counter-electrode and cantilever and the AFM probe's geometry.

Figure 4.3 illustrate the experimental results affirming this outcome. Figure 4.3a certifies the significant difference among current's magnitude at first harmonic and higher harmonics and its proportional relation to frequency only. Figure 4.3b depicts the constant value of phase versus frequency for harmonics 1, 3 and 4 and reveals the fact that these phase values are not affecting from cantilever's displacement. Figure 4.3c shows little amplitude of harmonics three and four compared to second harmonic, and their linear change with frequency. Figure 4.3d illustrates the resonant behavior of phase near to the resonant frequency only showed up by second harmonic.

Concluding, only second harmonic is showing the resonance effect versus frequency at

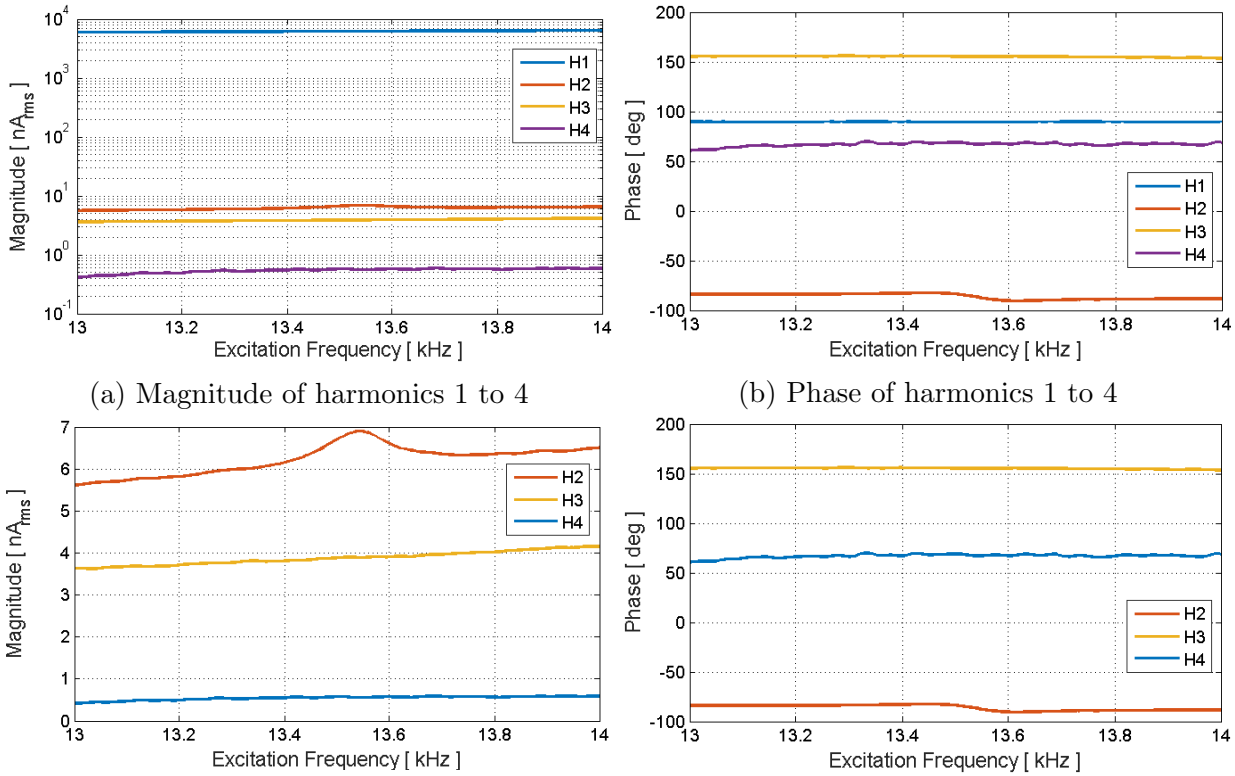

(a) Magnitude of harmonics 1 to 4

(b) Phase of harmonics 1 to 4

(c) Magnitude of harmonics 2 to 4

(d) Phase of harmonics 2 to 4

Figure 4.3: Experimental results of EAFM Prototype 1 current frequency response for four harmonics.

the resonant frequency $13.54kHz$ and the actuator's current at second harmonic provides robust information regarding EAFM probe's tip displacement.

4.2 System Model

For modeling the AFM probe Prototype 1 analytically, the methodology to describe the behavior of the cantilever in response to external excitations should be determined. In

the case of a long fixed-free cantilever with an electrostatic excitation which is not implied uniformly to the whole length of the beam, called *leveraged bending method* [22] in the literature, the lumped-mass model can not describe the exact reaction of the beam, because, the assumption of a concentrated mass at the end of the cantilever and a massless beam with spring constant k connecting the mass to the post is not realistic. Hence, a distributed-parameter model is necessary. The Euler-Bernoulli equation of motion considers the bending elements throughout the beam with respect to the position, therefore, it can describe the bending of the beam more effectively. The variables used to develop the model are listed in Table 4.1.

Table 4.1: List of variables in the analytical model

Variable	**Description**
L	Length of the beam (m)
b	Width of the beam (m)
h	Thickness of the beam (m)
d	Gap between the cantilever and the bottom electrode at rest (m)
A	Effective overlapping area of the cantilever and the bottom electrode $b \times B$ (m^2)
B	Width of the bottom electrode (m)
ρ	Density of probe's material (kg/m^3)
E	Young's modulus of probe's material (Pa)
I	Second moment of area for a rectangular beam (Nm^2)
$\epsilon_\circ$	Permittivity of air (F/m)
$\hat{c}$	Dimensional damping factor (kg/s)
$\hat{N}$	Dimensional tensile stress along the beam (N/m^2)
$\hat{v}(t)$	Dimensional actuation voltage (V)
$\hat{w}$	Dimensional displacement of cantilevers's tip (m)

Here, the linear equation of motion for the EAFM probe Prototype 1 consisting of a fixed-free microbeam and a fixed counter-electrode will be introduced, which is well known as the Bernoulli-Euler equation of motion and describes the transversal motion of the beam, $\hat{w}(\hat{x},\hat{t})$ at a distance $\hat{x}$ from the post at time $\hat{t}$ [58, 59].

$$EI\frac{\partial^4\hat{w}}{\partial\hat{x}^4}+\rho bh\frac{\partial^2\hat{w}}{\partial\hat{t}^2}+\hat{c}\frac{\partial\hat{w}}{\partial\hat{t}}=\Big[\frac{EA}{2L}\int_0^L\left(\frac{\partial\hat{w}}{\partial\hat{x}}\right)^2 d\hat{x}+\hat{N}\Big]\frac{\partial^2\hat{w}}{\partial\hat{x}^2}+\hat{F_{es}}(\hat{x})+F_{vdW} \tag{4.22}$$

In the right hand side of the equation of motion two different loads are implied to the cantilever. First, the effective electrostatic force or $F_{es}(\hat{x})$ exerted to a portion of the beam close to its post and causes the oscillation of the beam and governs the average separation to the sample's surface. This force can be represented by

$$F_{es}(\hat{x})=U\big(\hat{x}-\frac{B}{L}\big)\frac{\epsilon_\circ A\hat{v}^2(\hat{t})}{2(d-\hat{w})^2} \tag{4.23}$$

where $U(x)$ is the unit step function, defining the geometry of the bottom electrode compared to the cantilever.

Second, the van der Waal force acts between the cantilever's tip and the surface of the specimen and will affect the oscillation of the beam corresponding to the topography of the surface. According to molecular dynamics, the potential energy arising when two molecules come to their close vicinity is called Lennard-Jones potential and is represented in its general form by: [30, 27].

$$U_{LJ}=D\Big[E\Big(\frac{R}{r}\Big)^m-F\Big(\frac{R}{r}\Big)^n\Big] \tag{4.24}$$

while r is the distance between particles and m and n are integers and $m > n$. D, E and F are constants related to the materials, environment and specific conditions of the experiment. R is the intermolecular distance in which the non-bonded interactions between molecules emerge [30]. For a general definition in atomic force microscopy, $m = 12$ and $n = 6$ and the resultant Lennard-Jones force can be defined as [14]:

$$F_{LJ} = -24\epsilon \left[2\left(\frac{\sigma^{12}}{r^{13}}\right) - \left(\frac{\sigma^{6}}{r^{7}}\right) \right] \tag{4.25}$$

where ϵ (in meters) and σ (in J/mol) are parameters dependent on the particles.

To derive the potential energy between the AFM probe's tip and sample's surface, all the energies corresponding to the atoms of the tip and the atoms of the surface should be integrated to form the two-body potential of an atom on the tip nearest to the surface. For these calculations, usually the geometry of sphere-surface will be chosen. As a result, the van der Waal interaction for this geometry, based on the configuration depicted in Figure 4.4 is represented as [27, 20, 6]:

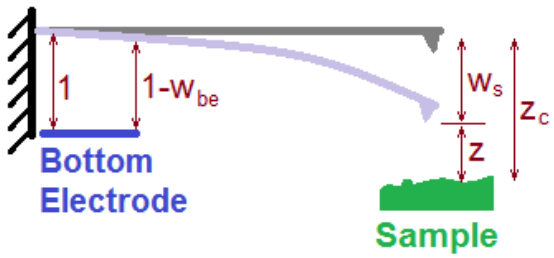

Figure 4.4: Geometry of EAFM Prototype 1 used to explain the van der Waal force.

$$
\begin{aligned}
F_{vdW} &= -\frac{HR}{6z^2}, \quad z \geq a_\circ \\
F_{DWT} &= -\frac{HR}{6a_\circ^2} + \frac{4}{3}E^*\sqrt{R}(a_\circ - z)^{3/2}, \quad z < a_\circ \\
\frac{1}{E^*} &= \frac{1-\nu_t^2}{E_t} + \frac{1-\nu_s^2}{E_s}
\end{aligned} \tag{4.26}
$$

where F_{vdW} is the van der Waal non-contact force for tip-sample distances larger than $a_\circ$ with an attractive nature, F_{DWT} is the Derjaguin–Muller–Toporov contact force when the tip-sample separation is smaller than $a_\circ$ with a repulsive nature, $a_\circ$ is the intermolecular distance at which two objects are considered to be in contact, H is the Hamaker constant, R is the tip's radius wich is assumed to be much larger than $a_\circ$ and E_t, ν_t and E_s, ν_s are the Young's modulus and Poisson coefficients of the tip and sample respectively.

Hamaker constant H is represented by [27]:

$$H = \pi^2 C \rho_1 \rho_2$$

where C is a constant related to the material properties and is equal to $10^{-77} Jm^6$ for solids. ρ_1 and ρ_2 are the densities of materials at the tip and the sample. Considering both the tip and the sample have dense materials, $\rho_1 \approx \rho_2 = 3 \times 10^{28} m^{-3}$, then H will be $10^{-19} J$ in vacuum.

The geometry of the tip and the sample in Figure 4.4 illustrates that electrostatic force $F_{es}(\hat{x})$ and van der Waal force F_{LJ} are independent of each other and modeled in the literature based on two different approaches [58, 9]. Table 4.2 shows the geometric and material specifications of two different AFM probes from Bruker® Corporation [15],

namely the RESPA™ and SCM-PIT™. In the following calculations, nominal values will be used.

Table 4.2: (Bruker™ AFM Probes Specifications)

Parameter	**Value**						**Unit**	**Description**
	RESPA			SCM-PIT				
	Nom.	Min.	Max.	Nom.	Min.	Max.		
L	450	440	460	225	200	250	μm	Length
b	35	33	37	28	23	33	μm	Width
h	1.8	1.05	2.75	2.5	2	3.5	μm	Thickness
k	0.1	0.03	0.2	2.8	1	5	N/m	Spring Constant
f_0	10	4	16	75	50	100	kHz	First Natural Frequency
σ	0.01 to 0.025						$\Omega \cdot cm$	Resistivity
ρ	2330						kg/m^3	Density
	Antimony n doped silicon						–	Material

The analytical model will be derived based on Reduced-order modeling exploiting the equation of motion in Equation (4.22) by applying the Galerkin Method [58].

4.2.1 Structural Analysis

In this analysis, the first five natural frequencies and the first five modeshapes of the RESPA™ cantilever are investigated (refer to Table 4.2 for dimensions). To benefit the advantages of simpler formula and the ability to compare the results of analyses for different structures, the Equation (4.22) will be normalized using the following normalizing

equations:

$$w = \frac{\hat{w}}{d}, \quad x = \frac{\hat{x}}{L}, \quad t = \frac{\hat{t}}{T}, \quad T = \sqrt{\frac{\rho b h L}{\frac{6EI}{L^3}}}, \quad c = \frac{\hat{c}}{\frac{EIT}{L^4}}, \quad N = \frac{\hat{N}}{\frac{EI}{L^2}}, \quad F_{es} = \frac{\hat{F_{es}}}{\frac{EI}{L^3}}$$

By substituting the normalizing equations in (4.22), this model can be reduced to:

$$\frac{\partial^4 w}{\partial x^4} - N\frac{\partial^2 w}{\partial x^2} + \frac{\partial^2 w}{\partial t^2} + c\frac{\partial w}{\partial t} = F_{es}(x). \tag{4.27}$$

In the absence of damping and by neglecting the axial force and no input force, Equation (4.27) can be written in the form of:

$$\frac{\partial^4 w}{\partial x^4} + \frac{\partial^2 w}{\partial t^2} = 0. \tag{4.28}$$

Solving this equation is known as the *Eigenvalue Problem* and tends to be the general solution of $w(x,t) = \phi(x)e^{j\omega t}$ where $j = \sqrt{-1}$ and ω is the natural frequency. Substituting this equation in (4.28) and some math manipulation yields to the following general form for $\phi(x)$:

$$\phi(x) = A\cos(\beta x) + B\sin(\beta x) + C\cosh(\beta x) + D\sinh(\beta x) \tag{4.29}$$

where $\beta = \sqrt{\omega}$. A, B, C and D are specific to each problem and can be determined by the boundary conditions of that problem. For a fixed-free beam, determining the constants A to D tends to the characteristic function for a cantilever:

$$1 + \cos(\beta_i)\cosh(\beta_i) = 0 \tag{4.30}$$

This equation has infinite solutions where $\beta_i = \sqrt{\omega_i}$ is a representative of the eigenfrequencies or natural frequencies of the cantilever. These eigenfrequencies are corresponding to $\phi_i(x)$ or eigenvectors (modeshapes). The five first natural frequencies and modeshapes are considered but later, it will be seen that only the first three eigenvectors have the most contribution in shaping the final displacement $w(x,t)$.

The first five nondimensional ω_i and modeshapes are listed in Table 4.3 and Figure 4.5 shows the five modeshapes of the $450\mu m$ cantilever.

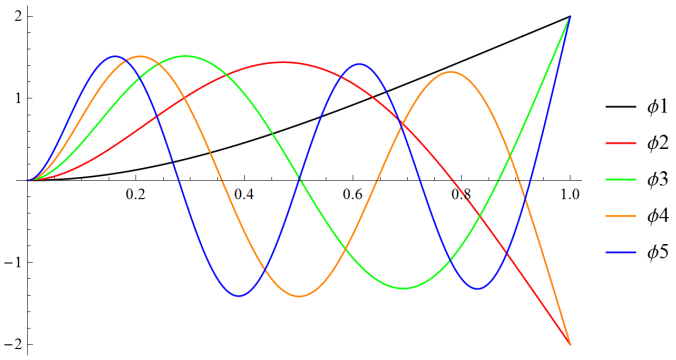

Figure 4.5: The first five mode shapes of the 450 μm cantilever

4.2.2 Analysis under Electrostatic Actuation

According to the intrinsic nonlinearity in electrostatic actuation, the static behavior of microelectromechanical devices will differ from the structural response. On the other hand, one of the most important information in electrostatic actuation of MEMS devices is the pull-in voltage and its corresponding pull-in distance. These information are crucial in both AFM devices designed for this project because an estimation about the actuation voltage

Table 4.3: List of natural frequencies, mode shapes and model coordinates in the analytical model (all quantities are nondimensional)

i	ω_i	$\phi_i(x)$	$u_i(t)$
1	3.516	$0.7341\sin(1.8751x) - \cos(1.8751x) -$ $0.7341\sinh(1.8751x) + \cosh(1.8751x)$	245.853×10^{-6}
2	22.035	$1.01847\sin(4.6941x) - \cos(4.6941x) -$ $1.0185\sinh(4.6941x) + \cosh(4.6941x)$	31.2431×10^{-6}
3	61.697	$0.9992\sin(7.8548x) - \cos(7.8548x) -$ $0.9992\sinh(7.8548x) + \cosh(7.8548x)$	8.6858×10^{-6}
4	120.902	$\sin(10.9955x) - \cos(10.9955x) -$ $\sinh(10.9955x) + \cosh(10.9955x)$	3.2413×10^{-6}
5	199.856	$0.9999\sin(14.1372x) - \cos(14.1372x) -$ $0.9999\sinh(14.1372x) + \cosh(14.1372x)$	1.3398×10^{-6}

is necessary to manage the average distance between the tip and the sample's surface as well as the amplitude of oscillation to keep the AFM probe working in the desired mode. In fact, unlike other MEMS devices, the pull-in phenomenon in Prototype 1 is different from other electrostatic actuators as the tip of the AFM cantilever is hovering above the sample's surface not on the substrate of the electrostatic actuator. As a result, based on the position of the specimen on the XY&Z positioner, the pull-in may have different meanings.

4.2.3 Static Analysis for EAFM Prototype 1

The static behavior of the cantilever for Prototype 1 has been modeled in this section. In Galerkin Method, using the expansion theorem [58], the discretized variables can be defined as

$$w(x,t) = \sum_{i=1}^{n} u_i(t)\phi_i(t) \tag{4.31}$$

while $\phi_i(t)$ are orthonormal functions expressing the mode shapes and $u_i(t)$ are model coordinates. These functions are listed in Table 4.3. By substituting this equation in the equation of motion (4.22), and continuing the math, the bifurcation curve or the static response of the AFM probe to the DC actuation voltage for a given gap ($d = 6\mu m$) shown in Figure 4.6 will be derived.

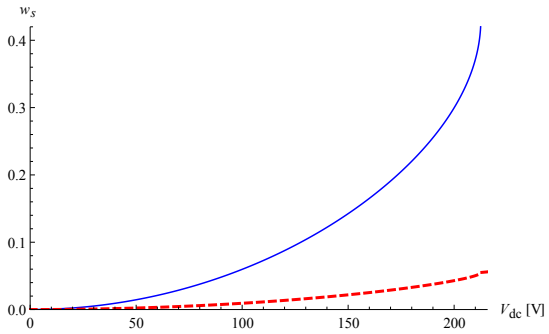

Figure 4.6: The displacement of AFM probe versus DC actuation voltage for a gap of $d = 6\mu m$ in the absense of van der Waasl force. Solid: normalized displacement at the tip, dashed: normalized displacement at the bottom electrode.

Figure 4.6 also reveals the static pull-in voltage as $247.8V$ and the nondimensional pull-in distance as 0.416. According to the structure of AFM probe in Prototype 1 and the gap between the cantilever and the bottom electrode, it is very important to know the

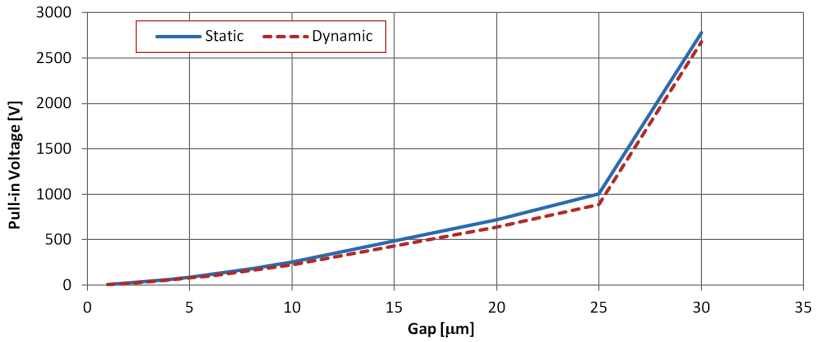

Figure 4.7: Pull-in voltages versus gap for a $450\mu m$ long cantilever. For gaps greater than $6\mu m$, pull-in voltages are drastically high.

range of pull-in voltages in terms of the gap. This information was calculated using the analytical model in the absence of van der Waal force and the result is depicted in Figure 4.7.

The next important information about the AFM probe Prototype 1 is the effect of the width of the bottom electrode compared to the length of the cantilever. As explained in section 3.1.1, the bottom electrode which is a track very close to the edge of the PCB, is responsible for providing the actuation signal to the AFM probe and functions as the fixed electrode of the electrostatic actuator. The width of this track has a crucial effect on the static behavior of the AFM probe. Figure 4.8a shows the effect of this width on pull-in voltage and pull-in distance. Figure 4.8b depicts the change in bifurcation curves for different bottom electrode widths.

Figures 4.8a and 4.8b show that using wider bottom electrode will provide us with lower actuation voltages, however, according to the AFM probe's structure, some space under the free end of the cantilever is needed for the specimen and the sample holder. Therefore,

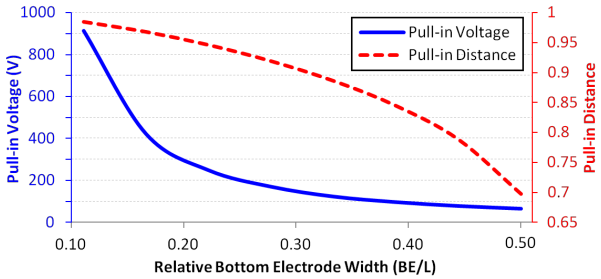

(a) pull-in voltage and pull-in distance vs bottom electrode's width

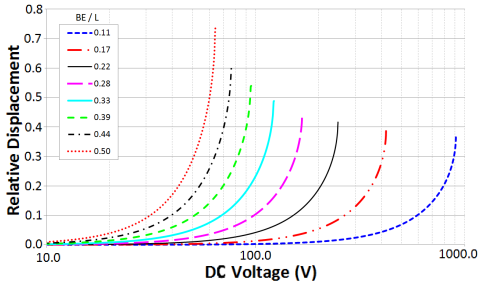

(b) Bifurcation curves vs bottom electrode's width

Figure 4.8: The effect of the bottom electrode width on the pull-in voltage, pull-in distance and bifurcation curves of the EAFM Prototype 1.

the width of the bottom electrode was selected to be 1/4 of the length of the cantilever. Referring to the experimental results, The dynamics of Prototype 1 is not mentioned here, because according to the device's geometry, the cantilever of this prototype acts as a regular resonator and does not show significant behavior worth to study.

The Effect of van der Waal Force on Pull-in Voltage and Tip Displacement

The next interesting study was the effect of van der Waal force on the pull-in voltage and tip's displacement under the electrostatic actuation. The pull-in voltage will be investigated first. By applying the van der Waal force to the model, there will be a sudden change in the pull-in voltage at $z_c = 0.058$. Figure 4.9 shows this change for an EAFM prototype 1 device when the gap between the cantilever and bottom electrode is $10\mu m$. Below the certain tip-sample distance, the pull-in voltage is negligibly small because of the strong attractive force between the tip and the sample.

Tip displacement demonstrates a similar behavior versus tip-sample separation. Figure

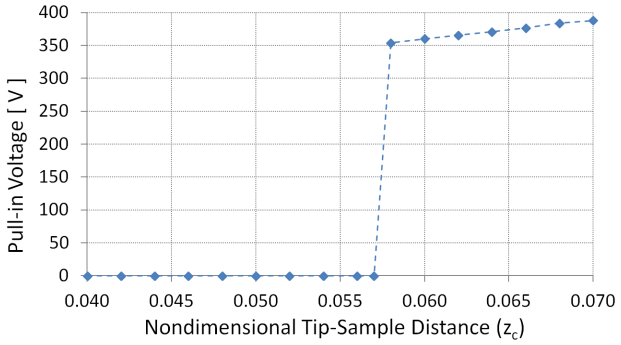

Figure 4.9: Pull-in voltages versus tip-sample separation for a $450\mu m$ long cantilever for gap $= 10\mu m$.

4.10 depicts this behavior. For high values of z_c, the displacement will be decayed by reducing z_c because of the effect of long-range attractive forces. At a certain value of z_c, there is an abrupt increase in displacement because of stronger attractive forces. Then the displacement will decrease linearly. This outcome is in accordance with results proposed in [20].

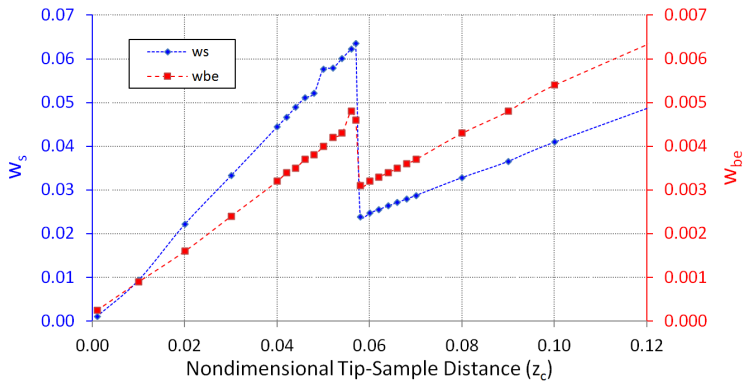

Figure 4.10: Displacements of two points on the AFM's cantilever: at the end and at the bottom electrode, gap $= 10\mu m$.

4.2.4 Dynamic Analysis of Prototype 2 in Tapping mode

The behavior of the electrostatic actuator under dynamic excitation is always of interest, specifically when there is a need to information about the actuator in tapping mode. Therefore, the dynamic analysis for a cantilever with dimensions mentioned in Table 4.2 with the actuation voltage of $V_a(t) = 47.5 + 47.5\sin(2\pi f_\circ t)$ where $f_\circ = 11.9kHz$ will be studied. The gap between the cantilever and the counter electrode was $20\mu m$. In this study, only first-mode analysis will be considered.

The outcomes of analytical and experimental results in this section will be compared to a comprehensive numerical analysis on the dynamics of AFM cantilevers in tapping mode proposed in [6]. It is important to note that excitation method in this report is based on piezoelectric actuation with linear relation between the force and the applied amplitude and the output parameter is tip's displacement. In our research, the applied force to the cantilever is electrostatic, hence, intrinsically nonlinear and the output parameter is actuator's current.

The results of first-mode analysis have been demonstrated as displacement and velocity frequency responses versus the tip-sample distance in Figure 4.11.

The flat tops of displacement curves in Figure 4.11b show the effect of tapping which means the displacement is limited by the tip-sample distance. This curve is in agreement to the displacement's frequency response proposed in [6]. In fact, the results regarding $z = 16\mu m$ (blue curve) obtained in this research are compatible with mode-one analysis in [6]. By decreasing the tip-sample distance, which is similar to increasing the cantilever's input amplitude, some fluctuations appear at frequencies that a flat top begins. These variations

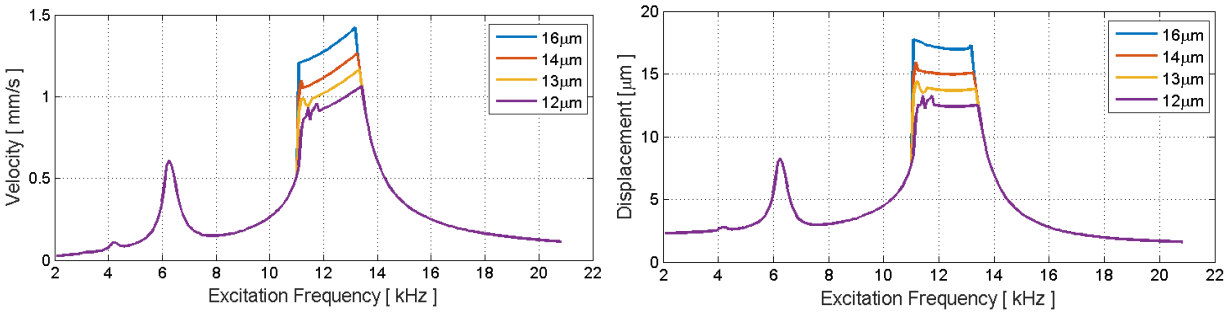

(a) Velocity

(b) Displacement

Figure 4.11: Dimensional (a) velocity and (b) displacement for the cantilever of Table 4.2.

illustrate the effect of chaos caused by grazing bifurcation in cantilever's tip vibration at these specific frequencies. This is the characteristic of an impact oscillator. While the excitation frequency grows, the displacement (velocity) settles to a stable amount showing the instability has been liquidated. By further decreasing the tip-sample distance, the effect of chaotic variations will continue to persist for more frequencies. This consequence fit to the discussions presented in [6].

Figures 4.11a and 4.11b also show the effect of period doubling in the analysis of this research.

The phase portraits of each tip-sample distance are important sources of information which are sketched in Figure 4.12 based on the last ten cycles of the time histories at the resonant frequency $f_\circ = 11.9kHz$. The following points can be derived from these phase portraits:

- All phase portraits show the flat region which corresponds to the limitation in displacement because of tapping.

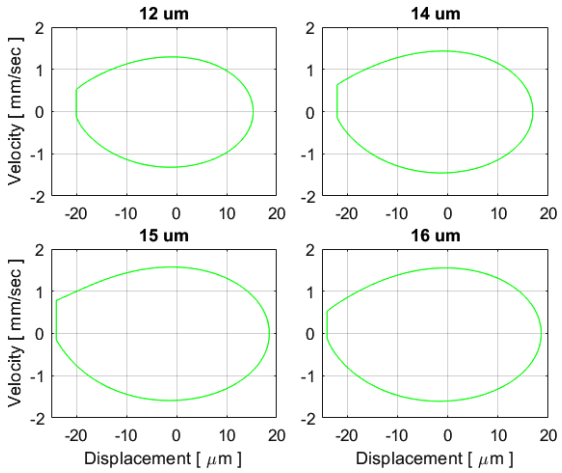

Figure 4.12: Phase portraits versus tip-sample distance for the $450\mu m$ cantilever.

- All phase portraits are asymmetric to $w = 0$ or the rest position of the cantilever because of the static deflection. The static deflection depends on gap, the tip-sample distance and actuation voltage.

- The flat region in displacement causes a sudden jump in the direction of the velocity which is expected from the dynamic behavior of harmonic oscillators.

- The flat region is in the negative plane of displacement because the sample and the counter electrode are in two sides of the cantilever and $w(t)$ has a positive sign when it deflects toward the counter electrode.

To compare the analytical result to experimental results, the outcomes of current measurement in tapping mode are illustrated in Figure 4.13. This Figure includes current's magnitude and phase curves versus frequency for different tip-sample distances. For better comparison, current responses for fly mode and contact mode are also included. Figure

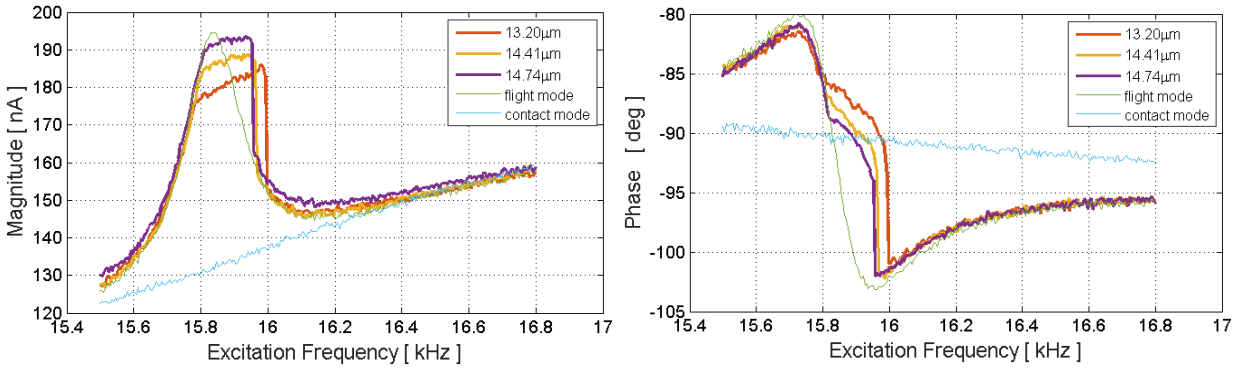

(a) Magnitude (b) Phase

Figure 4.13: Experimental results for current's magnitude versus frequency in tapping mode for different tip-sample distances.

4.13a shows the similarity between the current's magnitude of AFM probe and cantilever's velocity in Figure 4.11a because of the $\Omega_{\circ}X_1$ term in Equation (4.21) in the shape of flat tops. Moreover, the magnitude of current decreases as the sample gets closer to the cantilever's tip. The next point is, the range of frequencies at which the magnitude stays at its flat top is inversely related to the tip-sample separation. This experimental results These flat tops can be interpreted as an impact oscillation with a grazing bifurcation at these frequencies. It was observed that if the actuation voltage was decreased, the current magnitude showed the behavior of a smooth oscillator instead of impact oscillator at the same frequencies. It is expected that for a known actuation voltage and a fixed excitation frequency (like the cantilever's resonant frequency), a chaotic behavior emerges at tip-sample distances that tapping starts. To examine this expectation, the so-called 'magnitude noise' and 'phase noise' were sketched by deriving the amount of fluctuations at different tip-sample distances starting from free running mode and ending up at contact mode. The same procedure explained in section 5.4.1 for calibration curves was employed

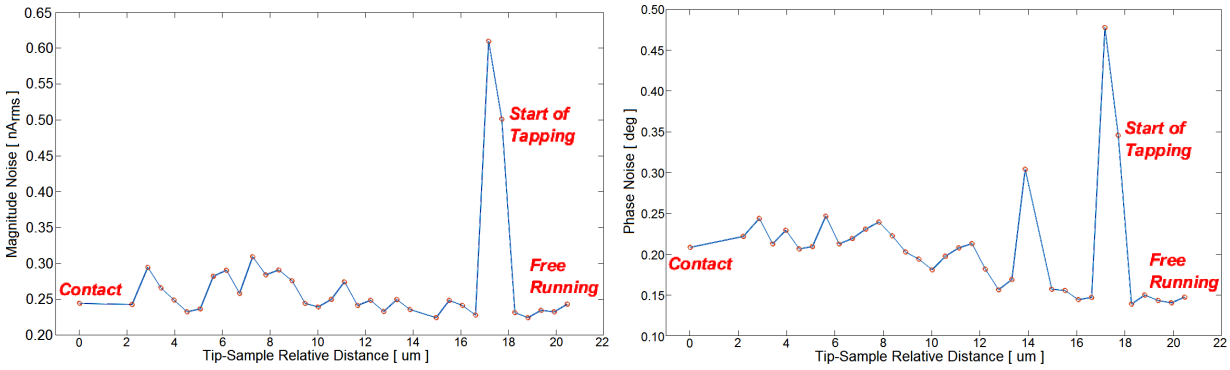

(a) Magnitude Noise (b) Phase Noise

Figure 4.14: Experimental results for Magnitude Noise and Phase Noise versus tip-sample distance. $V(t) = 75 + 75\sin(2\pi f_\circ t), f_\circ = 10.54kHz$

here.

For measuring the variations, the local regression of the data called '*Local regression using weighted linear least squares and a* 2^{nd} *degree polynomial model*' was subtracted from the real value of data at each tip-sample distance. The outcome of this procedure is sketched as Magnitude Noise and Phase Noise curves illustrated in Figure 4.14: These curves also certify the amplification of fluctuations at distances which the impact phenomenon starts to emerge. This is equivalent to the grazing bifurcation and leads to chaos in terms of displacement and velocity and have been discussed. As explained in [6], the tip's oscillations will be converged to a periodic attractor in phase plane which can be translated to low amount of magnitude and phase noise in terms of current measurement.

As a conclusion, although the dynamic analysis of tapping mode in this research did not support higher modes of Galerkin discretization, the analysis results for first mode and the experimental measurements comply with the analysis results proposed in [6].

4.3 Finite Element Simulation

4.3.1 Structural Analysis

Figure 4.15 shows the first six modeshapes of the AFM cantilever calculated by COMSOL. Modes 4 and 5 are not out-of-plane and can not be calculated by the analytical model. The eigenfrequencies corresponding to these modeshapes are listed in Table 4.4. This table also shows the natural frequencies from the analytical model for comparison. Table 4.4 shows that the natural frequencies calculated by two methods are very close.

Table 4.4: List of natural frequencies calculated by the FEM software and analytical model.

Method	**Mode** 1	**Mode** 2	**Mode** 3	**Mode** 4	**Mode** 5
Analytical	12231	75539	211511	414477	685161
COMSOL	12327	77235	216330	424210	N/A

Figure 4.15 illustrates four modeshapes with out-of-plane motion, one modeshape with in-plane vibration and one modeshape with torsional vibration.

4.3.2 Analysis Under Electrostatic Force

The result of COMSOL static analysis for the first modeshape deflection of AFM probe's cantilever is an important piece of information because of the dominant amplitude of the first modeshape.

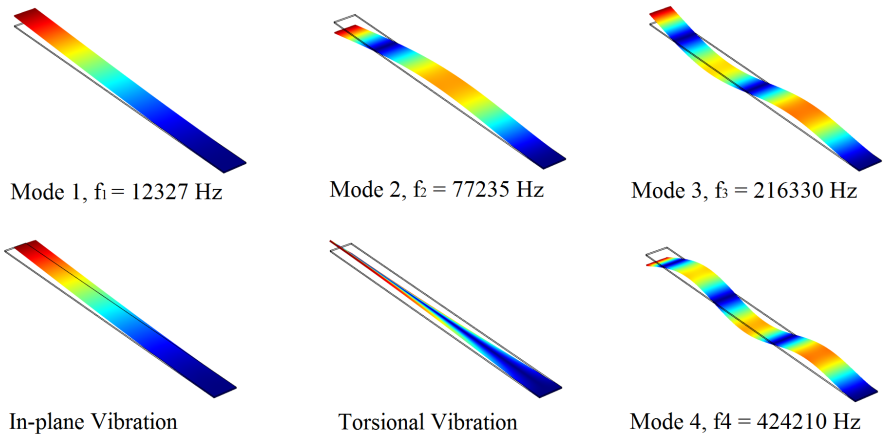

Figure 4.15: The modeshapes of the $450\mu m$ cantilever calculated by COMSOL

In this part, the parameters listed in Table 4.5 are used. The maximum deflection under a test force of $1\mu m$ is shown in Figure 4.16. Figure 4.17 depicts the softening effect of electrostatic force, namely, the cantilever's resonant frequency versus applied voltage.

4.3.3 Dynamic Analysis

The response of AFM probe's structure against the actuation voltage $V_a(t) = 75+\sin(2\pi 10400t)$ with a constant V_{DC} was the target of this simulation. Parameters used for this analysis are listed in Table 4.6 and the results are depicted in Figure 4.18a for $V_{AC} < 10V_{pp}$ and Figure 4.18b for $10V_{pp} < V_{AC} < 60V_{pp}$.

Figure 4.18 clarifies the softening effect of electrostatic actuators versus actuation voltages beyond 10 V_{pp}. We can see for voltages below 10 V_{pp} the decay in the resonant frequency is negligible. These results are in compliance with the experimental results for

Table 4.5: List of parameters for COMSOL dynamic analysis

Name	Expression	Value	Description
L_b	450 $[\mu m]$	4.5×10^{-4} m	Length of Beam
W_b	45 $[\mu m]$	4.5×10^{-5} m	Width of Beam
H_b	1.8 $[\mu m]$	1.8×10^{-6} m	Thickness of Beam
Y_b	130 [GPa]	1.3×10^{11} Pa	Modulus of Beam
ρ_b	2325 $[kg/m^3]$	2325 kg/m^3	Density of Beam
D_a	30 $[\mu m]$	3×10^{-5} m	Gap
F_{test}	1 $[\mu N]$	1×10^{-6} N	Test mechanical Force

current's magnitude depicted in Figure 4.18c and Figure 4.18d.

4.4 Summary

The first part of this chapter was dedicated to the development of the relation between the EAFM probe's displacement (or velocity) and the electrostatic actuator's current. The mathematical analysis showed a linear relation between the current's magnitude and tip's velocity at the second harmonic of a biased actuation voltage. It was approved that higher harmonics do not have significant contribution in current measurement.

From this point on, the structural and the static analysis for EAFM probe Prototype 1 was initiated by using the reduced-order model and Galerkin method to solve the equation of motion. This analysis included the electrostatic actuation force and the van der Waal surface force.

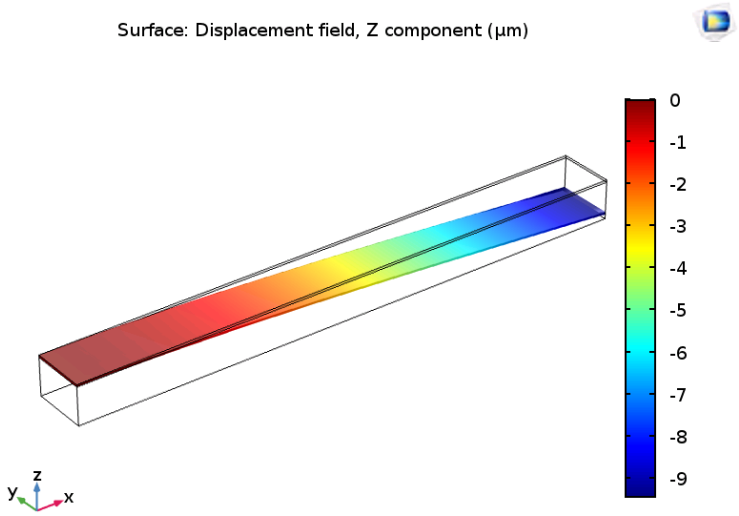

Figure 4.16: First modeshape of probe's cantilever under test force of $1\mu N$

The next section covered a dynamic analysis for the EAFM device Prototype 2 in tapping mode. The results were compared to experimental results in tapping mode. In each case, the outcomes were compared to results proposed in the literature. The comparison showed compatibility among the results.

Finally, a numerical analysis including structural, static and dynamic investigations using COMSOL was run. The dynamic analysis was employed to study the behavior of the EAFM probe's cantilever under different actuation conditions. Comparing the outcomes to the experimental results showed adaptability.

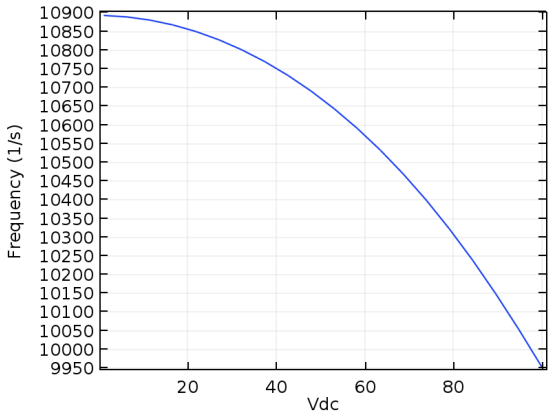

Figure 4.17: The decay in resonant frequency caused by electrostatic force versus applied DC voltage.

Table 4.6: List of parameters for COMSOL dynamic analysis for the structure of Table 4.5

Name	Expression	Value	Description
V_{DC}	75 [V]	75 V	DC Value of Actuation Voltage
V_{AC}	1 [V_{pp}]	1 V	AC Value of Actuation Voltage
V_{rms}	$\sqrt{V_{DC}^2 + 0.5V_{AC}^2}$	75.003 V	RMS Value of Actuation Voltage
V_{pk}	$\sqrt{2 \times V_{DC} \times V_{AC}}$	12.247 V	Peak Value of Actuation Voltage
$f_\circ$	10.4 [kHz]	10400 Hz	First Eigenfrequency
Q	20	20	Quality Factor
ζ	1/Q	0.05	Damping Factor
BW	$f_\circ/Q$	520 Hz	Bandwidth
f_1	$f_\circ - 2 \times BW$	9360 Hz	Start Frequency
f_2	$f_\circ + 2 \times BW$	11440 Hz	Stop Frequency
Nf	500	500	Number of

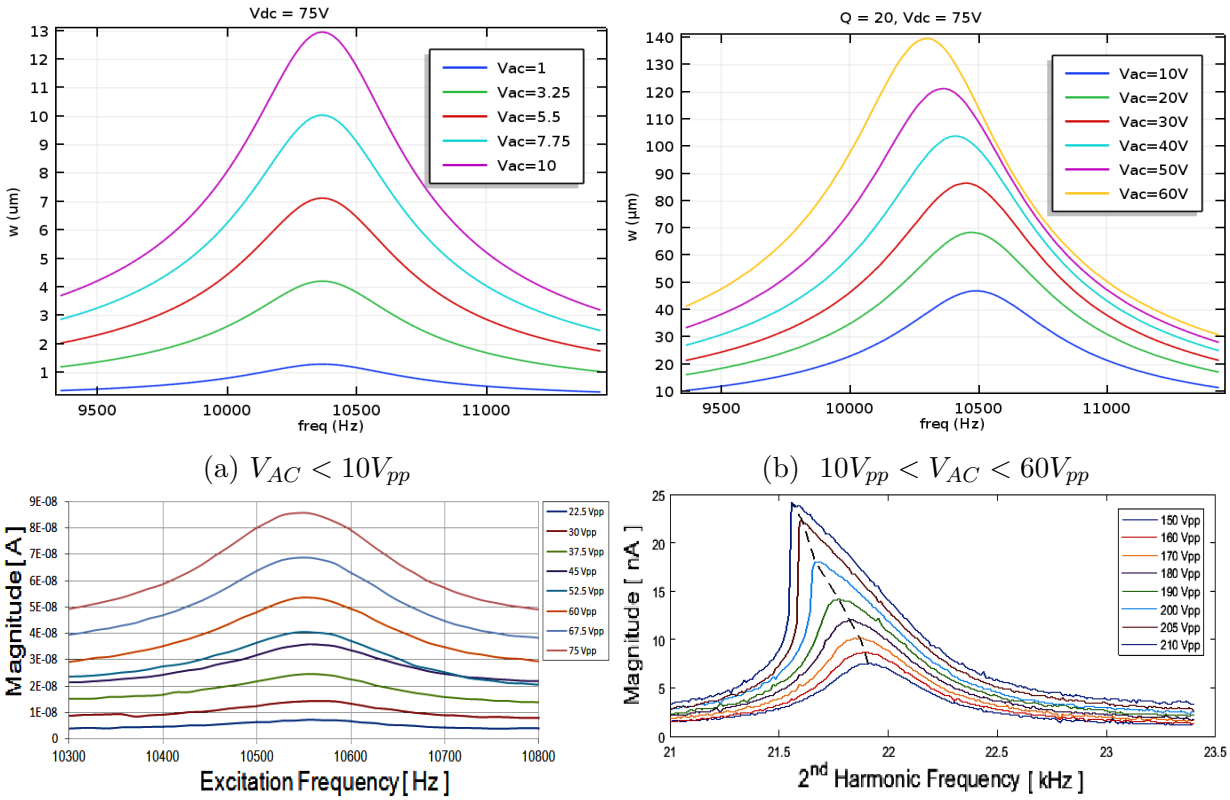

(a) $V_{AC} < 10V_{pp}$

(b) $10V_{pp} < V_{AC} < 60V_{pp}$

(c) $V_{AC} < 100V_{pp}$

(d) $V_{AC} > 150V_{pp}$

Figure 4.18: (a) and (b) numerical analysis results for AFM probe's beam displacement versus dynamic force V_{AC} with $V_{DC} = 75V$; related to Table 4.6; (c) and (d) experimental results of EAFM Prototype 2 for different V_{AC} values while $V_{DC} = 100V$. The device's gap in the experimental results were different from the one used in simulation.

Chapter 5

Experimental Results

In this chapter, the outcomes of the experiments are proposed to show the performance of capacitive detection for surface force scanning. The information acquired from the measurement's setup are the magnitude ($|i_a(t)|$), phase ($\measuredangle i_a(t)$), $X = |i_a(t)|\cos(\measuredangle i_a(t))$ and $Y = |i_a(t)|\sin(\measuredangle i_a(t))$ where $i_a(t)$ is the motion induced current.

5.1 Experimental Setup

The setup used for these experiments is shown in 5.1. The excitation frequency was the cantilever's mechanical resonant frequency ($f_\circ$) and in majority of the experiments, the measurements (observations) were in the second harmonic of the excitation frequency ($2f_\circ$) because of the biased actuation voltage $V_a(t) = V_{DC} + V_{AC}\sin(2\pi ft)$.

Figures 5.2 and 5.3 try to illustrate a comparison among the magnitude and phase of

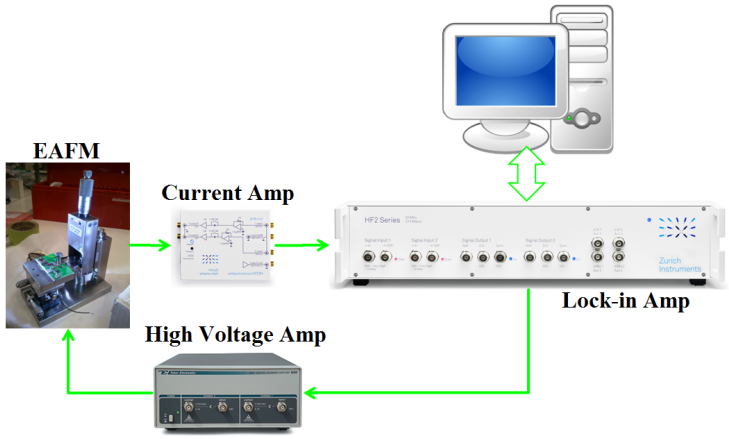

Figure 5.1: Experimental setup used for scanning.

harmonics 1 to 6.

As explained in section 4.1.2 and is evident from Figure 5.2a, the magnitude of first harmonic is three orders of magnitude higher than second harmonic and linear in all frequencies. The phase of first harmonic is also constant in all frequencies. Consequently, they can not provide promising information about the cantilever's vibration in a specific frequency range, even though the magnitude has the purpose of measuring the parasitic capacitance in the AFM device.

In fact, it was shown in section 4.1.2 that second harmonic is the best representative of the motion induced current. It is evident through the dominance of the magnitude of second harmonic in frequencies close to the resonant frequency in Figures 5.3a and 5.3b.

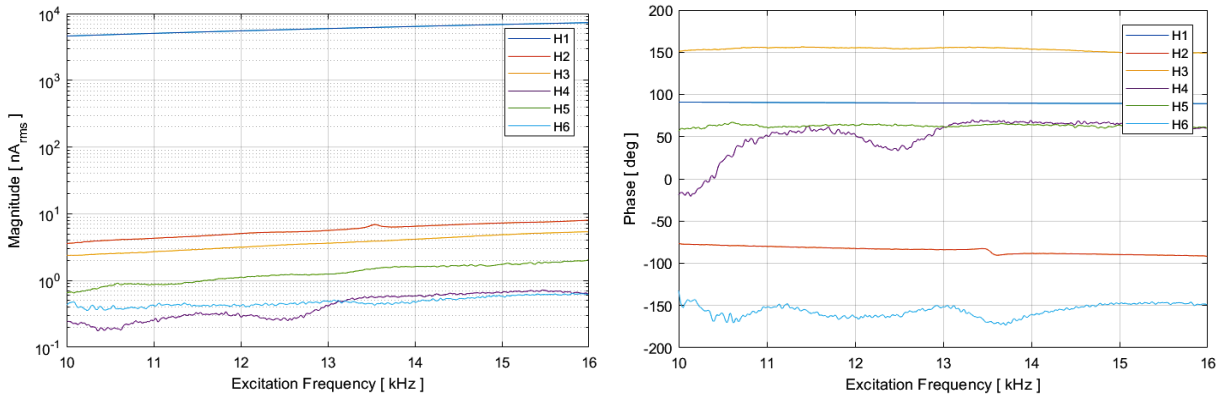

(a) Magnitude (b) Phase

Figure 5.2: Frequency responses of first six harmonics of EAFM Prototype 1 current in the frequency range of 10 to 16kHz with $V(t) = 75 + 75\sin(2\pi f_{\circ} t)$, $f_{\circ} = 13.54kHz$.

5.2 Experimental Approach

The experiments were arranged in three steps, first the response of the detection system to changes in the actuation voltage and the effect of tip-sample distance on current's frequency response were investigated, to derive the calibration curves by using Fixture 1 (described in section 3.2.1).

Second, single-line scanning of an random sample was performed in different line lengths, while exploiting the 1-D piezoscanner.

Lastly, by adding the manual micrometer to the fixture, as demonstrated in section 3.2.3, scanning several lines of the specimen was performed. Then, a semi-automatic raster scanning was implemented after exploiting the motorized XY-stage as explained in section 3.2.4.

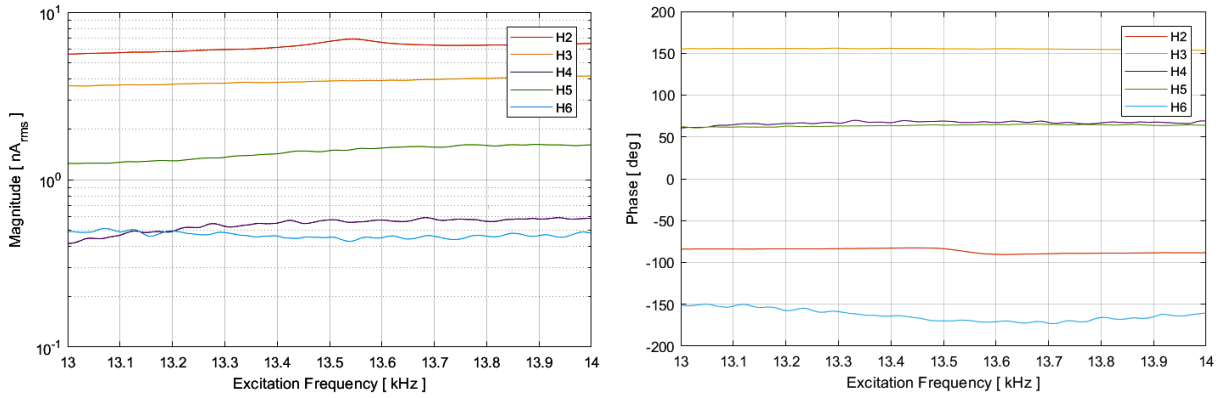

(a) Magnitude (b) Phase

Figure 5.3: Frequency responses of harmonics 2 to 6 of EAFM Prototype 1 current in the frequency range of 13 to 14 kHz with $V(t) = 75 + 75\sin(\Omega t)$.

5.3 Single-point Experiments

Single-point tests were performed in the first step of scanning experiments. Three main goals were pursued in this part:

1. Investigating the effect of actuation voltages on the behavior of electrostatic detection scheme.

2. Finding optimum parameters of the actuation voltage $V_a(t) = V_{DC} + V_{AC}\sin(2\pi f_\circ t)$.

3. Deriving the calibration curves for the developed capacitive detection system in tapping mode to find the optimum tip-sample distance.

The outcomes of the experiments will be discussed in the following.

5.3.1 The Effect of Actuation Voltage Levels

This feature is very important because of its direct impact on the parameters measured as the source of information for the scanning process and producing output images. It is worth repeating that all the measurements in this part are based on the EAFM probe's current measured at the second harmonic of the excitation frequency. This frequency is equal or very close to the probe's mechanical resonant frequency.

The electrostatic force has a quadratic relation with the actuation voltage. Same behavior could be seen in current's magnitude vs actuation voltage. The sweeping feature of Zürich Instruments HF2LI™ lock-in amplifier was used to test this relation in our EAFM devices. This feature was employed to sweep the DC voltage, the AC voltage or the frequency.

Prototype 1

Figure 5.4a illustrates the magnitude and phase of current vs changing in V_{AC} and Figure 5.4b shows the current vs V_{DC} for the first EAFM probe design (section 3.1.1). Both graphs show similar quadratic trends for magnitude but different trends for phase.

Prototype 2

In this part we tested the actuator's current versus excitation voltage in three different tip-sample distances, namely high, corresponding to free-running mode, medium, corresponding to tapping mode, and low, corresponding to contact mode.

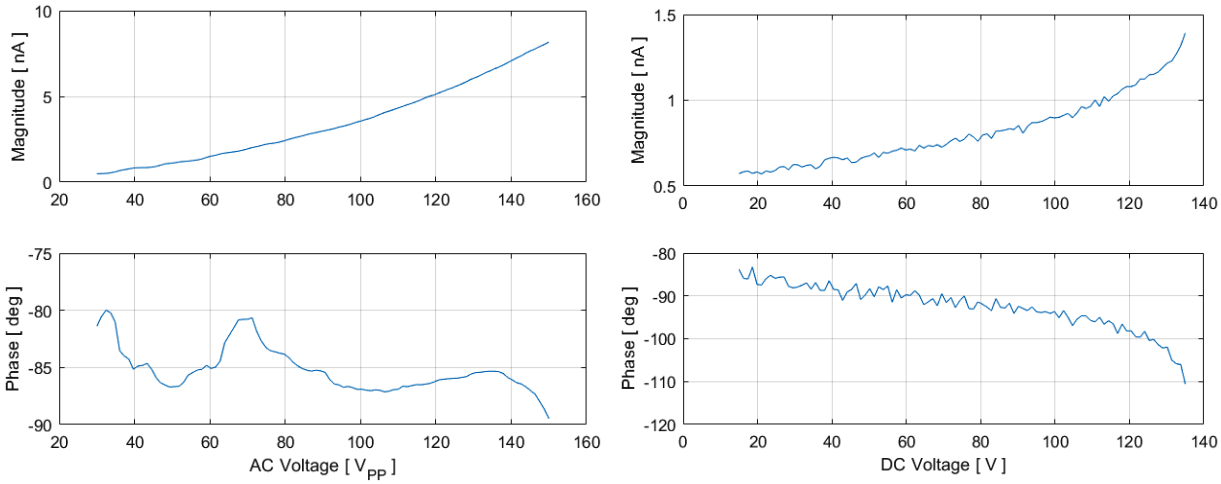

(a) Sweeping V_{AC} while $V_{DC} = 75V$

(b) Sweeping V_{DC} while $V_{AC} = 15.75V_{PP}$

Figure 5.4: Current versus changes in actuation voltage parameters for EAFM device 1 in free running mode.

High Tip-Sample Separation: Free-running Mode

Figure 5.5a illustrates the magnitude and phase of current versus changing V_{AC} and Figure 5.5b shows the current versus V_{DC} for the second EAFM probe design (section 3.1.2). Similar to EAFM first design, both graphs show similar quadratic trends for magnitude but different trends for phase. The phase responses are in compliance to results of first EAFM probe design.

Medium Tip-Sample Separation: Tapping Mode

Figure 5.6a shows the magnitude and phase of second design's current versus changing V_{DC}. The output curves have been derived by measuring the current's magnitude and phase at the resonant frequency, 10568Hz. The magnitude shows quadratic trend while phase has an almost linear trend, in compliance to results of first EAFM probe design. We will see later that this feature can be used as a matter of measurements for tip-sample

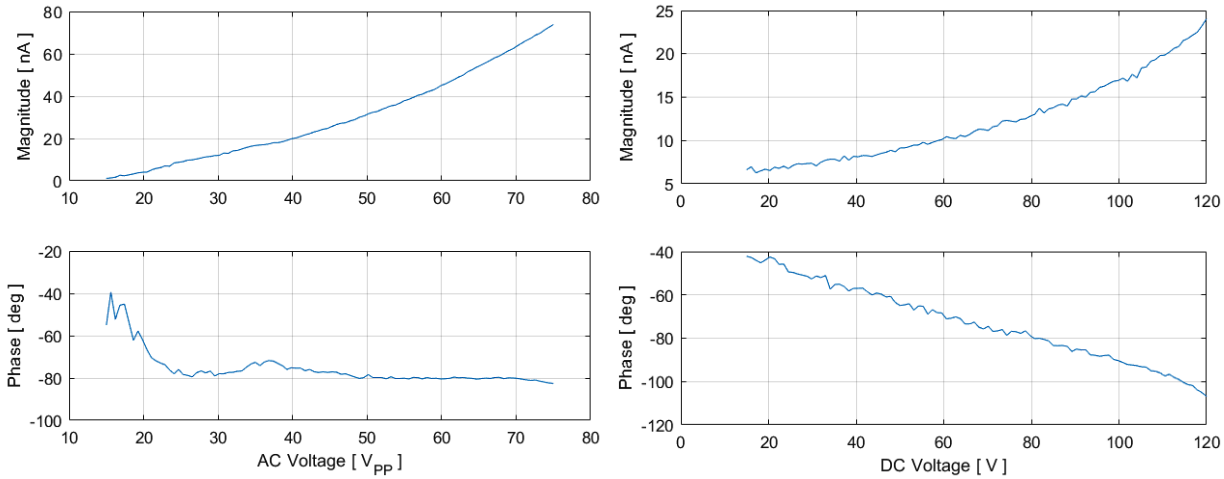

(a) Sweeping V_{AC} while $V_{DC} = 75V$ (b) Sweeping V_{DC} while $V_{AC} = 60V_{PP}$

Figure 5.5: Current versus changes in actuation voltage parameters for EAFM device 2 in free running mode. The devices for two experiments were not the same.

distance in tapping mode.

Low Tip-Sample Separation: Contact Mode

Figure 5.6b shows the magnitude and phase of second design's current versus changing V_{DC} in contact mode while V_{AC} was fixed at $60V_{PP}$. Like the free-running mode, the output curves have been derived by measuring the current's magnitude and phase at the resonant frequency, 10568Hz, although for contact mode, we do not have the resonant effects, and the magnitude and phase have almost constant values at all frequencies.

Figure 5.6 also shows a quadratic trend for magnitude and a piecewise linear trend for the phase in both operating modes. This fact certifies that both tapping and contact modes could be used for topography if the DC voltage applied to the EAFM probe could be controlled to maintain the phase at a fixed value while the EAFM tip is scanning the sample's surface.

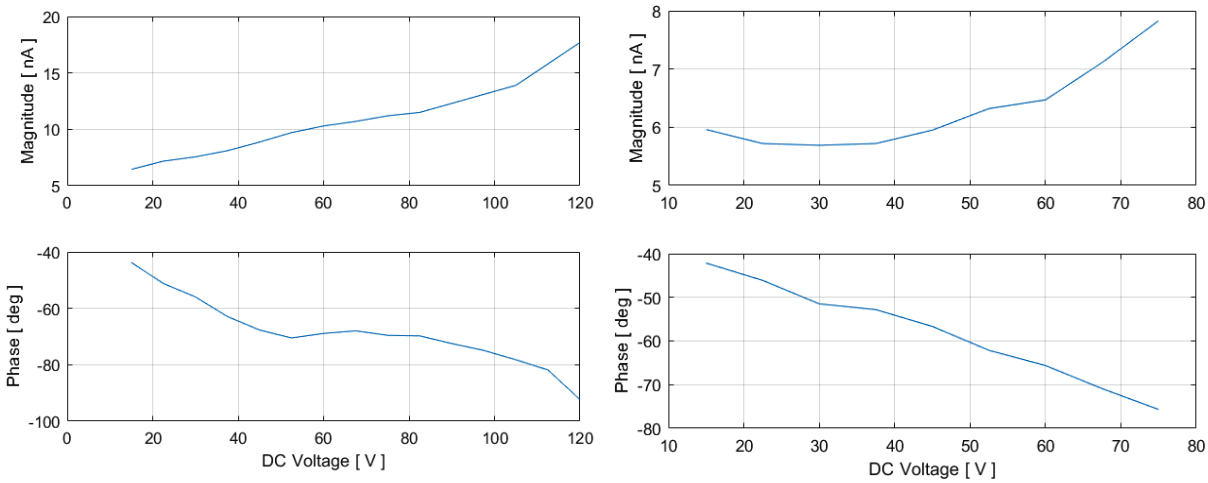

(a) Tapping mode

(b) Contact mode

Figure 5.6: Current versus V_{DC} for EAFM device 2 in two scanning modes, $V_{AC} = 60V_{PP}$.

5.3.2 Softening Effect

The well-known decrease in resonant frequency of the electrostatic actuators by increasing actuation voltage is also observable by the measurement of actuator's current in dynamic mode. Figure 5.7 shows the results of this test to investigate the impact of V_{DC} and V_{AC} on decreasing resonant frequency.

5.3.3 Hysteretic Jump

Hysteretic jump is one of nonlinear observations we had in driving the EAFM probe with relatively high voltages. The effect of this property is a sudden jump in the magnitude and phase of the actuator's current response if the excitation voltage increases from a certain level. This level depends on the initial gap between the cantilever and the counter

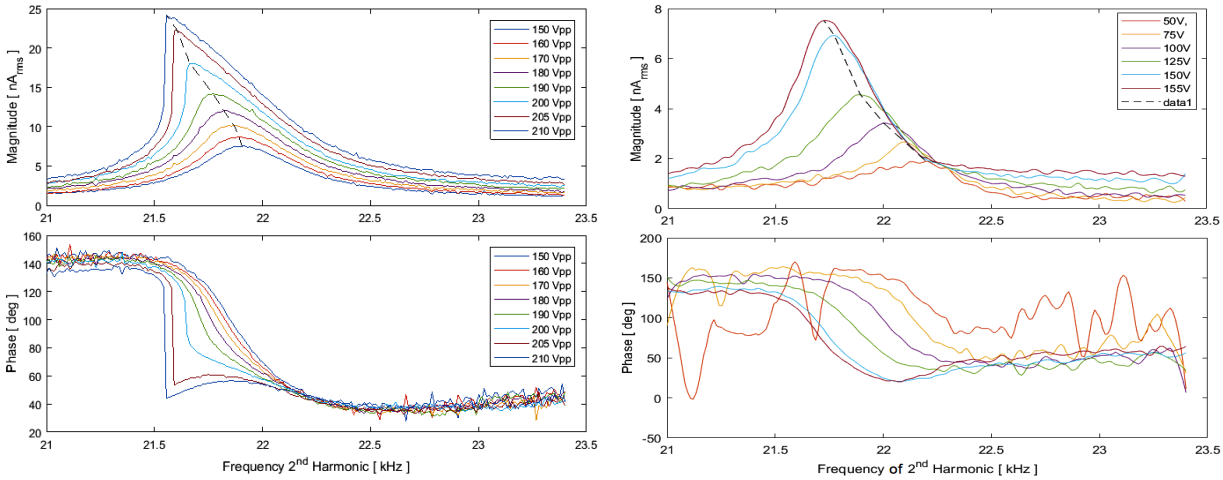

(a) Sweeping V_{AC} while $V_{DC} = 100V$

(b) Sweeping V_{DC} while $V_{AC} = 100V_{PP}$

Figure 5.7: Current versus changes in actuation voltage parameters for EAFM device 2 in contact mode.

electrode. As Figure 5.8 depicts, the frequency at which the magnitude or phase jump to another value decreases by increasing the actuation voltage because of the softening property in electrostatic actuators.

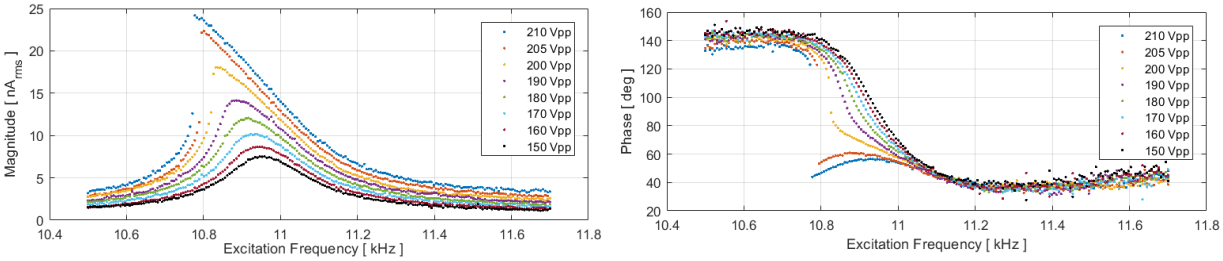

(a) Magnitude

(b) Phase

Figure 5.8: Current frequency responses showing the hysteretic jump and multivaluedness for different values of V_{AC} while $V_{DC} = 75V$.

5.3.4 Hysteresis Effect of Frequency Response

When an electrostatic actuator is working in tapping mode, the frequency responses of displacement to frequency sweeps in upward (increasing) and downward (decreasing) directions are not the same [20]. We observed the same phenomena for current measurements as illustrated by Figure 5.9.

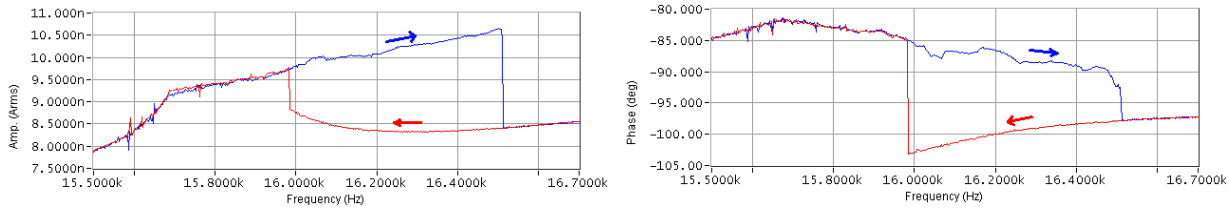

(a) Magnitude (b) Phase

Figure 5.9: The hysteretic effect of current magnitude and phase in upward and downward frequency sweeps.

The step in the frequency response is because of the bistable behavior of the vibrating cantilever. It depends on different factors including the cantilever's displacement amplitude, interacting surface forces, material stiffness and frequency.

5.4 Tapping

The purpose of the experiments in this part was finding the calibration curves of a tip-sample pair before the start of scanning. Calibration curves show the magnitude and phase of the electrostatic actuator's current versus tip-sample distance for a given actuation frequency. This frequency is usually the cantilever's resonant frequency ($f_\circ$) in free running mode (before tapping). Frequencies close to $f_\circ$ can also be selected.

The set of calibration curves can be exploited to determine the best tip-sample distance as well as best excitation frequency for tapping mode scanning in terms of linearity and sensitivity. The procedure was explained in section 3.2.1 with a set of results shown in Fig. 5.12.

In this experiment, current's magnitude and phase from all frequency responses at frequencies $(2f_\circ)$, $2(f_\circ - 20Hz)$ and $2(f_\circ + 20Hz)$ were selected as shown in Figure 5.13. $f_\circ$ is the resonant frequency of the AFM probe, measured by the frequency sweeps in the free running mode.

5.4.1 Calibration Curves

To derive the calibration curves depicted in Figure 5.11, one needs to select the current's magnitude and phase at a specific frequency while changing the tip-sample distance. Consequently, the frequency response curves for different tip-sample distances were recorded as illustrated in Figure 5.10. Figure 5.11 illustrates the cross section of the desired frequencies $(f_\circ - 20Hz,\ f_\circ$ and $f_\circ + 20Hz)$ with the frequency response curves which are known as calibration curves. In fact, for deriving these curves, all the frequency response vectors from the magnitude measurement were arranged in a matrix while the rows of this matrix were the individual frequencies and the columns were the vectors corresponding to different distances.

Then one row which represents all the magnitude values for different tip-sample distances was selected at a certain frequency, $f_\circ$. This procedure was iterated for two other frequencies, namely $f_\circ - 20Hz$ and $f_\circ + 20Hz$. The whole process was repeated for the

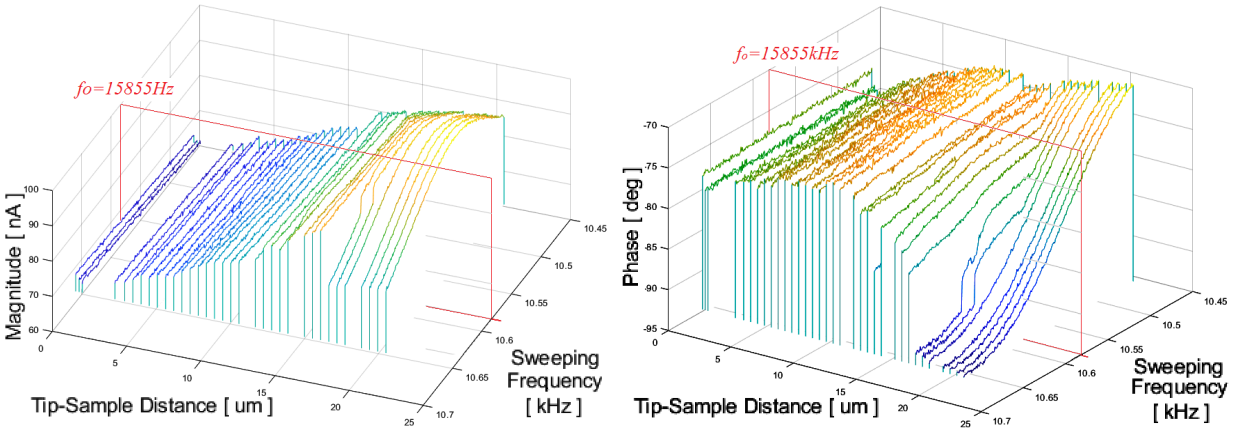

(a) Magnitude (b) Phase

Figure 5.10: Waterfall diagram of current frequency response curves versus different tip-sample distances.

phase in order to have six vectors including the magnitude and phase versus different tip-sample distances.

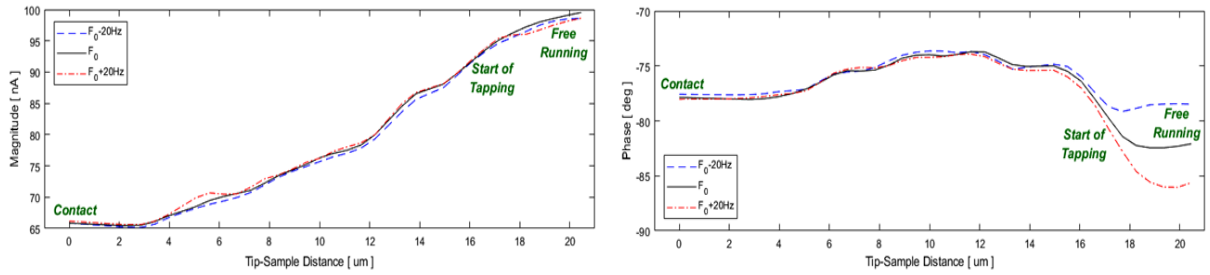

(a) Magnitude (b) Phase

Figure 5.11: Calibration curves versus tip-sample distance for three different frequencies.

At the next step, the area on the curves of Figure 5.11 with the steepest slope and simultaneously, highest linearity were recognized to provide the best differentiability. In this way, the difference of tip-sample distances were found by measuring the current's magnitude and phase. These information resemble the topography of the surface at the

point of scanning. The sections on the calibration curves satisfying the criteria were close to tip-sample distances in which slight tapping started. These area are assigned with 'Start of Tapping' in Figure 5.11.

Then the partial calibration curves were resketched in Figure 5.12 again to find the best excitation frequencies and optimum tip-sample distances while scanning the specimen.

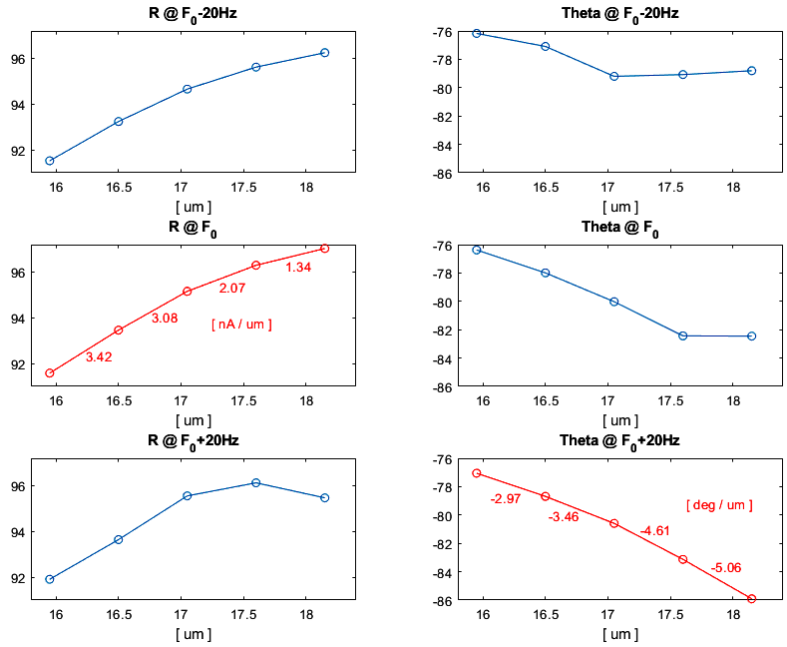

Figure 5.12: Partial calibration curves for distances close to the start of tapping at three frequencies.

In Figure 5.12, two curves which showed the highest linearity and differentiability are sketched with red color. In fact, the best response in regards to the magnitude, happened at $f_\circ$ and to the phase at $f_\circ + 20Hz$. Table 5.1 shows a summary of these results.

Figure 5.13 illustrates another representation for this approach. This figure shows the selected frequency response curves near to tapping with the raw and processed data.

Table 5.1: Summary of measurement results to find the optimum tip-sample distance and best excitation frequency.

Quantity	Sensitivity	Unit	Frequency
Magnitude	3.42	$nA/\mu m$	$f_\circ$
Phase	5.06	$deg/\mu m$	$f_\circ + 20Hz$

Indeed, the frequency response curves which contributed in the partial calibration curves were selected and shown only. The dashed curves represent the same data after applying a local regression method with a small window for data smoothing. Then the magnitude and phase values were derived for the selected distances as shown in Figure 5.12. The curves in Figure 5.12 are the same as insets in Figure 5.13.

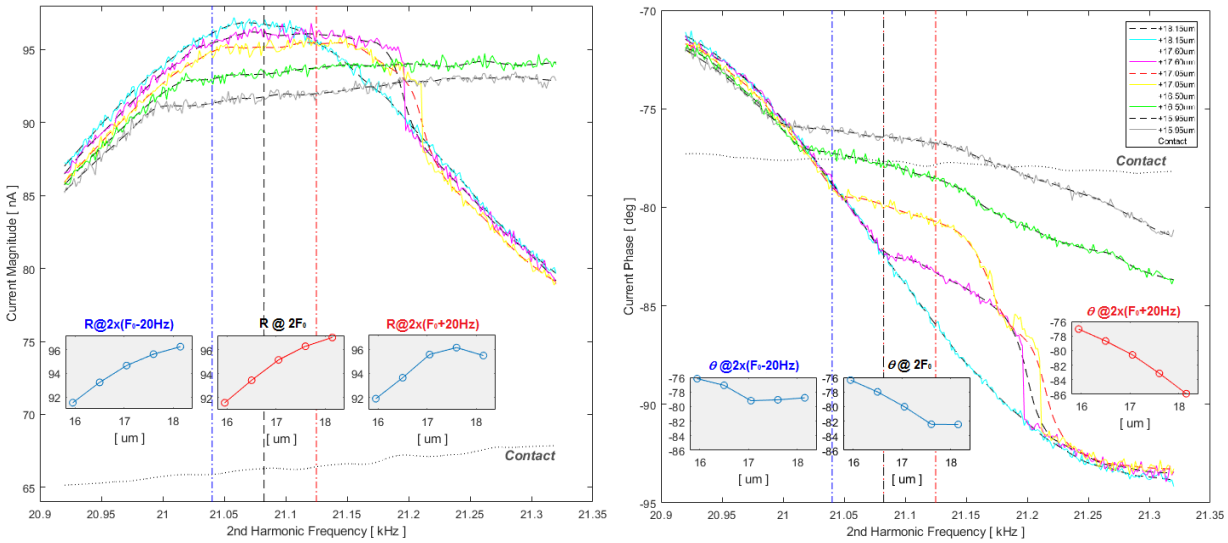

(a) Magnitude (b) Phase

Figure 5.13: Current frequency response curves vs tip-sample distance showing the responses for 'free running' and 'close to start of tapping'. The response for contact mode has been added for the purpose of comparison. The insets show the partial calibration curves produced by crossing the vertical lines and the frequency response curves.

To achieve the maximum phase difference, it is better to scan the sample at a frequency, higher than resonant frequency and for magnitude, scanning in resonant frequency produces the best result. Based on the information of insets with red curves in Fig. 5.13 , and the calculated RMS value of noise in each distance, this open-loop setup can provide a minimum detectable range for magnitude as $68.71nm$ scanned at $2f_\circ$ and for phase as $50.5nm$ scanned at $2(f_\circ + 20Hz)$.

5.5 Line Scanning

One line of a random specimen was rescanned in order to investigate the feasibility of the constructed system and the measurement approach. Using the 1-D piezoscanner, several line scannings were implemented. Scans were started from lines of $15\mu m$ length and fixed speed of $9.43\mu/sec$. In next steps, the same line was scanned with the same speed and longer lengths up to $150\mu m$.

5.5.1 Scanning Procedure

The sample was brought to the vicinity of the AFM probe by the vertical stage while the sweeper feature of Zürich Instruments HF2LI lock-in amplifier was measuring the current's frequency response to certify the optimum tip-sample distance. Once the probe came to tapping, line scanning started.

The spectroscopy feature of HF2LI was used for acquiring the data. The timing of this feature was set to provide the trace of 5 lines scanning in one screenshot which could be

captured by the host computer. The curves in the screenshots were digitized later to derive the values for current's magnitude and phase. The digitized data was then segmented into separate curves as illustrated in Fig. 5.14.

5.5.2 Scanning Results

General patterns of magnitude and phase show a repeating scheme which resemble the sample's topography and approves the functionality of this approach.

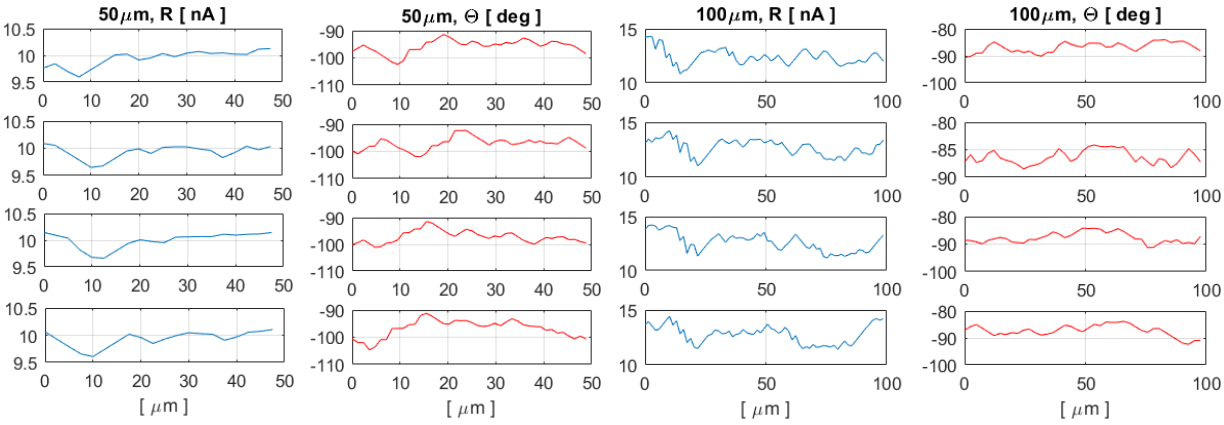

(a) Length $50\mu m$ (b) Length $100\mu m$

Figure 5.14: Electrostatic transducer's current while scanning lines with different lengths. Scanning speed=$9.43\mu m/s$ speed, Excitation signal: $V_{in}(t) = 75 + 75\sin(\Omega_0 t)$, measurement at $2\Omega_0$.

Comparing the magnitude curves in Figure 5.14a to magnitude curves in Figure 5.14b from 0 to $50\mu m$ discloses the similarity which also certifies the validity of measurements.

5.6 Raster Scanning

Raster scanning was implemented in open-loop and closed-loop fashions. Two fixtures were used for open-loop scanning, namely fixture 3 (section 3.2.3) and fixture 4 (section 3.2.4). Closed-loop scanning was performed by fixture 4 only.

To investigate any raster scanning, it is better to use known samples then compare the outcome of scanning process to the reality of the specimen. Several standard specimen are available on the market including calibration grating samples like TGZ2 and TGZ3 samples from NT-MDT Spectrum Instruments [26].

TGZ2 and TGZ3 have a periodic pattern with $3\mu m$ pitch. Their vertical features are $110nm$ and $500nm$ respectively as depicted in Figure 5.15.

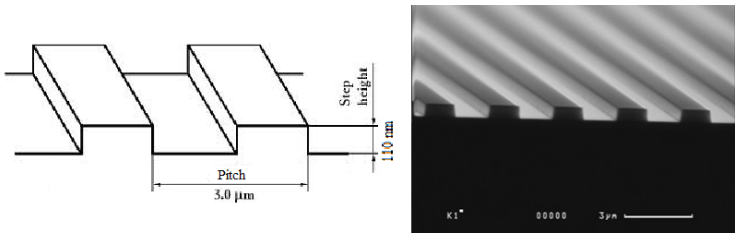

Figure 5.15: The outline and SEM picture of TGZ2 calibration grating sample.

The data produced by the HF2LI lock-in amplifier in this set of experiments were captured using LabOne, the new user interface deployed by Zürich Instruments. The plotter feature of HF2LI which is the time-domain data streaming tool was exploited for acquiring the current's magnitude and phase.

5.6.1 Open-loop Scanning

Scanning Procedure

Each line of the sample has been scanned 5 times. Each scan took $60sec$ with 13491 samples to produce enough source of information for post processing. The line scanner for this step was the nPoint piezoscanner with the scanning characteristics shown in Figure 5.16. This Figure shows the property of moving-dwelling which is crucial for all AFM XY scanner stages.

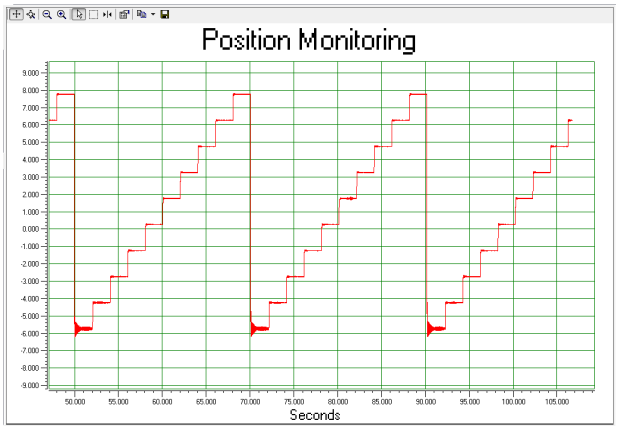

Figure 5.16: A sample of moving-dwelling method in piezoelectric scanners.

This property lets the scanner to settle after the transients caused by moving are diminished. The transients create a destroying impact on the quality of the final data. For better results, the data acquisition system should be synchronized to the line scanner in order to capture the data only when the scanner has been settled and is in the dwelling state.

For capturing the next line, the EAFM probe was progressed toward the next line manually with an accuracy less than $5\mu m$ and the aforementioned line scanning procedure

was repeated. Evidently, this distance was far below the requirements of AFM images, but at this step, the goal was only to show how this implementation can prove the concept of integrated electrostatic actuation/detection.

Scanning Results

The result of raster scanning of TGZ2 sample is shown in Fig 5.17. This scan covered a width of $X = 15\mu m$, but only a length of $10\mu m$ was used for imaging. In the Y direction, we had 14 lines with 5 scans in each line or 70 vectors covering a length of almost $70\mu m$. The sample had parallel features but it was placed with 45° angle in the stage.

X and Y matrices have been calculated in post-processing and for this specific case, they show more salient features. All four images in Fig. 5.17 show a rough resemble of the sample and prove the functionality of the device in an open-loop scheme. Apparently, a Y-direction scanner similar to the one exploited for X-direction scanning is an inevitable requirement for higher resolutions.

The sample illustrated in Figure 5.17 was scanned by 13491 samples acquired from 60 segments (pixels) in each row. The same area of the sample was scanned with 4497 samples acquired from 20 segments (pixels) in each row to compare the effect of number of samples visually. The result for magnitude, phase, X and Y are depicted in Figure 5.18. The images in Figure 5.17 show more details compared to Figure 5.18. The advantage of X and Y images is that they correlate two sets of information, namely magnitude and phase, and are able to show a better contrast from the sample's surface features.

As a result, a light post-processing was applied to the Y frame of Figure 5.17 to com-

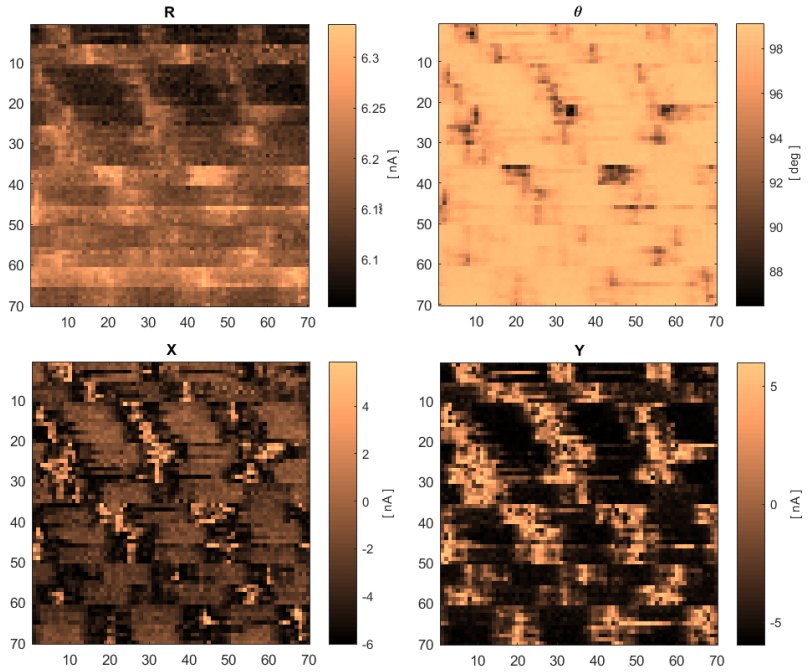

Figure 5.17: Results for open-loop raster scanning of AFM transducer's current using Fixture 3 before post-processing with 13491 samples-per-row. Images represent the magnitude, phase, X and Y of $10\mu m \times 70\mu m$ frame with scanning speed of $0.25\mu m/s$.

pensate the misalignment of adjacent rows. The result depicted in Figure 5.19 shows an image which can significantly resemble the TGZ2 calibration grating sample.

5.6.2 Closed-loop Scanning

Zürich Instrument™ HF2LI lock-in amplifier supports two PLLs modules and four Proportional Integral Derivative (PID) control modules. These options enable completing a closed-loop feedback scanning force microscopy with the block diagram shown in Figure 5.20a. For a better understanding of the test setup, the simplified block diagram of a

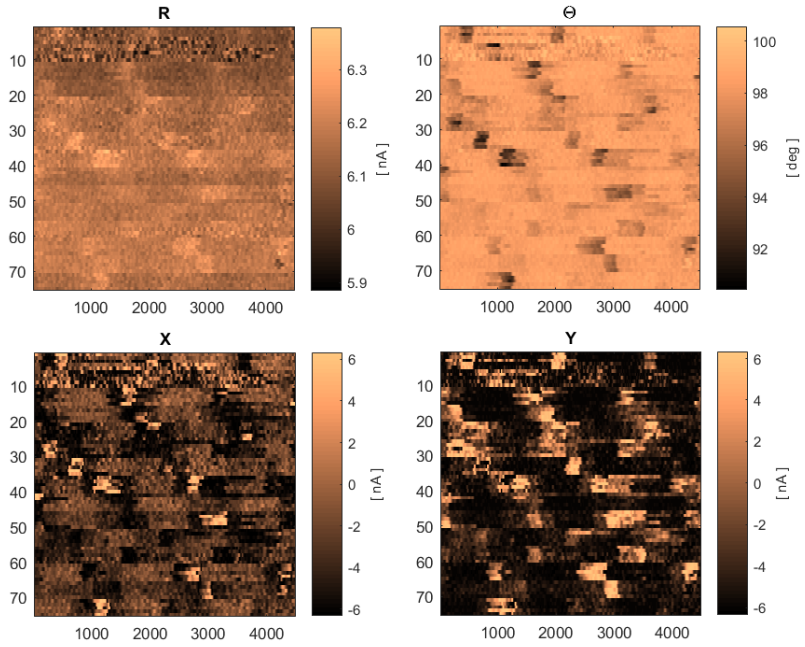

Figure 5.18: Results for open-loop raster scanning of AFM transducer's current using Fixture 3 before post-processing with 4497 samples-per-row. Images represent the magnitude, phase, X and Y of $10\mu m \times 70\mu m$ frame with scanning speed of $0.75\mu m/s$.

lock-in amplifier is depicted in Figure 5.20b.

To start a perfect scanning process, one needs to tune the PID controller gains. These gains are absolutely dependent to the lock-in amplifier's internal low-pass filter characteristics. To limit the maximum allowable variation of the output parameter, the PID controller needs to set the range of the output parameter. Consequently, the tuning problem has five variables to be determined together. The algorithm used in this research for setting these five parameters is as follows.

1. **Low-pass filter characteristic** This parameter determines the -3dB cut-off frequency (or time constant) of the lock-in amplifier filter. For the second harmonic of

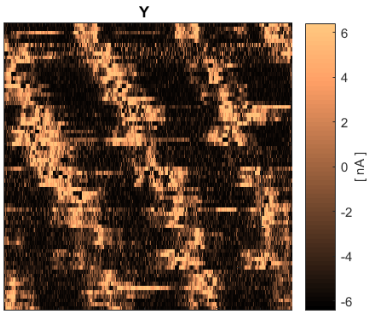

Figure 5.19: Y-image of Figure 5.17 after post-processing.

the excitation frequency it is better to select small cut-off frequencies to eliminate the high frequency noise.

2. **Range** This variable will be multiplied by the PID controller's gain (P) and added algebraically to the output signal. If it is selected large, it can help the potential instability in the feedback loop, and if it is too small, it can not compensate the output variable. As a result it has to be set carefully.

3. **PID Gains** By implementing known methods available, optimum values for the P, I and D gains could be found. One of these methods, recommended by the lock-in amplifier designer is the Ziegler-Nichols method.

Figure 5.21 shows two examples of applying the above method for the first and second harmonics. the PID gains and the Range values are determined with red boxes.

The block diagram in Figure 5.20 illustrates the closed-loop system. As the input parameter, one can select current's magnitude, phase, X or Y. Figure 5.21 shows R, but selecting X can involve both the current's magnitude and phase while it is insensitive to

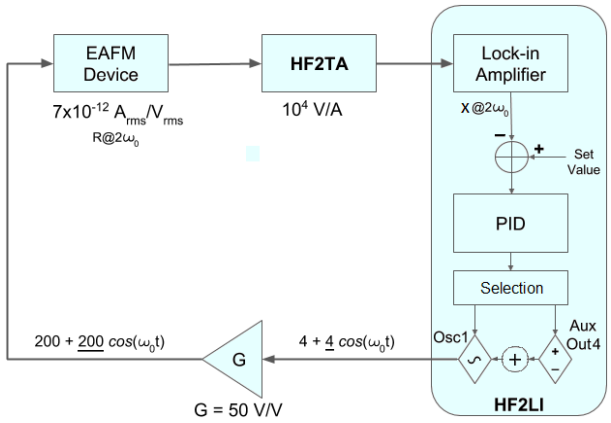

(a) Closed-loop feedback based on HF2LI's PID controller

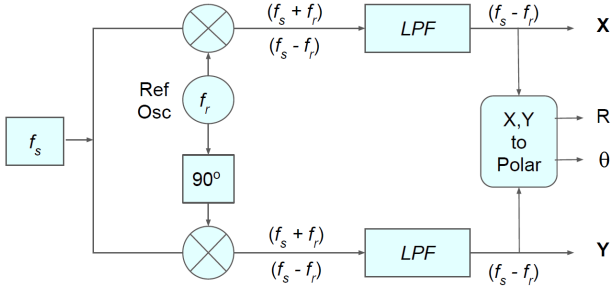

(b) Simplified Lock-in amplifier

Figure 5.20: Block diagrams of EAFM setup and lock-in amplifier. The selection box in (a) selects the control parameter: V_{AC} or V_{DC}.

unwanted phase unwrapping. The output parameter for this set of raster scanning was V_{AC}. This means one can use either the error signal or the output signal as the imaging parameter.

After tuning the PID parameters, several frames on the calibration grating sample TGZ3 were scanned using fixture 4 with results shown in Figure 5.22.

The same frame was scanned in the reverse direction with the feedback loop's output signal mapped in Figure 5.23.

The outcomes of closed-loop scanning illustrate the strong presence of transients because of the linear motion of motorized XY-stage. Indeed, for a perfect data acquisition, any scanning probe microscope needs to move the probe to a point, dwell at that point sufficiently long to allow the vibration of the probe settles, then collect the data, then let the probe move to the next pixel.

When the probe is moved by the scanner linearly, it looses the chance of settling to measure the exact surface force interactions at the desired point.

5.7 Summary

This chapter demonstrated the experiments designed and performed in this research with the results acquired by measuring the current of AFM probe at the second harmonic of actuation frequency. The vast majority of experiments proposed in this chapter were employing the latest AFM device named as Prototype 2.

The experiments were organized in four main sections.

1. One point tapping to investigate the behavior of the AFM probe and tip while actuated by a biased actuation voltage. The sample was vertically aligned to be in close proximity to the AFM probe's tip in most trials of these experiments. One of the main goals of this part was deriving the calibration curve necessary for adjusting the tip-sample distance.

   The nonlinear effects of electrostatic actuators in high actuation voltages were examined and recorded by measuring the actuator's current to compare with the mathematical and numerical analyses.

2. Line scanning for testing the validity of current measurement for deriving the topography of a random sample. The measurements show an acceptable output certifying the fundamental objective of the project.

3. Open-loop raster scanning of a known standard grating sample produced preliminary images which resembled the pattern of the sample according to the overall conditions of the equipment.

4. Closed-loop raster scanning of a known standard grating sample.

(a) Main harmonic

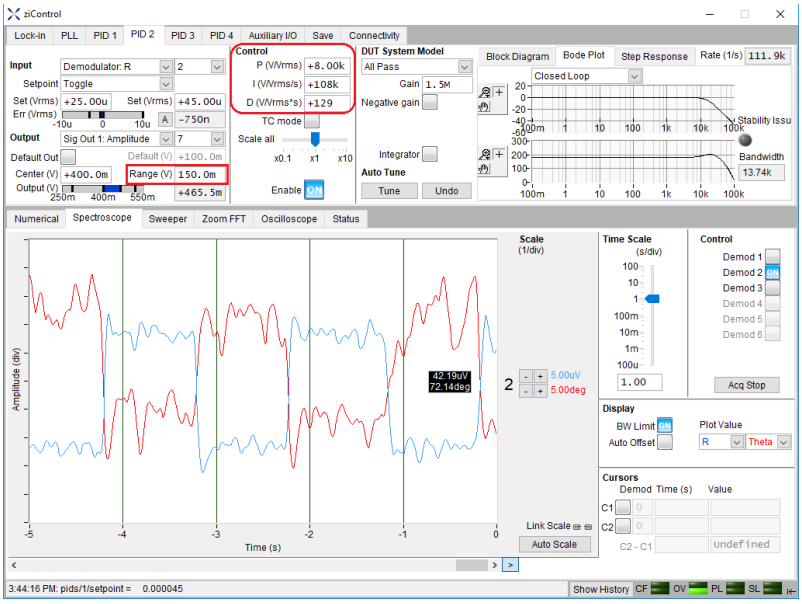

(b) Second harmonic

Figure 5.21: PID controller step responses after tuning the PID gains.

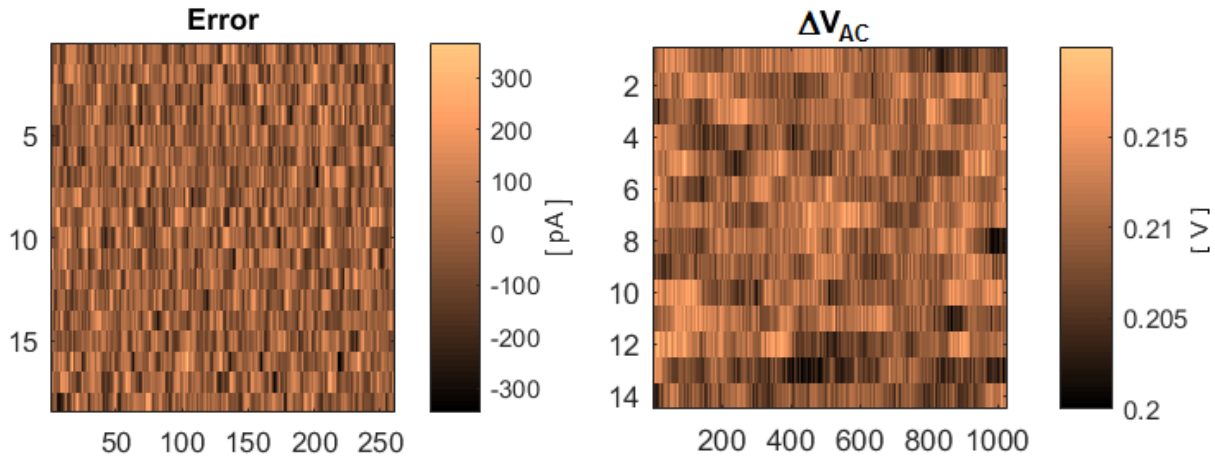

(a) Error signal (b) ΔV_{AC}

Figure 5.22: Spatial map of feedback loop's input and output signals for a raster of $20 \times 18 \mu m$. $V_{DC} = 33V, V_{AC,initial} = 63V_{pp}, f_\circ = 9985Hz$.

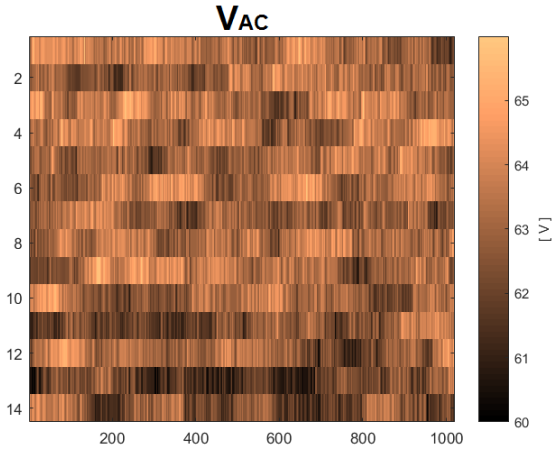

Figure 5.23: Spatial map of V_{AC} for the same raster as Figure 5.22 scanned in the reverse direction. $V_{DC} = 33V, V_{AC,initial} = 63V_{pp}, f_\circ = 9985Hz$.

Chapter 6

Conclusions and Future Work

6.1 Conclusions

In this thesis, a profound review on different methods applied for integration and miniaturization of AFM devices and systems was proposed to conclude that electrostatic actuation and detection could provide a promising tool to achieve the objective of the project.

In next step, appropriate devices and circuits based on available technologies and off-shelf AFM probes were designed which resulted in two feasible design concepts. The analytical models for each design concept were developed in order to evaluate the performance of the AFM probe prototypes and designed structures. Numerical analysis methods in static and dynamic modes were exploited to show the structural mechanics of the sensing device as well as to simulate the behavior of the designed AFM device under different actuation conditions. The results of this analysis were in compliance to the experimental

results.

To find the optimum design and measurement strategy, determining a conceptual model of the measurement system was inevitable. This model proposed the relation of the desired information to the measurable quantity in the integrated electrostatic actuator / capacitive detector. As a matter of fact, the model defined the displacement of the AFM probe as the source of information governed by the actuator's excitation voltage and interatomic forces at each point of the sample. These forces managed the amplitude of probe's tip, thus, the motion induced current. A lock-in amplifier was used to measure this current at the second harmonic of excitation frequency for a biased actuation voltage and the third harmonic of excitation frequency for an unbiased actuation voltage. The mathematical model of the actuators's current versus the tip displacement was developed.

To examine the feasibility of the conceptual model, two types of integrated actuator/detector devices were designed, implemented and tested leading to selection of the appropriate operating mode, or tapping mode. Therefore, necessary test setups were designed and constructed to facilitate this operating mode in the next steps.

Finally, several components for the EAFM device and mechanical fixtures were developed to accommodate all components of the system.

To prepare the required hardware, a step by step procedure was considered to reach the final target of the project, namely, scanning a raster on calibration grating samples. This procedure included firstly the point scanning to test the effect of tapping on the motion induced current and to find the optimum tip-sample distance. Secondly, scanning a line on a random sample to check the validity of the employed system and finally scanning a

raster on a calibration grating sample.

The surface of calibration grating samples were scanned while the transducer's current was recorded. Two sets of experiments, namely, open-loop scanning and closed-loop scanning were implemented. The AFM images acquired in open-loop scanning resembled the topography of the sample while the signals mapped spatially in closed-loop scanning were overwhelmed by transients.

6.2 Future Work

There are a number of points which need further efforts to be addressed:

1. According to the dynamic analysis and experimental results in this research and based on the dynamic analysis of an AFM probe in tapping mode presented in [6], it is evident that a second mode (or even higher modes) of excitation emerges when the AFM's cantilever starts to touch the sample's surface. In fact, the cantilever will leave the state of smooth oscillation and enter the new state of impact oscillation with different kinds of nonlinearities like grazing bifurcation and period doubling which tend to chaos. These nonlinear behaviors need to be investigated through considering higher modes of excitation, otherwise, limitations will be imposed to the accuracy of the AFM's probe analysis. This analysis could be of a high interest because of the inherent nonlinearity of electrostatic actuation which was not the subject of research in [6].

2. The difference of the outputs in this research and what has been proposed in [6] is

another topic which can be investigated in a future work combined to the first topic. The output of reviewed researches in the literature [6, 20, 4] is the displacement (or velocity) with absolute and average values measurable at any frequency harmonic including the excitation frequency. On the other hand, the output in this research is the Root Mean Square value of current's magnitude and current's phase measurable only at the second harmonic of the excitation frequency.

3. Applying other modes of scanning like non-contact mode with changes in cantilever's resonant frequency or FM-AFM is an attractive area of research.

4. Improving the quality of images produced. Following cases could be considered for this purpose:

   (a) Any XY-stage employed for scanning should facilitate step-wise motions in both directions.

   (b) The number of scanned rows could be increased to raise the image resolution.

   (c) The data acquired by the AFM transducer need to go through further processing techniques according to conventional AFM image post-processing methods like leveling or filtering [19] to eliminate the artifacts caused by sample tilting or noise.

   (d) The PID controller gains could be revised before starting each scan to achieve more accurate feedback parameters.

5. Investigating the ability of this approach in simplifying other methods of force microscopy for instance, electric force microscopy, magnetic force microscopy and Kelvin

probe force microscopy.

6. Investigating the capability of this system in manipulating the surface of objects. Specifically, producing micro and nano-channels for lab-on-a-chip projects.

7. Investigating the capability of this system in inspecting the surface of objects in micro scale.

8. Extending the mathematical model to include other surface forces.

9. Investigating the effect of damping and temperature change on the output performance of the detection mechanism.

10. Improving the mechanical structure of the EAFM device and the mechanical fixture to shrink the size and price of the whole system.

References

[1] E M Abdel-Rahman and A H Naifeh. Secondary resonances of electrically actuated resonant microsensors. *J. Micromech. Microeng.*, 13:491–501, 2003.

[2] T Akiyama, U Staufer, N F de Rooij, D Lange, C Hagleitner, O Brand, H Baltes, A Tonin, and Hidber H R. Integrated atomic force microscopy array probe with metal-oxide-semiconductor field effect transistor stress sensor, thermal bimorph actuator, and on-chip complementary metal-oxide-semiconductor electronics. *Journal of Vacuum Science & Technology*, B(18(6)), Nov/Dec 2000.

[3] T Akiyama, U Staufer, and de Rooij N F. Atomic force microscopy using an integrated comb-shape electrostatic actuator for high-speed feedback motion. *APPLIED PHYSICS LETTERS*, 76(21 22), 2000.

[4] M. Ashhab, M.V. Salapaka, M. Dahleh, and I. Mezić. Dynamical analysis and control of microcantilevers. *Automatica*, 35(10):1663 – 1670, 1999.

[5] M Azizi and N Sarkar. Single-chip CMOS-MEMS dual mode scanning microwave microscope. *IEEE TRANSACTIONS ON MICROWAVE THEORY AND TECH-*

NIQUES, 61(12), 2013.

[6] A Bahrami and A H Nayfe. On the dynamics of tapping mode atomic force microscope probes. *Nonlinear Dyn*, 70:1605–1617, 23 August 2012.

[7] J Bay, S Bouwstra, E Laegsgaard, and O Hansen. Micromachined AFM transducer with differential capacitive read-out. *Journal of Micromechanics and Microengineering*, 5(2):161, 1995.

[8] Felix Beyeler, Adrian Neild, Stefano Oberti, Dominik J Bell, Yu Sun, Jrg Dual, and Bradley J Nelson. Monolithically fabricated microgripper with integrated force sensor for manipulating microobjects and biological cells aligned in an ultrasonic field. *Journal of microelectromechanical systems*, 16(1):7–15, 2007.

[9] B Bhushan, H Fuchs, and S Kawata. Springer Verlag, Berlin Heidelberg.

[10] G Binnig, C F Quate, and C Gerber. Atomic force microscope. *Physics Review Letters*, 56:930–933, 1986.

[11] N Blanc, J Brugger, and N F de Rooij. Scanning force microscopy in the dynamic mode using microfabricated capacitive sensors. *Journal of Vacuum Science & Technology*, B(14(2)), Mar/Apr 1996.

[12] J Brugger, N Blamf, Ph Renaudb, and N F de Rooija. Microlever with combined integrated sensor/actuator functions for scanning force microscopy. *Sensors and Actuators*, 43:339–345, 1994.

[13] J Brugger, R A Buser, and N F de Rooij. Micromachined atomic force microprobe with integrated capacitive read-out. *Journal of Micromechanics and Microengineering*, 2(3):218, 1992.

[14] R S Carter and J J Rush. *Molecular Dynamics and Structure of Solids*. NATIONAL BUREAU OF STANDARDS, national bureau of standards special publication 301 edition.

[15] Bruker Corporation. AFM probes. *Bruker's Products Catalog*, 2013.

[16] A Dec and K K. Suyamat. Micromachined electro-mechanically tunable capacitors and their applications to rf ic's. *IEEE Transactions on Microwave Theory and Techniques*, 46(12):2587 – 2596.

[17] D Dickel, M J Skove, and A M Rao. An analytic characterization of the harmonic detection of resonance method. *Journal of Applied Physics*, 106, 2009.

[18] E C M Disseldorp, F C Tabak, A J Katan, M B S Hesselberth, T M Oosterkamp, J W M Frenken, and W M van Spengen. MEMS-based high speed scanning probe microscopy. *Review of Scientific Instruments*, 81(2):375 – 382, 2010.

[19] P EATON and P West. *Atomic Force Microscopy*. Oxford University Press Inc., New York, 1 edition, 2010.

[20] R García and A San Paulo. Attractive and repulsive tip-sample interaction regimes in tapping-mode atomic force microscopy. *PHYSICAL REVIEW B*, 60(7):4961–4967, 1999.

[21] J Geerlings, E Sarajlic1, J W Berenschot, M H Siekman, H V Jansen, L Abelmann, and N R Tas. Design and fabrication of in-plane AFM probes with sharp silicon nitride tips based on refilling of anisotropically etched silicon moulds. *J. Micromech. Microeng.*, 24, 2014.

[22] E S Hung and S D Senturia. Extending the travel range of analog-tuned electrostatic actuators. *Journal of Microelectromechanical Systems*, 8(4):497–505, 1999.

[23] S J Hung, S W Wang, and M S C Lu. Cmos micromachined capacitive cantilevers for efmbased mass data storage. In *Proceedings of the 3rd IEEE Int. Conf. on Nano/Micro Engineered and Molecular Systems, Sanya, China*. IEEE, Jan 6-9, 2008.

[24] P F Indermuhle, C Linder, J Brugger, V P Jaecklin, and N F de Rooij. Design and fabrication of an overhanging xy-microactuator with integrated tip for scanning surface profiling. *Sensors and Actuators A*, A(43):346–350, 1994.

[25] P-F Indermühle, G Schürmann, G-A Racine, and N F de Rooij. Atomic force microscopy using cantilevers with integrated tips and piezoelectric layers for actuation and detection. *Journal of Micromechanics and Microengineering*, 7(3):218, 1997.

[26] NT-MDT Spectrum Instruments. TGZ2 calibration grating sample. *TGZ Series Datasheet*, 2018.

[27] J N Israelachvili. *Intermolecular and surface forces*. Elsevier, Academic Press, 3 edition.

[28] J E Jones. On the determination of molecular fields. ii. from the equation of state of a gas. 1924.

[29] P N Kambali and A K Pandey. Gimbal-less two-axis scanning MEMS micromirrors: Device datasheets. *Mirrorcle Technologies Inc.*, 16(2):375–382, 2016.

[30] T C Lim. Scaling function between the exponential-6 and the generalized lennard-jones potential functions. *Journal of Mathematical Chemistry*, 33(3-4), 2003.

[31] C J Long and R J Cannara. Modular apparatus for electrostatic actuation of common atomic force microscope cantilevers. *Review of Scientific Instruments*, 86, 2015.

[32] T Michels and I W Rangelow. *Review of scanning probe micromachining and its applications within nanoscience*, 126:191–203, 2005.

[33] V Milanovic, G A Matus, and D T McCormick. Gimbal-less monolithic silicon actuators for tip–tilt–piston micromirror applications. *IEEE JOURNAL OF SELECTED TOPICS IN QUANTUM ELECTRONICS*, 10(3):462–471, 2004.

[34] S A Miller, K L Turner, and N C MacDonal. Microelectromechanical scanning probe instruments for array architectures. *Rev. Sci. Instrum*, 68(11), 1997.

[35] F Müller, A D Müller, M Hietschold, and T Gesxner. Atomic force microscopy in dynamic mode with displacement current detection in double cantilever devices. *Japanese Journal of Applied Physics*, 45(3B):1974–1977, 2006.

[36] A H NAYFEH1, M I YOUNIS, and E M ABDEL-RAHMAN. *Reduced-Order Models for MEMS Applications*, 41:211–236, 2005.

[37] M Olfatnia, L Cui, P Chopra, and S Awtar. Based xy stage with large displacement. *IDETC/CIE*, 16, 2013.

[38] H M Ouakad. Comprehensive numerical modeling of the nonlinear structural behavior of MEMS/NEMS electrostatic actuators under the effect of the van der waals forces. *Microsyst Technol*, 2017.

[39] S P Pacheco, L P B Katehi, and C T C Nguyen. Design of low actuation voltage rf MEMS switch. In *Microwave Symposium Digest. 2000 IEEE MTT-S International*, pages 912–915. IEEE, 11-16 June 2000.

[40] S H Pakdast. Advanced MEMS resonator for mass detection and micromechanical transistor.

[41] S Park and E M Abdel-Rahman. Low voltage electrostatic actuation and displacement measurement through resonant drive circuit. In *International Design Engineering Technical Conference, Chicago, Illinois, USA, 2012*. DETC, 2012.

[42] S Park, Y Bai, and J T W Yeow. Design and analysis of resonant drive circuit for electrostatic actuators. In *Optomechatronic Technologies (ISOT), 2010 International Symposium on*. IEEE, Jan 2010.

[43] S Park, M Khater, D Effa, E M Abdel-Rahman, and Yavuz M. Detection of cyclic-fold bifurcation in electrostatic MEMS transducers by motion-induced current. *Journal of Micromechanics and Microengineering*, 27:119–126, 2017.

[44] R R. Vermeer, E Sarajlic, M Siekman1, H Kawakatsu, H Fujita3, N R Tas, and H V Jansen. Electrostatically actuated double cantilever AFM probe for high speed imaging. In *Transducers 2013, Barcelona, SPAIN*, pages 912–915. IEEE, June 2013.

[45] R J Roark and W C Young. *Formulas for Stress and Strain*. Mc Graw Hill, Singapore, 5 edition, 1976.

[46] M G Ruppert, M Fowler, A G Maroufi, and S O R Moheimani. On-chip dynamic mode atomic force microscopy: A silicon-on-insulator MEMS approach. *JOURNAL OF MICROELECTROMECHANICAL SYSTEMS*, 26(1):215–225, 2017.

[47] M G Ruppert and S O R Moheimani. A novel self-sensing technique for tapping-mode atomic force microscopy. *Review of scientific instruments*, 84, 2013.

[48] D Sarid. *Scanning Force Microscopy*. Oxford University Press, 5 edition, 1991.

[49] N Sarkar, G Lee, and R Mansour. CMOS-MEMS dynamic fm atomic force microscope. *IEEE Sensors Journal*, 2013.

[50] N Sarkar et. al. CMOS-MEMS atomic force microscope. *IEEE Sensors Journal*, 16(2):375–382, 2011.

[51] Stephen D Senturia. *Microsystem design*. Springer US, 2013.

[52] F C Tabak, E C M Disseldorp, G H Wortel, A J Katan, M B S Hesselberth, T M Oosterkamp, J W M Frenken, and W M van Spengen. MEMS-based fast scanning probe microscopes. *Ultramicroscopy*, 110:599 – 604, 2010.

[53] J Thaysen, A Boisen, O Hansen, and S Bouwstra. Atomic force microscopy probe with piezoresistive read-out and a highly symmetrical wheatstone bridge arrangement. *Sensors and Actuators*, 83:47–53, 2000.

[54] S Towfighian. A large-stroke electrostatic micro-actuator.

[55] A Ulcinas and V Snitka. Intermittent contact AFM using the higher modes of weak cantilever. *Ultramicroscopy 86 (2001) 217±222*, 86:217–222, 2001.

[56] K Umeda, K Kobayashi, K Matsushige, and H Yamada. Direct actuation of cantilever in aqueous solutions by electrostatic force using high frequency electric fields. *Applied Physics Letter*, 101:123112–1,4, Sep 2012.

[57] RC Voicu, C Tibeica, R Müller, A Dinescu, M Pustan, and C Birleanu. Design, simulation and testing of polymeric microgrippers with v-shaped electrothermal actuators and encapsulated heaters. In *International Semiconductor Conference (CAS), 2016*, pages 89–92. IEEE, 2016.

[58] M I Younis. *MEMS Linear and Nonlinear Statics and Dynamics*. Springer, 2011.

[59] M I Younis and E M Abdel-Rahman. A reduced-order model for electrically actuated microbeam-based MEMS. *Journal of microelectromechanical systems*, 12(5), Oct 2003.